

AN ABSTRACT OF THE THESIS OF

Jackson R. Harter for the degree of Master of Science in Nuclear Engineering presented on October 1, 2015.

Title: Predicting Thermal Conductivity in Nuclear Fuels using Rattlesnake-Based Deterministic Phonon Transport Simulations.

Abstract approved: _____

Todd S. Palmer

The Boltzmann transport equation derived in the Self-Adjoint Angular Flux (SAAF) formulation is applied to simulate phonon transport. The neutron transport code Rattlesnake is leveraged in this fashion, slightly modified to accept input from variables consistent with phonon transport simulations. Several benchmark problems are modeled to assess the potential of this application to predict thermal conductivity in materials with heterogeneity and isotopic fission products affecting thermal transport. The 1-D, SAAF formulation of the Boltzmann transport equation for phonons is derived along with associated boundary conditions. Comparisons to phonon transport problems solved via deterministic, Monte Carlo (MC) and molecular dynamics (MD) methods are shown. Phonon intensity and heat flux are used to compute thermal conductivity in materials.

Phonon transport with Rattlesnake using similar input conditions compares well to test problems in open literature. Transport is simulated in one and two element systems, with special emphasis on uranium dioxide (UO_2) with xenon cluster defects. Rattlesnake solutions show thermal conductivity in UO_2 decreasing by up to a factor of 4 at elevated temperatures. Transport behavior for these problems appears qualitatively correct, though lack of data for xenon properties yields results which deviate from MD simulations. Results are generally favorable, though

the current deterministic phonon transport implementation does not include certain phonon scattering physics. Further development of Rattlesnake is discussed, with an emphasis on coupling with phase fields for better characterization of microstructure in nuclear fuel.

©Copyright by Jackson R. Harter

October 1, 2015

All Rights Reserved

Predicting Thermal Conductivity in Nuclear Fuels using Rattlesnake-Based
Deterministic Phonon Transport Simulations

by

Jackson R. Harter

A THESIS

submitted to

Oregon State University

in partial fulfillment of
the requirements for the
degree of

Master of Science

Presented October 1, 2015
Commencement June 2016

Master of Science thesis of Jackson R. Harter presented on October 1, 2015.

APPROVED:

Major Professor, representing Nuclear Engineering

Head of the School of Nuclear Science and Engineering

Dean of Graduate School

I understand that my thesis will become part of the permanent collection of Oregon State University libraries. My signature below authorizes release of my thesis to any reader upon request.

Jackson R. Harter, Author

ACKNOWLEDGEMENTS

I thank Dr. Todd Palmer for being a wonderful mentor, professor and friend. When I began my journey into the field of Nuclear Engineering, he was the first person I met when I walked into the Radiation Center more than six years ago. He helped me find who I was looking for and I was completely struck by his kindness and willingness to help. I have continually found this to be true during my tenure as his student and look forward to our future collaborations together. He has given me his unconditional support throughout this process, and I am eternally grateful.

My minor professor, Alex Greaney, is a fantastic mentor and friend and has been a driving force during my materials science education. He is always eager to lend help, listen, or talk through difficulties with me.

I have been lucky to meet other fantastic people along my way who have influenced me greatly. I thank William Comolli, Don Buenaventura and Jeff Kapernick. These gentlemen formed the core of my undergraduate study groups and have evolved into being true friends to me. I appreciate their viewpoints, criticisms, and senses of humor. I don't know that I could have had such success in this new field without their presence.

My experience in graduate school has changed me forever, it is surprising that such changes can take place in two short years. There are times of difficulty, and I thank the continual support of my friends and fellow graduate students to help see me through. In particular, Darin Reid, Mario Gomez, Tony Alberti, Tommy Holschuh, Doug Woods, Kyle Hoover, Kyle Combs, Adam Zabriskie and Laura de Sousa Oliveira are people whom I can bounce ideas off of, discuss problems and commiserate with.

I have had the good fortune to meet and collaborate with the talented researchers at Idaho National Laboratory. I was able to spend this past summer as an intern at the lab, working with Daniel Schwen. His ideas and guidance have been greatly appreciated and beneficial. I also thank Mark DeHart for the opportunity to work in the MOOSE family, and Yaqi Wang for his thoughtful input and helpful discussions.

My family has truly been at the center of all of this. When I departed my previous life of cooking professionally, I had no idea what was in store for me. I moved into my family's home in Corvallis with my mother Christine, step-father Toby and sister Kelsey. I could not have done all of this without their love, support and compassion. I also thank my brother Harrison and father Rod. They do not live in Corvallis but have been there for me along the way, and I thank them for their kindness and support. I love you all.

This research was supported under a Department of Energy grant in conjunction with the Idaho National Laboratory and National University Consortium.

TABLE OF CONTENTS

	<u>Page</u>
1 INTRODUCTION	1
1.1 Literature Review	4
1.1.1 Monte Carlo Approaches in Phonon Transport	4
1.1.2 Molecular Dynamics Methodology	6
1.1.3 Deterministic Solution Techniques	7
1.1.4 Introduction to MOOSE and Rattlesnake	9
1.1.5 Phonon Transport in UO ₂ with Impurities	10
1.1.6 Effects of Xenon on UO ₂ Thermal Conductivity	13
1.2 Thesis Overview	15
2 PHONON TRANSPORT PHYSICS	16
2.1 Introduction	16
2.2 The Boltzmann Transport Equation for Phonons	16
2.2.1 Gray Phonon Transport	18
2.2.2 The Self-Adjoint Angular Flux Formulation	20
2.2.3 Definition of Equilibrium Intensity	21
2.3 Phonon Interaction Processes	23
2.3.1 The Dispersion Relation	24
2.4 Relaxation Time Contributions	27
2.4.1 Size Effects	27
2.4.2 Normal and Umklapp Processes	28
2.4.3 Lattice Imperfections	34
2.5 Summary	37
3 METHODS	38
3.1 Introduction	38

TABLE OF CONTENTS (Continued)

	<u>Page</u>
3.2 Discretization of the Equations	38
3.2.1 Angular Discretization	38
3.2.2 Spatial Discretization - Slab Geometry	39
3.2.3 Boundary Conditions	41
3.2.4 Slab Geometry Code Development	42
3.3 Rattlesnake: A Radiation S_N Transport Code	43
3.4 Summary	48
 4 RESULTS	49
4.1 Introduction	49
4.2 Phonon Transport in Thin Films	49
4.3 Two Material System	53
4.4 Phonon Transport in z -axis Graphite	61
4.5 Thermal Conductivity in Single Crystal UO_2	63
4.6 UO_2 with Xenon Defects	71
4.7 Summary	81
 5 CONCLUSIONS	82
5.1 Introduction	82
5.2 Discussion of Results	82
5.2.1 Thin Film Transport	82
5.2.2 Two Material System	84
5.2.3 Transport in Graphite	88
5.2.4 Single Crystal UO_2	92

TABLE OF CONTENTS (Continued)

	<u>Page</u>
5.2.5 UO ₂ with Xenon Defects	93
5.3 Overall Conclusions and Future Work	95

LIST OF FIGURES

<u>Figure</u>		<u>Page</u>
1 Wigner-Seitz cell for a BCC lattice		26
2 Scattering change due to size effects in silicon		29
3 Trajectory of oxygen ion in UO_2		34
4 Stacking fault looking in $\langle 110 \rangle$ direction		36
5 Grain boundary showing velocity mismatch and dislocation array .		37
6 Spatial mesh and relevant quantities		39
7 Non-dimensional temperatures, Rattlesnake and Yilbas and Bin Mansoor		44
8 Non-dimensional heat flux		44
9 Mesh used in silicon thin film problem		51
10 Solution comparison with Yilbas and Bin Mansoor		51
11 Dependencies on quadrature set variation		52
12 Solution dependence on element count variation		53
13 Two-dimensional spatial domain		54
14 Temperature distribution at $t = 15 \text{ ps}$		55
15 Temperature distribution at $t = 85 \text{ ps}$		55
16 Mesh used in Al-Si system		57
17 Aluminum region of mesh		57
18 Phonon intensity, steady-state solution		58
19 Phonon intensity near aluminum dot, steady-state solution		58
20 Heat flux, x -direction		59
21 Heat flux, y -direction		59

LIST OF FIGURES (Continued)

<u>Figure</u>		<u>Page</u>
22 Rattlesnake solution at $t = 15$ ps		60
23 Rattlesnake solution at $t = 85$ ps		60
24 Mesh used in graphite scattering simulations		62
25 Thermal conductivity along z -axis		63
26 Experimental thermal conductivity for pristine UO_2 in $\langle 100 \rangle$, $\langle 110 \rangle$ and $\langle 111 \rangle$ directions		64
27 Laue back-reflection X-ray of UO_2 sample in $\langle 111 \rangle$ direction		65
28 Mesh used in UO_2 single crystal simulation		67
29 κ at 8 nm cell length		68
30 κ at 15 nm cell length		69
31 κ at 30 nm cell length		69
32 κ at 60 nm cell length		70
33 κ in superlattice		70
34 Comparison of thermal conductivities		71
35 Mesh used in UO_2 -Xe simulations		73
36 Non-dimensional temperature across z -axis at 300 K		74
37 Non-dimensional temperature across z -axis at 800 K		74
38 Non-dimensional temperature across z -axis at 1500 K		75
39 Non-dimensional temperature across z -axis at 300 K, 800 K and 1500 K		75
40 Heat flux across z -axis at 300 K		76
41 Heat flux across z -axis at 800 K		76
42 Heat flux across z -axis at 1500 K		77

LIST OF FIGURES (Continued)

<u>Figure</u>		<u>Page</u>
43 Heat flux across z -axis at 300 K, 800 K and 1500 K		77
44 Mean heat flux across z -axis at 300 K, 800 K and 1500 K		78
45 κ across z -axis at 300 K		79
46 κ across z -axis at 800 K		79
47 κ across z -axis at 1500 K		80
48 Thermal conductivity across z -axis at 300 K, 800 K and 1500 K versus Du et al.		80
49 Defect collection		89
50 Anisotropy ratios		90
51 Thermal conductivities along z -axis		91

LIST OF TABLES

<u>Table</u>		<u>Page</u>
1 Simulation convergence parameters		46
2 Thin film simulation parameters		50
3 Thin film simulation statistics		50
4 Quadrature study statistics		52
5 Mesh study statistics		53
6 Al-Si simulation parameters		56
7 Al-Si simulation statistics		56
8 Graphite simulation parameters		62
9 Graphite simulation statistics		62
10 Single crystal UO ₂ simulation parameters		66
11 Single crystal UO ₂ simulation statistics		66
12 Experimentally determined mean free path		67
13 κ in varying cell length		68
14 Thermal conductivity comparison		71
15 Values of Λ		72
16 UO ₂ + Xe simulation parameters		72
17 UO ₂ + Xe simulation statistics		73
18 Mean heat flux in UO ₂ + Xe		78
19 Thermal conductivity in UO ₂ with Xe		81

PREDICTING THERMAL CONDUCTIVITY IN NUCLEAR FUELS USING RATTLESNAKE-BASED DETERMINISTIC PHONON TRANSPORT SIMULATIONS

1 INTRODUCTION

Determining thermal conductivity in nuclear fuel has been a focus in the engineering community for decades. The precise knowledge of thermal conductivity in nuclear fuel is necessary for the safe operation of a nuclear reactor. Historically, thermal conductivity has been characterized through experiment [1–5] by performing thermal resistance measurements on the microstructure in fuel with varying isotopic (fission product) compositions. These are destructive and time consuming measurements, as they involve the physical sectioning of fuels with operating histories. This method does not consider the constantly changing concentration of isotopic byproducts in the fuel, nor has it historically provided appropriate values across a wide range of reactor operating conditions without significant interpolation error.

Due to the large uncertainties in the experimentally calculated values of thermal conductivity for nuclear fuel, nuclear power plants have been built with wide safety margins to account for effects seen in the fuel at high temperatures and concentrations of fission product defects. A rapid, simulation-based, predictive approach to determining thermal conductivity as a function of the operating history of the fuel intrinsic to a power plant would yield a better understanding of heat transport in the reactor core.

Characterization of nuclear fuel material properties is an active area of research. At the fundamental level, effects such as fuel cracking, physical strain, plutonium migration and void formation among others are being computationally modeled at

the nanoscale. These efforts are necessary for the continued development of nuclear fuel and advanced Generation IV nuclear reactors [6–10].

In the nanoscale regime, heat transport behaves differently than the classical macroscale model of Fourier. In the Fourier regime, thermal conductivity is related to the heat flux and temperature gradient through a material

$$\mathbf{q} = -\kappa \nabla T. \quad (1)$$

Unfortunately, the Fourier model of heat conduction is unable to capture all of the detailed physical processes which affect heat transport at the molecular level. The chief object of interest in this research is the phonon.

Phonons are a collection of longitudinal vibrations in an atomic lattice, also known as lattice waves. Phonons are quanta of energy which are generated by atomic displacements in the lattice due to applied temperature gradients. These lattice waves tend to be in the lower wavelength limit and could be viewed as an analog to sound waves. Phonons have a similar relation to the vibrations in a solid as photons do to the vibrations of an electromagnetic field [11]. However they are not truly particles such as photons or neutrons and are often described as ‘quasiparticles’. The physics and mechanics of phonons are further discussed in Section 2.

The goal of this work is to provide a deterministic phonon transport modeling capability for heterogeneous nuclear fuel with fission product defects. The fission product which most greatly impedes thermal transport is xenon, a noble gas which greatly degrades thermal conductivity in operating nuclear fuel over its life cycle [9, 10]. The Self-Adjoint Angular Flux formulation is used as the spatial discretization of the Boltzmann transport equation for phonons. The objective in applying this deterministic method is to greatly enhance the speed of thermal con-

ductivity calculations. The bulk of phonon transport work is done at the atomic scale through the use of molecular dynamics methods. Molecular dynamics is effective in predicting thermal conductivity, but can only model small systems of atoms due to the exceedingly high computational demand of the method.

To accomplish our goal, the neutron transport code Rattlesnake is tested as the phonon transport engine. Rattlesnake is a neutron transport code which uses the Self-Adjoint Angular Flux formulation spatially discretized in finite elements. Rattlesnake is a part of the Multiphysics Object Oriented Simulation Environment (MOOSE) architecture developed and maintained by Idaho National Laboratory (INL). These codes are discussed in Section 3. We employ Rattlesnake to show that a neutron transport code may be adapted to transport phonons (with some slight modifications) and to connect transport phenomena at the nanoscale to properties which are to be used at the macroscale (temperature, heat flux and thermal conductivity).

A variety of computational phonon transport approaches have been investigated. Three primary techniques are applied: Monte Carlo (MC) algorithms, molecular dynamics (MD) applications, and numerical solutions of the Boltzmann transport equation (BTE). Much of the attention to phonon transport is in the nanoscale regime, where length scales of material approach the magnitude of the phonon mean free path, and heat transport deviates from the Fourier law and instead follows solutions of the BTE. A majority of the work outlined in the open literature is on thin films and small volumes of material. The following literature review outlines some of the past and current work detailing the process of phonon transport. The focus is narrowed to investigate phonon transport in nuclear fuel with xenon cluster defects.

1.1 Literature Review

This section gives a review of the three primary methods (Monte Carlo, molecular dynamics and deterministic) used to computationally model phonon transport. A history of each is described and a discussion of work leading up to present day efforts is presented. The focus of this review narrows to investigate the state of phonon transport in nuclear fuel, with and without fission product defects.

1.1.1 Monte Carlo Approaches in Phonon Transport

Monte Carlo (MC) algorithms have been applied in many situations where an exact numerical solution of the BTE is difficult to obtain. MC techniques use algorithms which simulate the Brownian motion (a “random walk”) of particles in a medium, tracking the interactions of the particles using probability distribution functions, resulting in a net particle distribution over the spatial range of the medium. MC is often employed as a ‘benchmark’ solution other numerical solutions.

The work of Klitsner [12] combined experiment with a Monte Carlo algorithm to add quantitative analysis to their collected data. Klitsner examined polished single crystals of silicon at low temperatures, where phonon boundary scattering effects dominate. This was an investigation into phenomena first outlined by Casimir [13] in which phonons would only scatter at surfaces within the crystal. This effect is amplified at low temperatures where the surfaces are polished to the extent they act like mirrors, e.g., are highly specular, leading to diffusion as the dominant scattering mechanism. At low temperatures, other scattering processes such as normal, Umklapp and intrinsic scattering are minimized due to the low vibrational frequencies in the crystal [11].

Mazumder and Majumdar [14] studied phonon transport in thin films and took into consideration the phonon dispersion relation and polarization modes. If the dispersion relation is neglected, this assumption may drastically affect the phonon mean free path. In addition, the multiple phonon polarizations were assumed to be composed of a single, average polarization branch. These assumptions simplify the transport calculation, but may greatly reduce the accuracy of the solution. Monte Carlo schemes are advantageous because they capture the individual, anharmonic phonon scattering events which are sometimes simplified by the means of the relaxation time approximation [11]. Furthermore, the use of MC allows for the incorporation of a general spatial grid, which has been a limitation of deterministic methods.

Mazumder and Majumdar used Monte Carlo to solve two and three dimensional frequency dependent phonon transport problems in both silicon and gallium-arsenide thin films. They allowed for phonon drift and scatter in a transient simulation [14]. Boundary conditions were incorporated for both isothermal and adiabatic problems.

These simulations generated results that compared very favorably with past experiments in thin films. However, Monte Carlo techniques are computationally intensive and the numerical error is directly affected by the number of samples chosen for the simulation. These simulations of a simple geometry required three hours of computer time on a 500 MHz computer workstation [14].

Lacroix and Joulain [15] constructed a MC package which simulated phonon transport with the relaxation time approximation for the collisional term. This code gave comparisons to analytical solutions in the diffusive scattering regime, and was tested on silicon and germanium thin films.

1.1.2 Molecular Dynamics Methodology

Molecular Dynamics (MD) has been used to simulate phonon transport since the 1950s [16]. Molecular dynamics is a technique which can simulate a system of atoms ranging in size from tens to millions and is based on a numerical integration of Newton's equation of motion [16]. The method simulates the interactions of atoms using a wide array of potential models, which describe various types of atomic motion and interaction. The interactions are not necessarily restricted to atoms; quantities such as dislocations and spins may be simulated as well.

Molecular dynamics makes use of potential models from theory and/or experiment, and these are strongly problem dependent. Some examples of potentials include Lennard-Jones, Mie, Born-Mayer and Morse [17]. Each of these examples belong to the central-force potential category, as they are based on distance between atom pairs. These would be suited to modeling solid material of a simple structure [16].

Two variations of MD phonon transport simulations can be used to determine thermal conductivity or a host of other quantities [6,16–20] - equilibrium molecular dynamics (EMD) and non-equilibrium molecular dynamics (NEMD). EMD relies on a constant temperature, measuring fluctuation decay in a variable, e.g., heat flux, measured to compute thermal conductivity. Alternatively, NEMD uses a temperature gradient within the medium and calculates the temperature difference between the heat source and sink and a measured heat flux to compute thermal conductivity [16]. EMD has the advantage that only one simulation is required to obtain results. These calculations are carried out at a constant temperature, relying on potential models to determine system characteristics. The Green-Kubo method, used by Oliveira [6] and Hori [18] is an EMD approach which is applied to

measure lattice thermal conductivities. It relies on oscillations of the heat current autocorrelation function (HCACF) about equilibrium, and thermal conductivity is inferred from the time taken for the oscillations to vanish.

Large-scale Atomic/Molecular Massively Parallel Simulator (LAMMPS) is a popular software package for MD built and maintained by Sandia National Laboratory [21]. It is a highly parallelizable, open source program written in C++, and contains a vast library of models, atomic potentials, force fields, ensembles and constraints, and is very effective in performing many types of MD simulations including phonon transport. Visual Molecular Dynamics (VMD) is a software package for visualizing and post-processing large systems of molecular data [22]. Both LAMMPS and VMD support graphics processing unit (GPU) accelerated computing.

Molecular dynamics methods provide high fidelity solutions provided the researcher knows how to tune the myriad “knobs” in the simulation program. The largest drawback to MD simulation is the computational power required. For systems with millions of atoms, large scale parallel machines are necessary. For this reason, reported results are limited to the micro- and nano-scale dimensions; translation to engineering scale is not a trivial process.

1.1.3 Deterministic Solution Techniques

Approaching the Boltzmann transport equation with a deterministic methodology results in a system of discretized equations which may then be programmed into a computer and then rapidly solved with a computer. In deterministic methods, the BTE is discretized in all independent variables, i.e., spatial, angular, energy or time. Much work has been performed regarding phonon transport using the BTE

with the angular variable discretized via the discrete ordinates method, which is sometimes referred to as the “ S_N method” [23–39]. Discrete ordinates involves discretizing the angular domain into a series of directions (“rays”) and then solving the transport equation in each direction. This method is outlined in various texts [40–42]. Spherical harmonics (P_N) is another method used to discretize the angular variable in the transport equation. The angular flux is expanded in terms of Laplacian spherical harmonics which represent an orthogonal system.

The Boltzmann transport equation is typically written in “integro-differential” form, which has both a first order differential operator and an integral operator. However, other forms of the transport equation exist. One of these is known as second order (or even-parity) form [41, 42]. The second order formulation has second order differential terms, but gains traction in that the solution need only be over half of the angular domain. This can lead to a more expedient solution of the transport equation, as the computational expense is lessened and can provide a better formulation in the iterative methods required for the solution.

One particular second-order form of the BTE is the Self-Adjoint Angular Flux (SAAF) formulation [43]. Morel and McGhee show the SAAF equation may be derived from the first-order form of the transport equation using an algebraic technique. They also make computational comparisons with the even- and odd-parity equations and provide a derivation of the BTE for neutrons in 1D.

There are numerous advantages to using the self-adjoint property of the equations, which include ease of spatial discretization on multidimensional finite element meshes; doing so with first order methods can prove difficult due to re-entry conditions associated with the discretized cells. In addition, the resulting matrix equations are always symmetric positive definite, and allow use of powerful, ef-

ficient Krylov solution techniques such as the preconditioned conjugate-gradient method. One of the unique attributes of the SAAF equation in contrast to parity methods is that the **full** angular flux is computed, as opposed to just the even-parity or odd-parity component. Reflecting boundary treatments are also easier due to the availability of the full angular flux; the incoming and outgoing directions are coupled in the same manner as the first order transport equation [43].

The SAAF method does have some disadvantages; in applying source iteration, a sparse matrix equation is generated, rather than the more familiar block lower triangular matrix equation. The “sweeping” technique used with S_N discretized first order methods may not be used on the SAAF equation. The treatment of transport through void regions is difficult, because the formulation involves $\frac{1}{\sigma_t}$. In addition, solving the SAAF in purely scattering media is also challenging due to singularities which result when scattering and total cross sections are equal [43].

1.1.4 *Introduction to MOOSE and Rattlesnake*

The Self-Adjoint Angular Flux equation has gained considerable attention with the advent of the code Rattlesnake, a solver for the neutron transport equation which uses the SAAF formulation. Rattlesnake is part of the MOOSE (Multiphysics Object Oriented Simulation Environment) framework which has been developed at Idaho National Laboratory (INL) [44]. MOOSE is a sophisticated framework for solving coupled partial differential equations (PDEs). It is written in C++, is massively parallelizable, and employs a unit-agnostic finite element mesh discretization [44]. The mesh may be either structured or unstructured. Within MOOSE are a number of modules which solve the equations for specific physics applications, e.g., thermal hydraulics, materials science, or probabilistic risk assessment.

Rattlesnake can employ both S_N and P_N angular discretizations, and can use diffusion synthetic acceleration to speed up transport calculations [45, 46]. It can use both continuous and discontinuous finite element methods, diffusion theory, as well as the method of manufactured solutions [47]. It is able to solve transient, eigenvalue and steady state problems. As was mentioned in the previous section, the SAAF can sometimes have difficulty treating void regions. A weak form of the discrete ordinate, SAAF formulation using the Continuous Finite Element Method (CFEM) was developed to mitigate these situations [48].

We aim to show the SAAF-derived BTE for phonons shares similar characteristics to the SAAF form of the BTE for neutrons, and that Rattlesnake may be directly used as a deterministic tool to simulate phonon transport. Rattlesnake may be used as an engine to simulate phonon transport at the engineering scale, bridging the gap between molecular dynamics and the macroscale.

1.1.5 Phonon Transport in UO_2 with Impurities

Recent work investigating the effects of phonon transport in uranium dioxides (both pristine and with impurities) has been primarily conducted by means of MD simulations [8, 9, 49, 50]. Phonon transport in uranium dioxide is of chief importance, due to phonon scattering being the primary mechanism of energy transport in nuclear fuel. UO_2 is the fuel for all light water reactors, and the prediction of thermal conductivity based on phonon transport is becoming more important in the scientific community.

Gofryk et al., Kim et al., and Wang [8, 49, 50] investigated phonon transport contributions to thermal conductivity in pristine (single crystal), thin film uranium dioxide. All used molecular dynamics techniques to simulate phonon transport.

Both EMD and NEMD processes were used. Kim et al. used the Green-Kubo method to compute the HCACF and find the optical phonon transport contribution. Kim et al. and Gofryk et al. reported using the phonon dispersion relation to obtain group velocities. Kim et al. also used a non-equilibrium *ab-initio* MD (NEAIMD) method using density functional theory (DFT) to compute thermal conductivity values. In all non-equilibrium techniques, temperature gradients were applied to compute thermal conductivity using the Fourier law.

Simulations of single crystal UO₂ typically involve rectangular, parallelepiped cells. Size effects play an important role in determining scattering contributions at cell boundaries and grain boundaries, which must be accounted for in the simulation. Both EMD and NEMD have different advantages and drawbacks. The EMD method offers reliable, size-agnostic results provided the simulation size is appropriate ($\sim 10,000$ atoms). NEMD methods have a strong dependence on the size of the sample (length and atom count) and the established temperature gradient. Results from this study are compared against results from classical molecular dynamics (CMD) simulations, in order to reduce artifacts of simulations.

Uranium dioxide takes the crystalline form of a stable fluorite structure (CaF₂, space group *Fm3m*) with 4 U⁺ and 8 O²⁻ ions. UO₂ is cubic in its point and space groups; cubic structures exhibit symmetric behaviors, therefore UO₂ should show isotropy in the second rank tensor property of thermal conductivity. Grofryk et al. hypothesized a hidden anisotropy in UO₂, which might help to explain scattering behavior in single crystals of UO₂ that has been observed in samples with impurities or measurement errors [8]. Gofryk et al. proposed that the recognized anisotropy is a result of applied temperature gradient interaction with electric moments on the uranium atoms, which affect phonon spin to marginally “break” cubic symmetry.

They report the effect on magnetic properties of UO₂ and degenerate bands as generating Jahn-Teller distortions [8, 51]. This anisotropic effect was observed for MD simulations of UO₂ at lower (4K - 300K) temperatures, and may not have a pronounced effect on uranium dioxide at high temperatures. Kim et al. also cite a polaron hopping mechanism to explain some high temperature, anisotropic thermal conductivity behaviors in UO₂ [49].

Molecular dynamics methods are beneficial in that they incorporate a variety of conditions which affect phonon scattering and impact thermal conductivity. Fuel porosity, grain boundary scattering, thermal boundary resistance, and boundary scattering are all scattering phenomena which are included naturally in MD. This is the primary advantage of MD simulations - the ability to record singular interaction mechanics. However, tracking singular interactions has the disadvantage of being very computationally expensive.

Understanding the effect of impurities on phonon scattering in UO₂ is critical, due to the constantly changing environment which develops as nuclear fuel undergoes the fission process. The fuel microstructure is affected by the fission process through the formation of isotopic decay products. It is due to these fission products that thermal conductivity changes by an appreciable amount while the fuel undergoes irradiation in a nuclear reactor. Of these products, xenon remarkably affects the transport of phonons in uranium dioxide. Because modeling a wide array of fission products in fuel would be very computationally expensive, we can focus on xenon because of its marked effect on thermal conductivity [9].

1.1.6 Effects of Xenon on UO_2 Thermal Conductivity

Du et al. examined the presence of xenon on phonon scattering in uranium dioxide. They cite xenon as the “most important fission gas” and examine the effect of xenon atoms dispersed in the UO_2 lattice and the impact of quantized xenon bubbles in the matrix. The reasons for analyzing xenon in both forms are twofold; although xenon will be present in bubbles after annealing, it will also be dispersed in the UO_2 matrix as individual molecules or in small clusters [9]. Du et al. construct models and perform calculations which reflect this.

The Callaway model was used to parameterize the relation between thermal conductivity, volumetric heat capacity, group velocity and effective mean free path. The Callaway model uses the Debye approximation which results in a temperature and frequency dependent model for lattice thermal conductivity. This model is able to resolve individual phonon scattering mechanisms including Umklapp processes, boundary scattering and point defect scattering [9], which are processes related to the relaxation time.

In simulations of xenon dispersed randomly in the UO_2 matrix, Du et al. reported a decrease in thermal conductivity as a result of the increased phonon scattering by defects. Temperatures were varied for each simulation and a temperature gradient was applied which, implies the use of NEMD methodology. Simulations were performed in rectangular box system geometries with a 3.8 nm x 3.8 nm area, and lengths between 26 nm and 75 nm. Different box lengths are used to capture thermal conductivity for multiple mean free path lengths of phonons in UO_2 . They used three concentrations of xenon: 0.303, 0.612 and 0.927 atom percent xenon. The simulation cells used did not have boundaries, in theory boundary scattering should not contribute to the overall scattering rate. However, due to the hot and

cold plates used to apply the temperature gradient, boundary scattering was not completely eliminated [9].

The focus of this paper is on the modeling of quantized bubbles of xenon in the uranium dioxide lattice, which includes grain boundary interaction. Five types of structure were analyzed at a temperature of 300 K in simulation boxes of 3.8 nm x 3.8 nm area and lengths between 8 nm and 60 nm. These structures were: Type I: one Xe bubble and no grain boundary; Type II: grain boundary and no Xe atoms; Type III: grain boundary and randomly distributed Xe atoms corresponding to Xe concentrations of one or three bubbles; Type IV: one Xe gas bubble on the grain boundary; and Type V: one or three Xe bubbles near the grain boundary [9]. Thermal conductivity is computed for three crystal directions of (100), (110) and (111) at temperatures of 300 K, 800 K and 1500 K.

Du et al. found the presence of Xe and grain boundaries to reduce thermal conductivity in all simulations and at all temperatures. They report that a random dispersion of xenon throughout the UO₂ structure reduces reducing thermal conductivity more than the presence of xenon bubbles. This is due to the random xenon atoms decreasing the phonon mean free path, while the bubbles act more as defect centers which change the local behavior of the phonon scattering. The bubbles have a much larger relative separation compared to the distributed Xe atoms, which strengthens the case for the greater impact of phonon scattering among the dispersed Xe.

Du et al. make a final point of computing thermal conductivity in the 100, 110 and 111 directions in bulk UO₂ to gain an understanding of the anisotropy. This anisotropy was also reported in [8, 49, 50], though the authors offer different explanations for its presence. Anisotropy is an unexpected result and merits further

study [9].

1.2 Thesis Overview

The remainder of this thesis is organized as follows:

- II. Chapter 2 introduces the generalized Boltzmann transport equation for phonons. Various phonon scattering mechanics are discussed and connections to transport processes are made. The Self-Adjoint Angular Flux formulation is introduced.
- III. In Chapter 3, the Boltzmann equation for phonons is derived in the SAAF formulation. A discretization of the equations is provided and proper boundary conditions are defined. Results of tests with this code are discussed. MOOSE and Rattlesnake are introduced.
- IV. Chapter 4 provides the results of each phonon transport test problem. Input conditions for each simulation case are discussed. Tables of data and plots of simulations are presented.
- V. Chapter 5 contains an analysis and discussion of the results from the phonon transport simulations. We conclude by assessing the progress made toward our research objectives, and suggest potential future work.

2 PHONON TRANSPORT PHYSICS

2.1 Introduction

The generalized Boltzmann transport equation is used in many areas in the transport community. In nuclear engineering, the community is most familiar with the neutral particle form of the equation. Phonons are uncharged, like neutrons, which greatly simplifies the mathematical description of their behavior. Phonon scattering processes are discussed here, along with a brief introduction to some of the underlying physics associated with phonons in the atomic lattice.

2.2 The Boltzmann Transport Equation for Phonons

Phonons inhabit the boson class of elementary particles and follow Bose-Einstein statistics. Their direct counterpart is the fermion (neutrons, electrons), which follow Fermi-Dirac statistics - the identifying quality being that two fermions may not occupy the same quantum state, as prescribed by the Pauli exclusion principle. Phonon multiple occupation is characterized by the Bose-Einstein distribution function:

$$\langle f_\omega \rangle = \frac{1}{\exp\left(\frac{\hbar\omega}{k_B T}\right) - 1} \quad (2)$$

where \hbar is the reduced Planck's constant, ω is the phonon frequency, k_B is Boltzmann's constant and T is temperature. The generalized Boltzmann transport equation for a distribution function f_ω , considering streaming, influence of external fields and scattering, is

$$\dot{f}_\omega = \dot{f}_{\omega|\text{stream}} + \dot{f}_{\omega|\text{ext}} + \dot{f}_{\omega|\text{scatt.}} \quad (3)$$

Expanding these contributions yields the form

$$\frac{\partial f_\omega}{\partial t} + v_g \boldsymbol{\Omega} \cdot \nabla f_\omega + \frac{e}{\hbar} \left(\mathbf{E} + \frac{1}{c} v_g \wedge \mathbf{H} \right) \cdot \frac{\partial f_\omega}{\partial \omega} = \dot{f}_{\omega|\text{scatt}}. \quad (4)$$

In a steady state nuclear heat generation environment (nuclear fuel at operating temperatures) we assume no external electrical or magnetic field. Equation (4) simplifies to

$$v_g(\omega, \mathbf{k}) \boldsymbol{\Omega} \cdot \nabla f_\omega = \dot{f}_{\omega|\text{scatt}}. \quad (5)$$

The $\dot{f}_{\omega|\text{scatt}}$ includes all the mechanisms by which phonons may scatter. Often, this scattering kernel is simplified by use of the relaxation time approximation as described by Kittel and Ziman [11, 52]:

$$\dot{f}_{\omega|\text{scatt}} = \frac{f_\omega^0 - f_\omega}{\tau_c}. \quad (6)$$

Equation (6) expresses the degree of separation of the phonon distribution from its equilibrium value, on a per unit time basis. If a temperature gradient or external field does not exist, then $f_\omega^0 - f_\omega = 0$ and the scattering term vanishes. In solving for the phonon distribution f_ω at spatial location \mathbf{r} , f_ω only shifts a small amount from its local equilibrium distribution f_ω^0 . The equilibrium distribution is fixed by the local temperature at \mathbf{r} . For small deviations of the phonon distribution function from the equilibrium state, the scattering term may be expressed by Eq. (6). τ_c is the composite relaxation time, or mean time between scattering events. This parameter is typically on the order of 10^{-15} s, but varies depending on the scattering process [11].

Substitution of Eq. (6) into Eq. (5) will result in

$$\Lambda \boldsymbol{\Omega} \cdot \nabla f_\omega = f_\omega^0 - f_\omega \quad (7)$$

which is the modified form of the BTE for phonons. Here relaxation time τ_c has

been multiplied to the left hand side with group velocity v_g which results in the phonon mean free path Λ - the mean distance traveled between scattering events.

2.2.1 Gray Phonon Transport

Now, the transformation of the frequency dependent BTE into a frequency independent equation for a gray medium may be performed.

$$\Lambda \boldsymbol{\Omega} \cdot \nabla f_\omega(\mathbf{r}, \omega, p, \theta, \phi) = f_\omega^0(\mathbf{r}, \omega, p, \theta, \phi) - f_\omega(\mathbf{r}, \omega, p, \theta, \phi). \quad (8)$$

Multiplying Eq. 8 by $v_g \hbar \omega \mathcal{D}(\omega)$, summing over three phonon polarizations, and integrating over all possible frequencies the gray phonon intensity is defined:

$$I(r, \theta, \phi) = \frac{1}{4\pi} \int_0^{\omega_{limit}} \sum_p v_g \hbar \omega \mathcal{D}(\omega) d\omega. \quad (9)$$

Here $\mathcal{D}(\omega)$ is phonon density of states per volume and v_g is the phonon velocity. Operating on Equation 8 as just described yields

$$\Lambda \boldsymbol{\Omega} \cdot \nabla I(\mathbf{r}, \theta, \phi) = I^0(\mathbf{r}, \theta, \phi) - I(\mathbf{r}, \theta, \phi), \quad (10)$$

$$\Lambda = v_g \cdot \tau_c \quad (11)$$

where,

$$\begin{aligned}
v_g &= \text{phonon group velocity}, \\
\tau_c &= \text{relaxation time}, \\
\Lambda &= \text{mean free path, average distance phonons travel before next scattering event} \\
\Omega &= \frac{\mathbf{v}_g}{|\mathbf{v}_g|}; \text{unit vector for phonon direction polar and azimuthal components,} \\
I(\mathbf{r}, \theta, \phi) &= \text{phonon intensity distribution at position } \mathbf{r}, \text{ in polar and azimuthal directions,} \\
I^0(\mathbf{r}, \theta, \phi) &= \text{phonon equilibrium intensity distribution at position } \mathbf{r}, \text{ in polar and azimuthal directions,}
\end{aligned}$$

The right hand side of Eq. (10) implies the restoration of thermal equilibrium, by interactions of phonons with electrons, other phonons, etc. Equation (10) the equation of phonon radiative transfer (EPRT) [23].

Three quantities are of interest in this research: temperature, heat flux and thermal conductivity. Numerical solutions to the EPRT generate a phonon angular intensity, which may be integrated over solid angle to obtain scalar phonon intensity. From this zeroth angular moment, temperature is calculated through the relation

$$T = \frac{4\pi I}{C_v v_g}. \quad (12)$$

Heat flux is the first angular moment of phonon intensity

$$q(\mathbf{r}) = \int_{4\pi} I(\mathbf{r}, \Omega) \Omega d\Omega. \quad (13)$$

Thermal conductivity can be calculated in a number of ways. In their molecular dynamics simulations, Gofryk et al. [8] and Du et al. [9] used the Callaway model to calculate lattice thermal conductivity

$$\kappa_L(T) = \frac{k_B}{2\pi^2 v} \left(\frac{k_B T}{\hbar} \right) \int_0^{\Theta_D} \frac{\tau_p x^4 e^x}{(e^x - 1)^2} dx, \quad (14)$$

where τ_p is the total relaxation time contribution, k_B is Boltzmann's constant and $x = \frac{\hbar\omega}{k_B T}$. They used this continuum model to compare against MD simulations of thermal conductivity in uranium dioxides. In this research, thermal conductivity is calculated through the Fourier equation of thermal conductivity

$$\kappa = -\frac{\mathbf{q}}{\nabla T}, \quad (15)$$

where the components \mathbf{q} and ∇T are obtained through taking angular moments of phonon intensity. In this approach, an average thermal conductivity for the bulk can be computed by taking the spatial average of the ratio of heat flow through the material to the temperature gradient, the rate which temperature changes the most rapidly about some local point.

Though heat flux and temperature are calculated in all spatial dimensions, the dimension of interest is one where a temperature gradient is applied. This methodology is applied to myriad MD simulations, and is repeated here.

2.2.2 The Self-Adjoint Angular Flux Formulation

Morel and McGhee [43] outline an algebraic technique for the derivation of a self-adjoint form of the transport equation. From a computational perspective, a second order form such as the Self-Adjoint Angular Flux is advantageous as the full angular flux becomes the unknown. Here, a derivation of the EPRT in the Self-Adjoint Angular Flux formulation is shown.

In Section 2.2, the three-dimensional frequency independent EPRT was derived. To derive the SAAF form of the EPRT, isolate the phonon intensity $I(\mathbf{r}, \theta, \phi)$:

$$I(\mathbf{r}, \theta, \phi) = I^0(\mathbf{r}, \theta, \phi) - \Lambda \boldsymbol{\Omega} \cdot \nabla I(\mathbf{r}, \theta, \phi), \quad (16)$$

and then substitute this expression into Eq. (10)

$$\Lambda \boldsymbol{\Omega} \cdot \nabla [I^0(\mathbf{r}, \theta, \phi) - \Lambda \boldsymbol{\Omega} \cdot \nabla I(\mathbf{r}, \theta, \phi)] = I^0(\mathbf{r}, \theta, \phi) - I(\mathbf{r}, \theta, \phi). \quad (17)$$

Next, distribute the coefficients and gradient

$$\Lambda \boldsymbol{\Omega} \cdot \nabla I^0(\mathbf{r}, \theta, \phi) - \Lambda \boldsymbol{\Omega} \cdot \nabla [\Lambda \boldsymbol{\Omega} \cdot \nabla I(\mathbf{r}, \theta, \phi)] = I^0(\mathbf{r}, \theta, \phi) - I(\mathbf{r}, \theta, \phi), \quad (18)$$

and collect like terms on each side of the equation:

$$I(\mathbf{r}, \theta, \phi) - \Lambda \boldsymbol{\Omega} \cdot \nabla [\Lambda \boldsymbol{\Omega} \cdot \nabla I(\mathbf{r}, \theta, \phi)] = I^0(\mathbf{r}, \theta, \phi) - \Lambda \boldsymbol{\Omega} \cdot \nabla I^0(\mathbf{r}, \theta, \phi). \quad (19)$$

Equation (19) is the SAAF form of the EPRT.

From the implications of the relaxation time approximation, the phonon equilibrium intensity will be defined with a condition of zero heat generation, $\nabla \cdot \mathbf{q} = 0$. This suggests that phonon radiative equilibrium could exist at all possible frequencies, though applied temperature gradients make non-equilibrium conditions possible in certain situations [23].

2.2.3 Definition of Equilibrium Intensity

The equilibrium intensity $I^0(\mathbf{r}, \theta, \phi)$ is now given treatment to define it as a purely spatial function. First, multiply Eq. (10) by $d\Omega$ and integrate over solid angle, with an approach similar to one taken by Yilbas and Bin Mansoor [25], where

$$d\Omega = \sin \theta d\theta d\phi, \quad (20)$$

$$\boldsymbol{\Omega} \cdot \nabla I = \sin \theta \cos \phi \frac{\partial I}{\partial x} + \sin \theta \sin \phi \frac{\partial I}{\partial y} + \cos \theta \frac{\partial I}{\partial z}. \quad (21)$$

Using these expressions in Eq. (10) and bringing Λ to the right hand side gives

$$\int_{4\pi} \boldsymbol{\Omega} \cdot \nabla I(\mathbf{r}, \theta, \phi) d\Omega = \frac{1}{\Lambda} \left[\int_{4\pi} I^0(\mathbf{r}, \theta, \phi) d\Omega - \int_{4\pi} I(\mathbf{r}, \theta, \phi) d\Omega \right], \quad (22)$$

and heat flux in directions x, y, z is defined as

$$\int_0^{2\pi} \int_0^\pi \frac{\partial I}{\partial x} \sin^2 \theta \cos \phi d\theta d\phi = q_x, \quad (23)$$

$$\int_0^{2\pi} \int_0^\pi \frac{\partial I}{\partial y} \sin^2 \theta \sin \theta d\theta d\phi = q_y, \quad (24)$$

$$\int_0^{2\pi} \int_0^\pi \frac{\partial I}{\partial z} \sin \theta \cos \theta d\theta d\phi = q_z. \quad (25)$$

Applying the law of energy conservation and implementing the assumption of steady state conditions with no internal heat generation, the heat flux vector is zero and removed from the equation

$$\int_0^{2\pi} \int_0^\pi \Omega \cdot \nabla I(\mathbf{r}, \theta, \phi) d\Omega = \nabla \cdot \mathbf{q} = q_x + q_y + q_z = 0. \quad (26)$$

The relationship between phonon intensities is now

$$\int_0^{2\pi} \int_0^\pi I^0(\mathbf{r}, \theta, \phi) \sin \theta d\theta d\phi = \int_0^{2\pi} \int_0^\pi I(\mathbf{r}, \theta, \phi) \sin \theta d\theta d\phi \quad (27)$$

From the assumption that phonon equilibrium intensity is only a function of space (distribution at equilibrium temperature in the material), it may be removed from the integral. This leads to

$$I^0(\mathbf{r}) = \frac{1}{4\pi} \int_0^{2\pi} \int_0^\pi I(\mathbf{r}, \theta, \phi) \sin \theta d\theta d\phi. \quad (28)$$

Substituting the expression in Eq. (28) back into Eq. (19) gives the result

$$\begin{aligned} I(\mathbf{r}, \theta, \phi) - \Lambda \Omega \cdot \nabla [\Lambda \Omega \cdot \nabla I(\mathbf{r}, \theta, \phi)] = \\ \frac{1}{4\pi} \left[\int_0^{2\pi} \int_0^\pi I(\mathbf{r}, \theta, \phi) \sin d\theta d\phi - \Lambda \Omega \cdot \nabla \int_0^{2\pi} \int_0^\pi I(\mathbf{r}, \theta, \phi) \sin d\theta d\phi \right], \end{aligned} \quad (29)$$

which is the SAAF form of the EPRT solely in terms of phonon intensity $I(\mathbf{r}, \theta, \phi)$.

2.3 Phonon Interaction Processes

Kinetic excitation of the atomic lattice due to an applied temperature gradient produces a quasi-particle in the boson family known as a phonon. The vibrational wave associated with the creation of a phonon can be viewed as a series of harmonic oscillators, a chain of atoms connected through springs. The motion of an atom creates waves which transmit information to the surrounding atoms in the chain.

Phonons are the dominant mechanism through which energy is transported in ceramic based materials, a class that includes fuels such as UO_2 , PuO_2 and the solid neutron moderator graphite. Thermal conductivity is a second rank tensor property of crystalline lattices, and is maximized when long range order is preserved though this generally occurs at low temperatures. Phonon scattering disrupts energy transport through crystalline structures, so it is important to understand different types of scattering and their effects in order to precisely characterize thermal conductivity in ceramic materials.

Phonons follow the Bose-Einstein distribution function, have an integer spin, and are not conserved through scattering unlike electrons or neutrons. Though phonons are categorized here and in literature [11, 52, 53] as particles, inhabit a probability distribution function and their motion can be simulated through the application of the Boltzmann transport equation (BTE), they are lattice waves (with an associated energy, frequency, polarization, and velocity) created as a function of an applied temperature gradient.

The motion of phonons results in the divergence of the system from thermodynamic equilibrium. Phonons scattering with each other (normal or Umklapp processes) aids in restoring thermodynamic equilibrium. In the presence of a temperature gradient where the size of the system is larger than the mean free path of

the phonons, diffusive transport processes dominate [23–28]. In this diffusive limit, equilibrium can be restored and heat transfer can be modeled using the Fourier law of conduction. Alternatively, if the size of the system is smaller than the mean free path of phonons, ballistic transport will be the primary scattering behavior, equilibrium may not exist and the Fourier law is not applicable to describe conduction [11, 52, 53].

The focus of this section is to describe the important physical processes affecting phonon transport and the dominant scattering mechanisms which affect transport behavior.

2.3.1 The Dispersion Relation

By strict definition, phonons are a collection of lattice waves generated by atomic displacements in materials with crystalline structure. The dispersion relation relates the phonon frequency to its wave vector. In a 1D system of atoms, the forces on the system acting to the left and right are

$$\begin{aligned} F_{\text{left}} &= K(u_n - u_{n-1}) \\ F_{\text{right}} &= K(u_{n+1} - u_n) \end{aligned}, \quad (30)$$

where u_n is the displacement of an atom from its equilibrium position n and K is a force constant given by the second derivative of the potential energy between atoms

$$K = \frac{\partial^2 V}{\partial x^2}. \quad (31)$$

The net force on the system is then

$$M\ddot{u}_n = K(u_{n+1} - 2u_n - u_{n-1}) \quad (32)$$

where \ddot{u}_n is the acceleration of atom n and M is the mass of the atom. The displacement $u_n(x)$ of atom n can be found through the solution of the force

system

$$u_n(x) = A \exp [i(kx_n^0 - \omega t)], \quad (33)$$

where Eq. (33) is an equation of motion, k is the wavevector related to wavelength by $k = \frac{2\pi}{\lambda}$, x_n^0 is the equilibrium position of the atom, ω is frequency and t is time. Using Eq. (33), Eq. (32) has the solution

$$-\omega^2 M = K [\exp(ika) - 2 + \exp(-ika)], \quad (34)$$

where a is the lattice spacing. Eq. (34) can be simplified to

$$\omega^2 M = 4K \sin^2 \left(\frac{ka}{2} \right). \quad (35)$$

For a system of two atoms, the equation of motion for the other atom is

$$m\ddot{u}_n = K(u_n - 2u_{n-1} - u_{n-2}). \quad (36)$$

The solution with these systems for ω^2 is

$$\omega^2 = \frac{K(M+m)}{Mm} \pm K \left[\left(\frac{(M+m)}{Mm} \right)^2 - \frac{4}{Mm} \sin^2 \left(\frac{ka}{2} \right) \right]^{\frac{1}{2}}, \quad (37)$$

where M is the mass of atom 1 and m is the mass of atom 2.

Equation (37) is the dispersion relation for the atomic system. Phonons will appear in either the acoustic (+) or optic branch (-). In the optical branch phonons are out of phase; atoms are displaced in opposite directions and wave vectors move against each other. In the acoustic branch, phonons are in phase and wave vectors travel in the same direction. Longitudinal displacements have a parallel orientation and transverse displacements are perpendicular [11, 52].

The dispersion relation is always shown for the first Brillouin zone, which is the Wigner-Seitz cell (see Fig. 1 [52]) in the reciprocal (k^{-1}) lattice space. The

reciprocal lattice is connected to the interatomic spacing a by $\mathbf{G} = w \frac{2\pi}{a}$ where w is an integer value. The first Brillouin zone ($w = 1$) forms a square with side lengths $\frac{\pi}{a}$ around a particular atom. The behavior of solutions in this first zone will be the same as in the entire medium, and this zone is of interest in determining the group velocity of phonons.

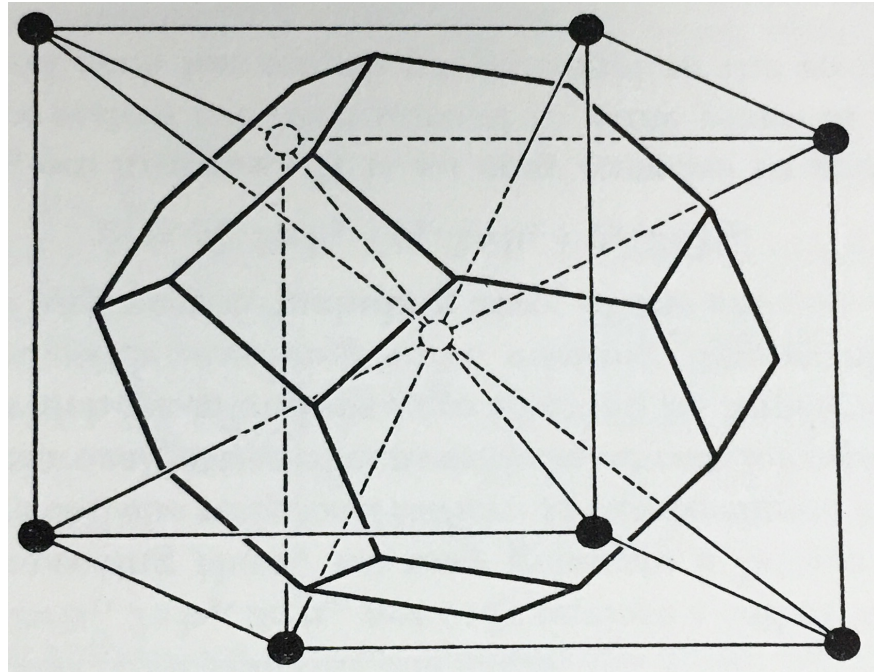


Figure 1: Wigner-Seitz cell for a BCC lattice

These wave vectors possess a cyclical symmetry corresponding to the symmetry of the lattice

$$\mathbf{k} + 2n\pi \equiv \mathbf{k}, \quad n = 1, 2, \dots, N \quad (38)$$

where there are N wave numbers for N lattice sites and a short range $-\pi \leq \mathbf{k} \leq \pi$ is typically chosen [52]. With this consideration, short and long wavelengths may represent the same lattice displacement.

Phonon group velocity is obtained by taking the derivative of the acoustic branch in the dispersion relation. The slope of the derivative in the acoustic branch is much greater than the optic branch (optic phonons are out of phase); as a result we do not consider a velocity contribution from the optic branch. Frequency is a function of wavenumber and taking the derivative with respect to wavenumber gives

$$v_g(\omega, k) = \frac{\partial\omega(k)}{\partial k}. \quad (39)$$

2.4 Relaxation Time Contributions

In many phonon transport simulations, the scattering operator is transformed through the application of the relaxation time approximation [11, 52]. The relaxation time is a function of the underlying scattering processes which take place at the atomistic scale. The total inverse relaxation time is the sum of the inverse times associated with each scattering process. All of the contributions are additive through Matthiessen's rule:

$$\tau_p^{-1} = \tau_B^{-1} + \tau_D^{-1} + \tau_U^{-1}, \quad (40)$$

where τ_B is contribution from size effects, τ_D is the point defect contribution and τ_U are contributions from normal and Umklapp processes. Each of these scattering processes are outlined in the following sections.

2.4.1 Size Effects

Changes in scattering behavior can occur when length scales are on the order of the phonon mean free path. Phonon transport is generally simulated with an applied temperature gradient in a single dimension of a multi-dimensional geometry.

Phonon intensity at the boundary is defined by:

$$I_b = \frac{C_p v_g T}{4\pi}, \quad (41)$$

where C_p is volumetric specific heat, v_g is group velocity, and T is the temperature at the specified boundary. Figure 2 is a plot of non-dimensional temperatures in silicon with differing acoustic thicknesses.

At the boundaries of Fig. 2, the non-dimensional temperature values do not reflect the prescribed temperature boundary conditions. The expected solution that would correspond to $T_L = 301\text{ K}$ and $T_R = 300\text{ K}$ is shifted on each border due to size effects in the material. It is evident from these variations that as problem size grows or shrinks to approach the Casimir limit [13], the phonon intensity shifts and results in step changes at the boundaries. The Casimir limit is a condition in which the length scale of the problem is that of the phonon mean free path, and ballistic scattering becomes dominant. Some of the phonon flux is reflected outright rather than contributing to the magnitude at the opposing boundary. The closer the emissive planes, the more pronounced the effect.

2.4.2 Normal and Umklapp Processes

Most phonon transport simulations assume harmonic (isotropic) behavior in the scattered phonons. However, anharmonic scattering effects can occur as temperatures increase. This is an important mechanism to consider in phonon transport in nuclear fuel, which is characterized by its high operating temperatures.

The assumption of potential energy being a function of the position vectors is described in Ziman [52] and Srivastava [53], using the adiabatic approximation. The approximation states that the electron cloud surrounding atoms may be neglected in the description of displaced atoms in the system. This justification

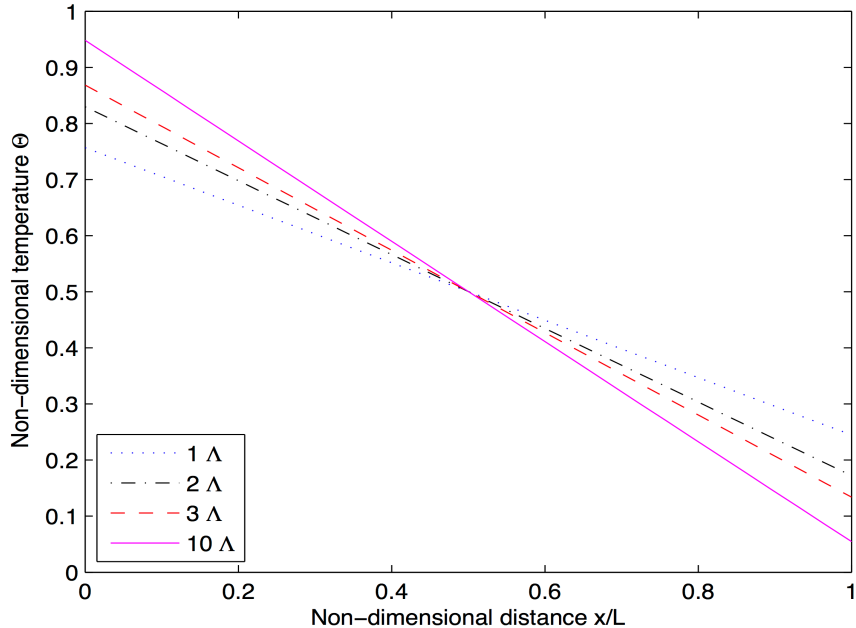


Figure 2: Scattering change due to size effects in silicon

involves the notion that the electrons move so quickly that the electronic coordinates are a function of the nuclear coordinates [52]. The Hamiltonian of the system can be written as

$$\mathcal{H} = \frac{1}{2} \sum_l \frac{\mathbf{p}_l^2}{m_l} + V(\mathbf{x}_1, \mathbf{x}_2, \dots, \mathbf{x}_l) \quad (42)$$

where the total kinetic energy is the sum of the individual kinetic energies of the atoms at position l , \mathbf{p}_l is the momentum and m_l is the mass of each atom. The potential energy V is a function of the position vectors \mathbf{x}_l [52]. To interpret this system, the potential energy term is converted to be a function of the displacement between positions in a mono-atomic chain. If the lattice is defined by

$$\mathbf{l} = l\mathbf{a}, \quad (l = 1, 2, \dots, N), \quad (43)$$

where \mathbf{a} are atomic positions, then the coordinates \mathbf{x}_l are scalar and the potential

energy function may be rewritten as

$$V(\mathbf{x}_1, \mathbf{x}_2, \dots, \mathbf{x}_l) = \sum_l f(\mathbf{x}_{l+1} - \mathbf{x}_l) \quad (44)$$

and now $f(\mathbf{x}_{l+1} - \mathbf{x}_l)$ is purely a function of the displacement between atoms at l and $l + 1$.

In understanding the dynamics of the system, it is preferable to express the coordinates of the displacements from the lattice points as [52]

$$n_l = \mathbf{x}_l - l\mathbf{a}. \quad (45)$$

Equation (45) is the relationship where atoms occupy the lattice sites in the equilibrium state. Since there will be no difference at equilibrium, the derivative of potential energy with respect to position must be zero

$$\frac{\partial V}{\partial n_l} = 0, \quad (46)$$

if the displacements are equivalent at $n_1, n_2, \dots, n_N = 0$ [52]. If the potential energy function is expanded in a Taylor series along the displacements

$$V(\mathbf{x}_1, \mathbf{x}_2, \dots, \mathbf{x}_l) \approx V_0 + \frac{1}{2} \sum_{ll'} n_l n_{l'} \frac{\partial^2 V}{\partial n_l \partial n_{l'}}, \quad (47)$$

the second term in Eq. (47) is the second derivative of the interatomic potential function f given by Eq. (44). This is equivalent to the force constant in Section 2.3.1. The potential energy function developed through the Taylor expansion in Eq. (47) is called the harmonic approximation; it considers only the harmonic terms of the potential energy function and is merely an approximation to the total contribution from both harmonic and anharmonic processes in phonon scattering [52, 53].

To obtain the true state of a system which has multiple transport processes, the assumption that phonons and electrons behave independently of one another

must be abandoned. In doing so the anharmonic terms in the Hamiltonian may no longer be neglected. Assuming contributions from only the harmonic terms implies a perfect crystal system, which does not exist in reality. In a real system, phonons will interact with other phonons and electrons, and these interactions are perturbations of the Hamiltonian [52].

The anharmonic contribution of interest is the cubic term in the Taylor expansion, which describes three-phonon processes. This term can be added into the total Hamiltonian of the system through

$$\mathcal{H}_{pp} = \frac{1}{3!} \sum_{\mathbf{l}, \mathbf{b}; \mathbf{l}', \mathbf{b}'; \mathbf{l}'', \mathbf{b}''} \mathbf{n}_{\mathbf{l}, \mathbf{b}} \mathbf{n}_{\mathbf{l}', \mathbf{b}'} \mathbf{n}_{\mathbf{l}'', \mathbf{b}''} : \mathbf{A}_{\mathbf{l}, \mathbf{b}; \mathbf{l}', \mathbf{b}'; \mathbf{l}'', \mathbf{b}''}, \quad (48)$$

where $\mathbf{A}_{\mathbf{l}, \mathbf{b}; \mathbf{l}', \mathbf{b}'; \mathbf{l}'', \mathbf{b}''}$ is a third rank tensor in Cartesian coordinates. The Taylor expansion representation of this tensor is

$$\mathbf{A}_{\mathbf{l}, \mathbf{b}; \mathbf{l}', \mathbf{b}'; \mathbf{l}'', \mathbf{b}''} = \left. \frac{\partial^3 V}{\partial \mathbf{n}_{\mathbf{l}, \mathbf{b}} \partial \mathbf{n}_{\mathbf{l}', \mathbf{b}'} \partial \mathbf{n}_{\mathbf{l}'', \mathbf{b}''}} \right|_0 \quad (49)$$

which would be the next term in the Taylor expansion seen in Eq. (47) [52].

The third term in the Taylor series expansion describes the anharmonic lattice forces and incorporates phonon-phonon interaction processes. Consider one term of the summation in Eq. (49), $a_{-\mathbf{k}, p} a_{-\mathbf{k}', p'} a_{\mathbf{k}'', p''}^*$ which describes a process in which the phonons in the modes $(-\mathbf{k}, p)$ and $(-\mathbf{k}', p')$ are both eliminated and a phonon in mode (\mathbf{k}'', p'') is created (p denotes the polarization branch).

A three-phonon process is represented by

$$\mathbf{k} + \mathbf{k}' + \mathbf{k}'' = \mathbf{g} \quad (50)$$

and can be rearranged to show the sum of the wave vectors of the destroyed phonons $(\mathbf{k}, \mathbf{k}')$,

$$(-\mathbf{k}) + (-\mathbf{k}') = \mathbf{k}'' + \mathbf{g}. \quad (51)$$

If $\mathbf{g} = 0$, it is simple to follow Eq. (51), in which the wave vector of the created phonon must equal the sum of the wave vectors of the destroyed phonon. When this is the case, the process of state change is called a *Normal* process. It becomes difficult to explain the case where $\mathbf{g} \neq 0$, as intuition would suggest the phonon momentum is not being conserved. However, in crystal lattice vibrations no transfer of momentum can take place. Ziman explains this by calculating the expectation value of each phonon state [52]

$$\mathcal{B}_0 = \sum_{\mathbf{b},\mathbf{l}} \mathbf{p}_{\mathbf{b},\mathbf{l}}. \quad (52)$$

In Eq. (52), each phonon state has an expectation value of zero. The case in which $\mathbf{g} \neq 0$ in the phonon wave vector is called an *Umklapp* (“flop-over”) process. Umklapp processes interrupt heat transport as phonons are scattered back into the Brillouin zone, opposite in direction to the primary stream of phonons.

An example from Ziman [52] describes the effects of these anharmonic terms: A wave vector \mathbf{k} moves through a solid. As the wave passes, the lattice vibrates and some atoms come together closer than their equilibrium distance, and some move further apart. Another wave vector \mathbf{k}' moving through the medium will see the elastic properties of the lattice perturbed by the effects of the first wave. Wave vector \mathbf{k}' sees a change in the lattice elasticity due to the anharmonicity in the interatomic forces. The original phonon (wave vector \mathbf{k}) generates a periodic variation, and the phonon \mathbf{k}' is reflected from this, as though through a diffraction grating [52]. The coalescence of the two leads to a reflected phonon with a new wave vector, which is a Normal process

$$\mathbf{k}'' = \mathbf{k} + \mathbf{k}'. \quad (53)$$

In Umklapp processes, $\mathbf{g} + \mathbf{k}''$ is substituted into the left hand side of Eq. (53).

Section 2.3.1 discussed the properties of wave vectors in the first Brillouin zone, and that no wave vector may travel outside the boundaries of the first Brillouin zone. Because the same lattice displacement may be represented by either short or long wavelengths (as in Eq. (38)) only a single value of \mathbf{g} exists to allow \mathbf{k}'' to remain in the first Brillouin zone. The interference condition \mathbf{g} reflects dissipation processes in which phonons lose momentum and scatter diffusively [11, 52, 53].

Anharmonic effects are often observed in real materials. An excellent example from Gofryk et al. [8] demonstrates anharmonic scattering of an oxygen ion along its path in the cubic fluorite UO_2 lattice. Figure 3 shows the trajectory of the ion along the c-axis of a uranium dioxide simulation cell in an EMD simulation with no applied thermal gradient. The [100] and [001] axes represent the basal plane. Uranium dioxide possesses cubic symmetry and the white sphere in Fig. 3 [8] is consistent with harmonic (isotropic) scattering, which is expected. The red ellipsoid shows the actual trajectory distribution due to anharmonic scattering [8]. This case is further discussed in Section 4.5.

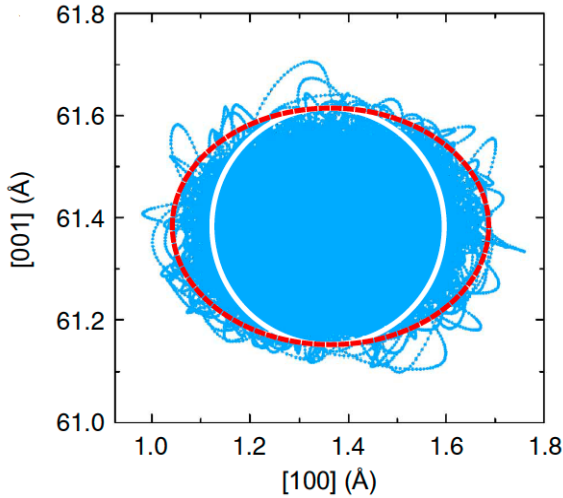


Figure 3: Trajectory of oxygen ion in UO_2

2.4.3 Lattice Imperfections

Physical defects in the atomic lattice are of primary importance in the study of scattering. No material exists which is completely free of defects. Some of the most common material defects are point imperfections, such as vacancies, interstitials and isotopes. Isotopic presence is the defect of interest in this research. Molecular dynamics simulations are able to capture behaviors of atoms through the use of interatomic potentials. Among such potentials of interest are the Basak and Geng potentials [9] for modeling interactions in UO_2 and xenon. These potentials are based on first-principles derivations, but also possess aspects determined by experiment. Previously, cross sections of the point defect were considered and a fourth power dependence on the wave vector was assumed [52]. This approach still has some merit, although the interatomic potential method, while not perfect, is able to capture effects which mimic those obtained experimentally.

Dislocations are discontinuities in the atomic lattice having some unrestricted motion under the influence of mechanical stresses. Dislocation energy is the potential energy of strain, which is spread out through the crystal. Locally, dislocations affect the energy of a phonon wave vector by changing the sound velocity, which is related to the strain field produced by the dislocation. The scattering probability is dependent on material properties and is related to the Grüneisen law of thermal expansion with a T^4 dependence [52], which is an anharmonic mechanism affecting Normal and Umklapp phonon-phonon processes (Section 2.4.2). In general, the strain field has a scattering power inversely proportional to the phonon wavelength λ .

Stacking faults and twin boundaries are two dimensional surface discontinuities in the crystal lattice. Literature suggests these surface defects produce strain fields which affect the scattering of the phonon wave vector [11, 52, 53]. It is assumed the perfect lattice for the $\langle 111 \rangle$ plane in a face-centered cubic crystal structure stacks atoms of type A, B, C in a repeating pattern, $ABCABCABC$. An example of stack fault is an error in this lattice, such as $ABCABABC$, where a line of C atoms have been left out. This discontinuity causes a mismatch in the periodicity of a plane wave, shown by Fig. 4 [52]. This can be handled by calculating coefficients to correct the wave displacements. However, this approach is limited in scope and can be modeled only in simple materials [52].

The principal mechanism affecting scattering behavior is the difference in orientation of the crystal structure of both grains at either side of the boundary. These are grain boundaries. If a phonon is traveling in a straight line, it may encounter a grain boundary and be redirected elsewhere, based on the incident angle of contact. If the angle is very low, the phonon may be totally reflected. This is due

to material anisotropy. Generally, the reflection coefficient is proportional to $\frac{\Delta v_g}{v_g^2}$ where Δv_g is the change in phonon velocity at the surface, and is also dependent on the polarization of the wave [52].

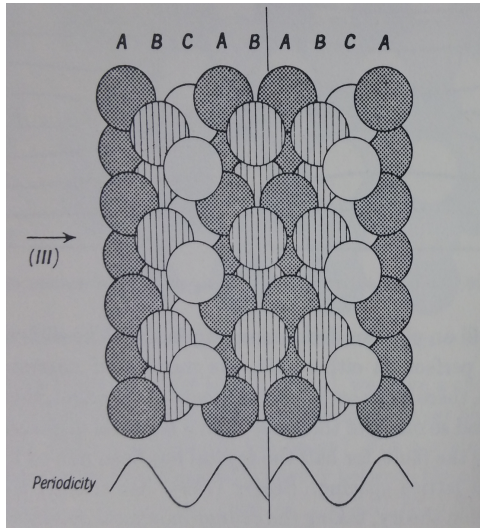


Figure 4: Stacking fault looking in $\langle 110 \rangle$ direction

Figure 5 shows phonon reflection at a grain boundary and emphasizes dependence on the angle of incidence. On the right side of Fig. 5 [52] is the grain mismatch at the boundary, where anharmonicity is strong. When phonon wavelength is long, the boundary can be modeled as a zero-thickness artifact. If the phonon wavelength is short, the boundary is treated as a surface of thickness D , and the coefficient of reflection will likely be proportional to $(\frac{D}{\lambda})^2$ if $\lambda \gg D$ [52,53]. Phonon transport is highly disrupted at grain boundaries, and molecular dynamics techniques are able to capture effects at these imperfections.

Phonon scattering by lattice imperfections has a marked effect on the thermal transport in materials. Some of the limitations in using deterministic methods have been clearly identified - as there are no specific lattice scattering kernels built

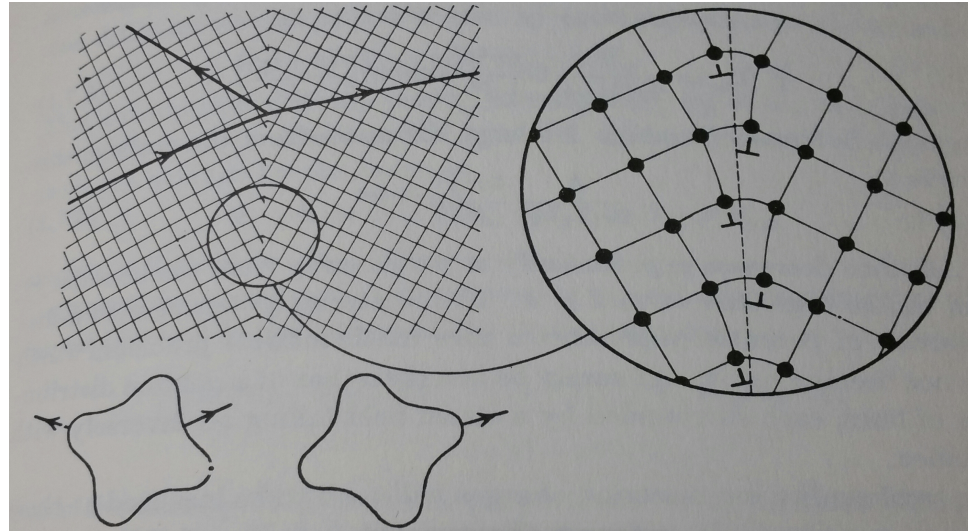


Figure 5: Grain boundary showing velocity mismatch and dislocation array

in to Rattlesnake. The only transport effects Rattlesnake can currently capture are the size effects due to the decreased length scales of transport simulations. This limitation is further discussed in Chapter 5.

2.5 Summary

In this chapter, the Boltzmann transport equation for phonons was introduced and the equation was reduced to the form used in this research. The SAAF form of the EPRT was derived. Phonon transport processes were discussed with an emphasis on their contributions to the mean free path. Phonon scattering physics were introduced, three of the primary processes were outlined and the limitations of a frequency independent method in a gray medium were discussed. The difficulties in capturing some of the more complicated processes were discussed with potential solutions outlined for future work.

3 METHODS

3.1 Introduction

In this chapter, we introduce the Self-Adjoint Angular Flux (SAAF) method, which is a second order formulation of the Boltzmann transport equation. The Boltzmann equation for phonons is then derived in SAAF form through a relatively simple algebraic process. This equation is reduced to a single dimension and spatially discretized using finite differences. The discrete-ordinates (S_N) angular discretization is applied to the resulting set of equations. Boundary conditions for phonon transport are implemented and results from the 1D, monoenergetic test code are shown. Rattlesnake, a neutron transport code is used to perform phonon transport simulations. MOOSE and Rattlesnake are further discussed and techniques are introduced to allow phonon transport to be simulated in Rattlesnake.

3.2 Discretization of the Equations

The SAAF form of the EPRT is reduced to a function of one spatial dimension x , and μ , the cosine of the angle between the phonon direction (Ω) and the x -axis. Equation (19) can be reduced to an equation for simulating phonon transport in a slab geometry

$$I(x, \mu) - \Lambda^2 \mu^2 \frac{\partial^2 I}{\partial x^2}(x, \mu) = I^0(x) - \Lambda \mu \frac{\partial I^0}{\partial x}(x). \quad (54)$$

3.2.1 Angular Discretization

The discrete ordinates method [41–43] is used to discretize the angular variable μ . The phonon transport equation becomes a set of N equations for the angular

phonon intensity in each discrete angle μ_m ,

$$I(x, \mu_m) = I_m(x). \quad (55)$$

Gauss-Legendre quadrature is chosen to numerically integrate the angular phonon intensity over angle:

$$I(x) = \int_{-1}^1 I(x, \mu) d\mu \approx \sum_{m=1}^N w_m I_m(x) \quad (56)$$

where $I(x)$ is the scalar phonon intensity (the zeroth angular moment), and heat flux q is the first angular moment

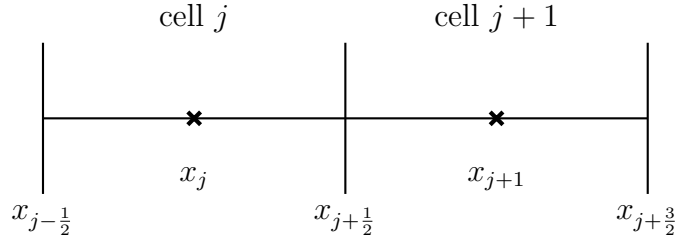
$$q(x) = \int_{-1}^1 I(x, \mu) \mu d\mu \approx \sum_{m=1}^N w_m \mu_m I_m(x). \quad (57)$$

The weights in the quadrature set have been normalized such that

$$\sum_{m=1}^N w_m = 2. \quad (58)$$

3.2.2 Spatial Discretization - Slab Geometry

We begin this process by collapsing Eq. (7) into slab geometry form. Figure 6



$$[\Lambda_j, \Delta x_j, I_{m,j}, I_j^0]$$

Figure 6: Spatial mesh and relevant quantities

shows cell configuration in the slab geometry. Equation (59) is for angular phonon

intensity at the cell center j and direction m - a balance equation for the first order form of the transport equation over an interval $[x_{j-\frac{1}{2}}, x_{j+\frac{1}{2}}]$:

$$\Lambda_j \mu_m \left(I_{m,j+\frac{1}{2}} - I_{m,j-\frac{1}{2}} \right) + I_{m,j} \Delta x_j = I_j^0 \Delta x_j. \quad (59)$$

Where

$$\Delta x_j = \Delta x_{j+\frac{1}{2}} - \Delta x_{j-\frac{1}{2}}. \quad (60)$$

The equation for the dual cell is defined for the edge quantities at $j + \frac{1}{2}$, which is a balance equation for the first order form of the transport equation over an interval $[x_j, x_{j+1}]$:

$$\Lambda_{j+\frac{1}{2}} \mu_m (I_{m,j+1} - I_{m,j}) + I_{m,j+\frac{1}{2}} \Delta x_{j+\frac{1}{2}} = I_{j+\frac{1}{2}}^0 \Delta x_{j+\frac{1}{2}}, \quad (61)$$

where

$$\Lambda_{j+\frac{1}{2}} = \frac{\Lambda_j \Delta x_j + \Lambda_{j+1} \Delta x_{j+1}}{\Delta x_{j+1} + \Delta x_j}, \quad (62)$$

$$\Delta x_{j+\frac{1}{2}} = \frac{1}{2} (\Delta x_{j+1} + \Delta x_j). \quad (63)$$

Equations (59) and (61) may now be used to arrive at an interior mesh discretization scheme for the EPRT in the SAAF derivation. Solving Eq. (59) for $I_{m,j}$ yields

$$I_{m,j} = I_j^0 - \frac{\Lambda_j \mu_m}{\Delta x_j} \left(I_{m,j+\frac{1}{2}} - I_{m,j-\frac{1}{2}} \right). \quad (64)$$

This result is inserted into Eq. (61) to replace the cell-centered quantities:

$$\begin{aligned} & - \frac{\Lambda_{j+\frac{1}{2}} \Lambda_{j+1} \mu_m^2}{\Delta x_{j+1}} \left(I_{m,j+\frac{3}{2}} - I_{m,j+\frac{1}{2}} \right) + \frac{\Lambda_{j+\frac{1}{2}} \Lambda_j \mu_m^2}{\Delta x_j} \left(I_{m,j+\frac{1}{2}} - I_{m,j-\frac{1}{2}} \right) \\ & + \Delta x_{j+\frac{1}{2}} I_{m,j+\frac{1}{2}} = \Delta x_{j+\frac{1}{2}} I_{j+\frac{1}{2}}^0 + \Lambda_{j+\frac{1}{2}} \mu_m [I_j^0 - I_{j+1}^0]. \end{aligned} \quad (65)$$

If the terms corresponding to cell indices are grouped, the result is a tridiagonal matrix,

$$\begin{aligned} & - \left[\frac{\Lambda_{j+\frac{1}{2}} \Lambda_j \mu_m^2}{\Delta x_j} \right] I_{m,j-\frac{1}{2}} + \left[\frac{\Lambda_{j+\frac{1}{2}} \Lambda_j \mu_m^2}{\Delta x_j} + \frac{\Lambda_{j+\frac{1}{2}} \Lambda_{j+1} \mu_m^2}{\Delta x_{j+1}} + \Delta x_{j+\frac{1}{2}} \right] I_{m,j+\frac{1}{2}} \\ & - \left[\frac{\Lambda_{j+\frac{1}{2}} \Lambda_{j+1} \mu_m^2}{\Delta x_{j+1}} \right] I_{m,j+\frac{3}{2}} = \Delta x_{j+\frac{1}{2}} I_{j+\frac{1}{2}}^0 + \Lambda_{j+\frac{1}{2}} \mu_m [I_j^0 - I_{j+1}^0]. \end{aligned} \quad (66)$$

Equation (66) is applicable for all interior cell edges.

3.2.3 Boundary Conditions

To define the angular phonon intensity at the left side boundary $I_{m,\frac{1}{2}}$, Eq. (59) is solved over the interval $[x_{\frac{1}{2}}, x_1]$

$$\Lambda_1 \mu_m (I_{m,1} - I_{m,L}) + I_{m,\frac{1}{2}} \frac{\Delta x_1}{2} = I_{\frac{1}{2}}^0 \frac{\Delta x_1}{2}. \quad (67)$$

Using Eq. (64) to eliminate the cell centered quantity in Eq. (67) gives

$$\Lambda_1 \mu_m \left(\left[I_1^0 - \frac{\Lambda_1 \mu_m}{\Delta x_1} (I_{m,\frac{3}{2}} - I_{m,\frac{1}{2}}) \right] - I_{m,L} \right) + I_{m,\frac{1}{2}} \frac{\Delta x_1}{2} = I_{\frac{1}{2}}^0 \frac{\Delta x_1}{2}, \quad (68)$$

and isolating the angular phonon intensities results in a prescription for the left boundary condition

$$\left[\frac{\Lambda_1^2 \mu_m^2}{\Delta x_1} + \frac{\Delta x_1}{2} \right] - \left[\frac{\Lambda_1^2 \mu_m^2}{\Delta x_1} \right] I_{m,\frac{3}{2}} = \frac{\Delta x_1}{2} I_{\frac{1}{2}}^0 + \Lambda_1 \mu_m [I_{m,L} - I_1^0]. \quad (69)$$

A similar approach is applied for the right boundary with the interval shifted to $[x_N, x_{N+\frac{1}{2}}]$,

$$\Lambda_N \mu_m (I_{m,R} - I_{m,N}) + I_{m,N+\frac{1}{2}} \frac{\Delta x_N}{2} = I_{N+\frac{1}{2}}^0 \frac{\Delta x_N}{2}. \quad (70)$$

and again use Eq. (64) to eliminate the cell centered quantity in Eq. (70)

$$\begin{aligned} \Lambda_N \mu_m \left(I_{m,R} - \left[I_N^0 - \frac{\Lambda_N \mu_m}{\Delta x_N} \left(I_{m,N+\frac{1}{2}} - I_{m,N-\frac{1}{2}} \right) \right] \right) \\ + I_{m,N+\frac{1}{2}} \frac{\Delta x_N}{2} = I_{N+\frac{1}{2}}^0 \frac{\Delta x_N}{2}. \end{aligned} \quad (71)$$

Grouping terms results in at equation for the right boundary condition

$$\begin{aligned} \left[\frac{\Lambda_N^2 \mu_m^2}{x_N} \right] I_{m,N-\frac{1}{2}} - \left[\frac{\Lambda_N^2 \mu_m^2}{x_N} - \frac{\Delta x_N}{2} \right] I_{m,N+\frac{1}{2}} = \\ I_{N+\frac{1}{2}}^0 \frac{\Delta x_N}{2} + \Lambda_N \mu_m [I_N^0 - I_{m,R}]. \end{aligned} \quad (72)$$

Boundary conditions are implemented by specifying $I_{m,L}$ and $I_{m,R}$ for incident angles in the quadrature set. The values the angular intensities take on the boundaries is directionally dependent,

$$I_{m,L} \begin{cases} f_m, & \mu_m > 0 \\ I_{m,\frac{1}{2}}, & \mu_m < 0 \end{cases}, \quad (73)$$

$$I_{m,R} \begin{cases} f_m, & \mu_m < 0 \\ I_{m,N+\frac{1}{2}}, & \mu_m > 0 \end{cases}, \quad (74)$$

where $f_m = 0$ for a vacuum boundary and $f_m = I_{\frac{1}{2}}(-\mu_m)$ or $f_m = I_{N+\frac{1}{2}}(-\mu_m)$ for a reflecting boundary. Typically, phonon emission sources are placed on the boundaries to simulate a temperature gradient, these were discussed in Section 2.

3.2.4 Slab Geometry Code Development

A one-dimensional slab geometry S_N phonon transport code in the SAAF formulation was developed and tested in Matlab [54], based on the work of Morel and McGhee [43]. The code was modified with the discretized equations of phonon

transport. The code was compared against the work of Yilbas and Bin Mansoor, who ran phonon transport simulations using a 1D forward and backward finite transport scheme with a finite difference discretization [26]. They modeled a homogeneous thin film of silicon - this type of test problem is very common in phonon transport and has been simulated in other work [23–26].

We simulated a 1 K temperature gradient, with boundary temperatures of 300 K and 301 K, applied to a thin film three mean free paths in thickness, $L = 101.4 \cdot 10^{-9}$ m. The mean free path for silicon at 300 K is $\Lambda = 33.8 \cdot 10^{-9}$ m, $C_v = 1.653 \cdot 10^6$ J · m⁻³ · K⁻¹, $v_g = 8430$ m · s⁻¹. Figure 7 shows the non-dimensional temperature and the results of Yilbas and Bin Mansoor for the same problem.

Figure 8 shows the first moment of the angular phonon intensity. Here we see the steady state assumption of zero heat flux properly applied as the shape of the solution of sinusoidal and the area under the curves is zero.

The shape of the numerical solution to the thin film problem in Fig. 7 using the 1D transport code agrees well with the solution of Yilbas and Bin Mansoor. These results lay the groundwork for testing phonon transport using a more robust, generalized geometry neutron transport code. Rattlesnake [48] is a neutron transport code in the Self-Adjoint Angular Flux form and is introduced and discussed in the next section.

3.3 Rattlesnake: A Radiation S_N Transport Code

Rattlesnake is a radiation transport code in the MOOSE framework which was developed at INL. It solves the Boltzmann transport equation for neutrons in the Self-Adjoint Angular Flux formulation. MOOSE is a finite-element multiphysics architecture built for solving coupled nonlinear partial differential equations. In

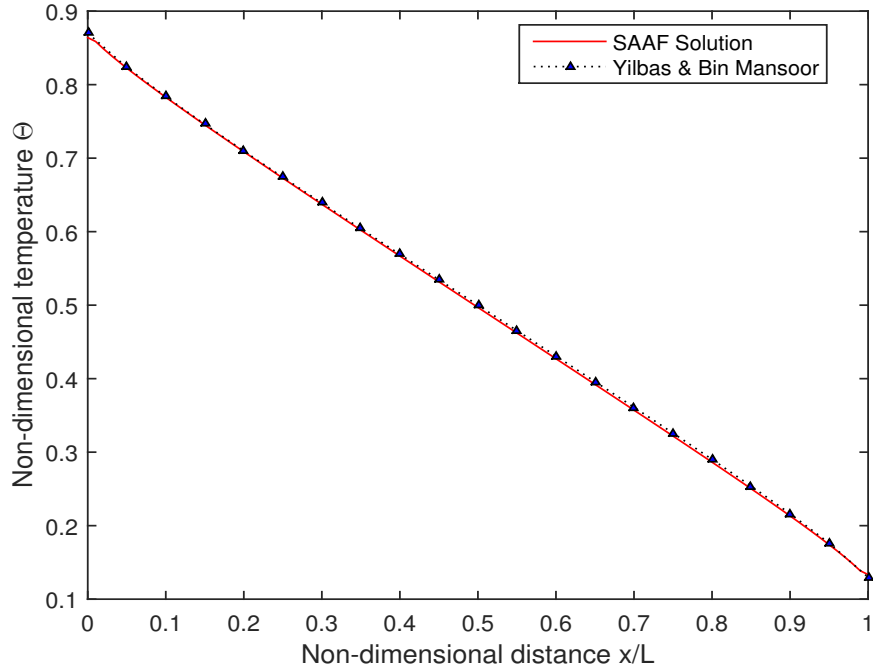


Figure 7: Non-dimensional temperatures, Rattlesnake and Yilbas and Bin Mansoor

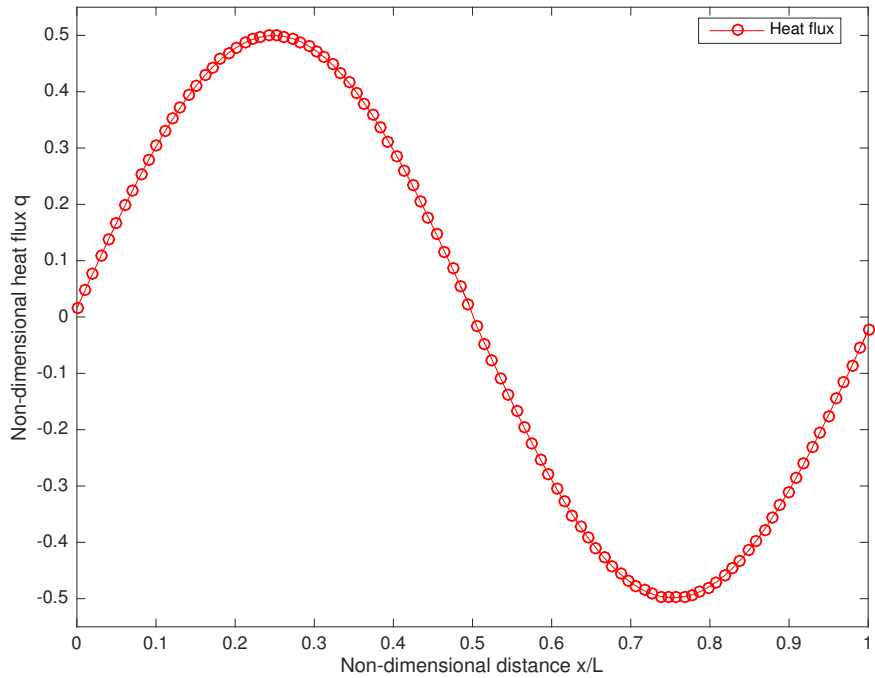


Figure 8: Non-dimensional heat flux

addition to Rattlesnake there are a number of other modules which solve equations for specific physics applications, e.g., thermal hydraulics, probabilistic risk assessment and meso-scale phase fields.

MOOSE is written in the C++ language and is a fully-coupled and fully-implicit solver. All the user code is dimension agnostic, and employs unstructured meshes. MOOSE is fully parallelizable and is meshed with the `libMesh` [55] finite-element C++ library. Meshes can be generated in the MOOSE environment (static and adaptive) or read in from a file (static). The solver library in MOOSE is the Portable, Extensible Toolkit for Scientific Computation (PETSc) [56] suite. Among these are `boomerAMG` and `hypre`, which are used extensively in this research. These use preconditioned Jacobian-Free Newton-Krylov methods to rapidly solve transport problems.

To show how MOOSE interprets equations into the coding environment, it is best to look at the strong and weak forms of an equation. The terms of Eq. 75 (the heat equation) are rearranged to obtain zero on the right hand side, the entire equation is multiplied by a test function (ψ) and integrated over the angular domain (Ω). Integration by parts is used in conjunction with the divergence theorem to obtain functions which can be read into MOOSE (Eq. 76),

$$\rho C_p \frac{\partial T}{\partial t} - \nabla \cdot k(T, B) \nabla T = f, \quad (75)$$

$$\int_{\Omega} \rho C_p \frac{\partial T}{\partial t} \psi_i + \int_{\Omega} k \nabla T \cdot \nabla \psi_i - \int_{\Omega} k \nabla T \cdot \mathbf{n} \psi_i - \int_{\Omega} f \psi_i = 0. \quad (76)$$

Each of the terms in Eq. (76) are read into MOOSE as ‘kernels’ which are solved at various quadrature points in the simulation through a weighted residual method (one of the solution archetypes in MOOSE). MOOSE uses ‘Executioners’ as solution drivers, which can be steady-state, transient, and adaptive transient. Temporal discretization is handled using the fully implicit Euler method.

In this research, all of the meshes were constructed in CUBIT [57], a geometry and mesh generation toolkit developed by Sandia National Laboratory. These meshes are exported in the Exodus format. All problems are solved with Preconditioned Jacobian-Free Newton Krylov (PJFNK) methods. The PETSc options are kept static, use `hypre` as the linear solver, `boomerAMG` as the parallel algebraic multigrid solver, and use the Krylov Space Method (KSP) of Generalized Minimal Residuals (GMRES). All problems modeled use the Steady executioner, with the exception of the simulation in Section 4.3. Table 1 provides tolerances, iteration limits and quadrature type used in all problems. All simulations were conducted on the Rogue cluster at Oregon State University, which has 2 6-core Intel Xeon Phi processors at 2.67 GHz each and 48 GB RAM.

MOOSE and Rattlesnake solution criteria				
l-max-its	nl-max-its	l-tol	nl-rel-tol	Quadrature
1000	100	10^{-6}	10^{-8}	Level-Symmetric

Table 1: Simulation convergence parameters

The Rattlesnake transport code has been identified as a good candidate to simulate phonon transport. To use Rattlesnake to effectively model phonon transport, certain measures must be taken with the construction of the code input to specify the proper conditions and physics of phonon transport. In the MOOSE input file, Rattlesnake parameters are added through the `RattlesnakeParams` block. Material properties are defined through either an XML file which is best used for multiband transport applications, or through the `Materials` block in the input file. Phonons can be binned into frequency groups, analogous to the way neutrons are partitioned into energy groups - however this research uses a gray approximation and frequency dependence is not assumed. Therefore, materials can be specified in

the `Materials` block by use of `ConstantNeutronicsMaterial`, which allows the user to input constant macroscopic cross sections. Rattlesnake can compute higher scattering moments which is set with the `NA` command. This parameter was set to `NA=1` for all simulations, which calculated the zeroth and first moments of angular phonon intensity.

The phonon mean free path Λ was defined in Chapter 2 and has units of length. Rattlesnake reads macroscopic cross section data which have units of inverse centimeters. To use mean free path in place of macroscopic cross section, Λ is simply inverted and passed to the input file. The conversion from meters to centimeters is unimportant as MOOSE is dimensionally agnostic, and proper conversions can be applied during postprocessing of the output data.

The relationship between angular phonon intensity, temperature and material properties was outlined in Chapter 2. An incident angular phonon intensity can be thought of as an analog to an incident neutron source. To place neutron sources in transport simulations, Rattlesnake uses the function `SurfaceSource`, which allows placement of a user-defined source on a geometric boundary. Boundary locations are defined in CUBIT and passed in to the Rattlesnake input file. The `SurfaceSource` function requires a vacuum boundary location, and replaces the vacuum with a source instead. Vacuum and source boundaries may be easily interchanged in the SAAF derived transport equation, as discussed in Section 3.2.3. To apply an incident source of phonons, the boundary locations are specified, and a vector with angular phonon intensity rates is declared through `SurfaceSource`. Reflecting conditions were applied to all boundaries not assigned as phonon sources.

3.4 Summary

This chapter introduced the Boltzmann transport equation derived in the Self-Adjoint Angular Flux form for a generalized geometry. The equation was reduced to a slab geometry form and discretized in angle and space. A neutron transport code was written and the SAAF method was tested on problems with known analytic solutions. As this method proved effective, the code was modified to simulate phonon transport. Yilbas and Bin Mansoor [26] simulated phonon transport through a thin film of silicon, a problem well-characterized in open literature. Their results were compared to the numerical solutions using the 1D slab geometry code modified for phonon transport. The two results were in good agreement, and motivated the extension of this research to use a more sophisticated, general neutron transport solver. Rattlesnake, in the MOOSE framework, was identified and discussed as the ideal candidate for this purpose. A brief overview of Rattlesnake is given.

4 RESULTS

4.1 Introduction

Rattlesnake was identified as a viable candidate to perform 3D, deterministic phonon transport simulations. The types of problems modeled steadily increased in complexity as Rattlesnake continued to generate positive simulation results. In most cases, problems with known solutions from MD, deterministic or experimental methods were chosen to validate Rattlesnake as a deterministic phonon transport driver. The results of these simulations are provided in this chapter. The principal physical system of interest in our research uranium dioxide with xenon cluster defects. An MD phonon transport study [9] is selected, system conditions are replicated and deterministic phonon transport results are compared with those of MD. This is presented in Section 4.6.

4.2 Phonon Transport in Thin Films

A test problem from Yilbas and Mansoor [25] was selected, a deterministic phonon transport simulation through a thin film of silicon. To simulate the test problem from [25] in Rattlesnake, a three dimensional mesh was constructed with CUBIT [57]. In keeping with the parameters used by Yilbas and Bin Mansoor, the lengths of the cube geometry were 101.4 nm on each side, equivalent to three phonon mean free paths. This quantity is the “acoustic thickness” of the material, and is analogous to the optical thickness characterized in neutron transport simulations. Material properties for the model problem are obtained from Majumdar [23] and Incropera [58].

Temperature boundary conditions were applied to the YZ planes using `SurfaceSource`, and reflecting boundary conditions were placed on the XY and XZ planes. Parameters used in the silicon thin film simulation are listed in Table 2. $I_{b,L}$ and $I_{b,R}$ are the phonon intensities at the left and right boundaries. The test problem was executed with an angular quadrature of S_8 , using a coarse and fine mesh. Both of these were constructed with a Python script written for CUBIT. Figure 9 is the mesh used in the simulations. Table 3 contains mesh and quadrature data.

Properties for silicon thin film	
Parameter	Value
$T_{b,L}$ [K]	301
$T_{b,R}$ [K]	300
v_g [$\text{m} \cdot \text{s}^{-1}$]	8430
C_v [$\text{J} \cdot \text{m}^{-3} \cdot \text{K}^{-1}$]	$1.653 \cdot 10^6$
$I_{b,L}$ [$\text{W} \cdot \text{m}^{-2}$]	$3.3378 \cdot 10^{11}$
$I_{b,R}$ [$\text{W} \cdot \text{m}^{-2}$]	$3.3267 \cdot 10^{11}$
Λ [m]	$33.8 \cdot 10^{-9}$

Table 2: Thin film simulation parameters

Thin film test data				
Case	Element Count	DOFs	Quad. Order	Time [s]
Coarse	1000	$1.1 \cdot 10^5$	S_8	8
Fine	12167	$1.17 \cdot 10^6$	S_8	57

Table 3: Thin film simulation statistics

A mesh and quadrature refinement study was performed on the test problem. This was accomplished by varying the number of available weights and ordinates in the angular discretization, as well as changing the element size of the mesh. Figure 11 shows the results of the variation in angular quadrature set. Figure 12 shows results of changing element size in the mesh.

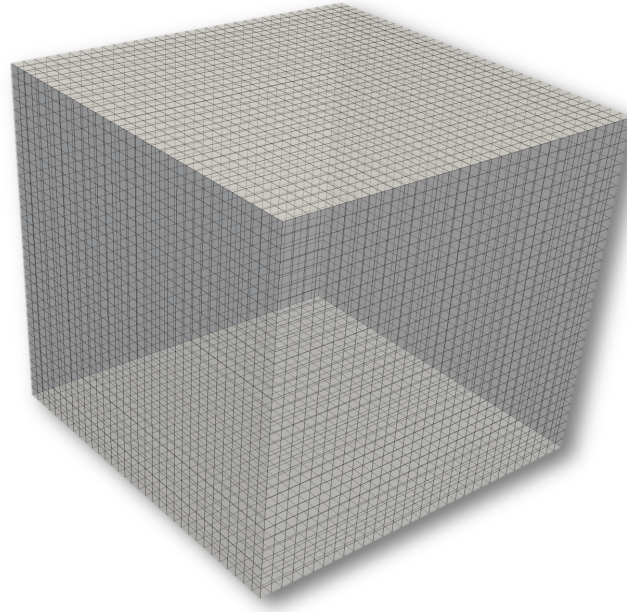


Figure 9: Mesh used in silicon thin film problem

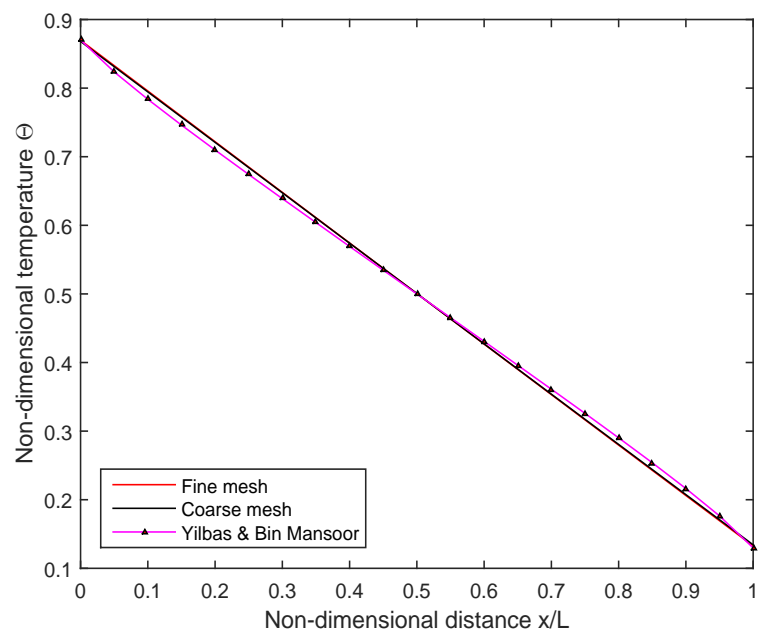


Figure 10: Solution comparison with Yilbas and Bin Mansoor

Quadrature study data				
Case	Element Count	DOFs	Quad. Order	Time [s]
1	1000	$2.3 \cdot 10^5$	S ₁₂	14
2	1000	$3.0 \cdot 10^5$	S ₁₄	20
3	1000	$3.8 \cdot 10^5$	S ₁₆	26
4	1000	$5.9 \cdot 10^5$	S ₂₀	40
5	1000	$8.3 \cdot 10^5$	S ₂₄	59

Table 4: Quadrature study statistics

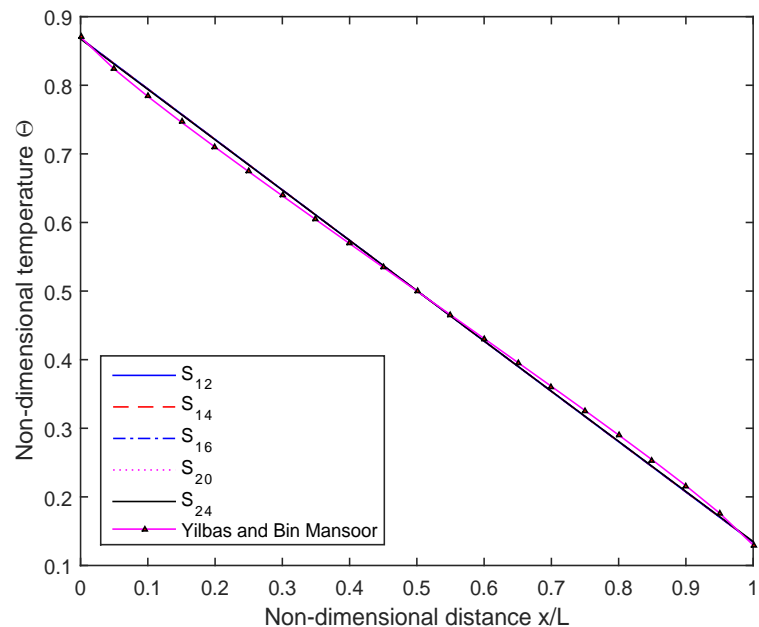


Figure 11: Dependencies on quadrature set variation

Mesh refinement study data				
Case	Element Count	DOFs	Quad. Order	Time [s]
1	1000	$1.1 \cdot 10^5$	S ₈	8
2	4096	$4.0 \cdot 10^5$	S ₈	21
3	12167	$1.1 \cdot 10^6$	S ₈	57
4	27000	$2.4 \cdot 10^6$	S ₈	121
5	35937	$3.2 \cdot 10^6$	S ₈	156

Table 5: Mesh study statistics

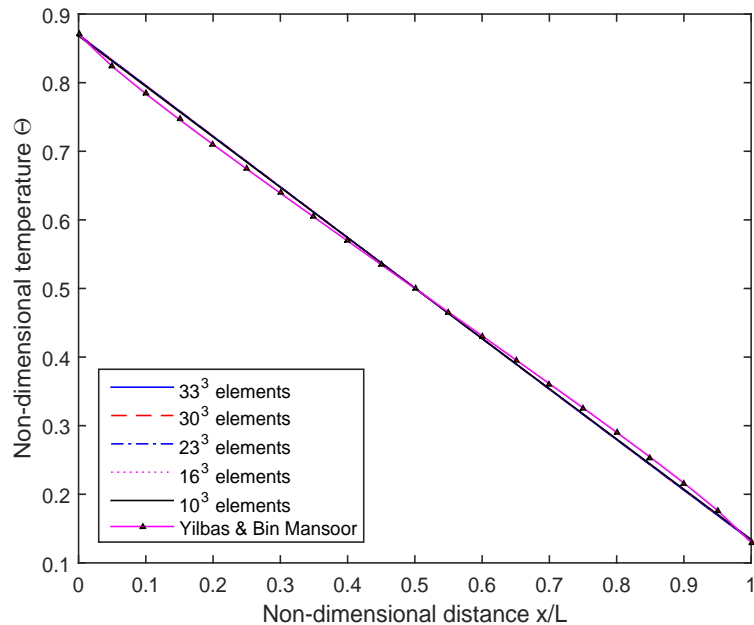


Figure 12: Solution dependence on element count variation

4.3 Two Material System

This test problem is based on the work of Ali and Yilbas [29], who performed deterministic transport simulations in an aluminum and silicon system in two dimensions. They divide the problem into four sub-domains, which was necessary

for the solution technique they used. A finite difference numerical scheme (forward Euler) was employed to discretize the spatial domain, and the discrete ordinates method was applied to the angular variable. Time discretization is implemented with an implicit Euler method. Figure 13 is the spatial grid used by Ali and Yilbas [29].

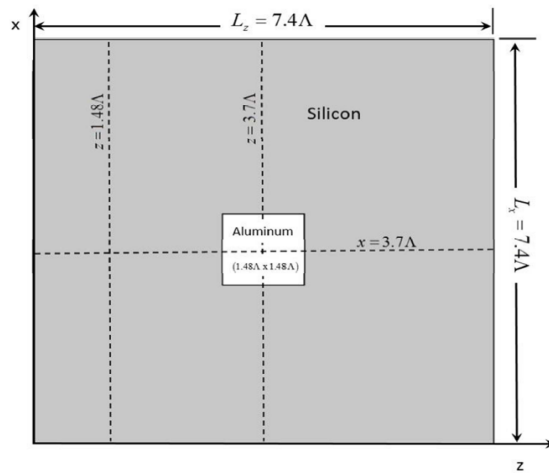


Figure 13: Two-dimensional spatial domain

Subdividing both the silicon and aluminum regions was likely employed to properly model the contributions from the wave vector and dispersion formulation, however no discussion of this is given. Temperature boundary conditions at the silicon edges were set to $T = 300$ K, and the aluminum region had a time-dependent, exponential function governing the temperature, $T_{q,dot} = (300 + \exp(\frac{-6.8}{t}))$. Due to the nature of the spatial discretization, either forward or backward difference schemes were used based on position. Figures 14 and 15 show temperature distribution of Ali and Yilbas at $t = 15$ ps and $t = 85$ ps [29].

To model this system with Rattlesnake, the temperature boundaries of the aluminum dot were fixed at $T = 301$ K. The temperature of the silicon boundaries

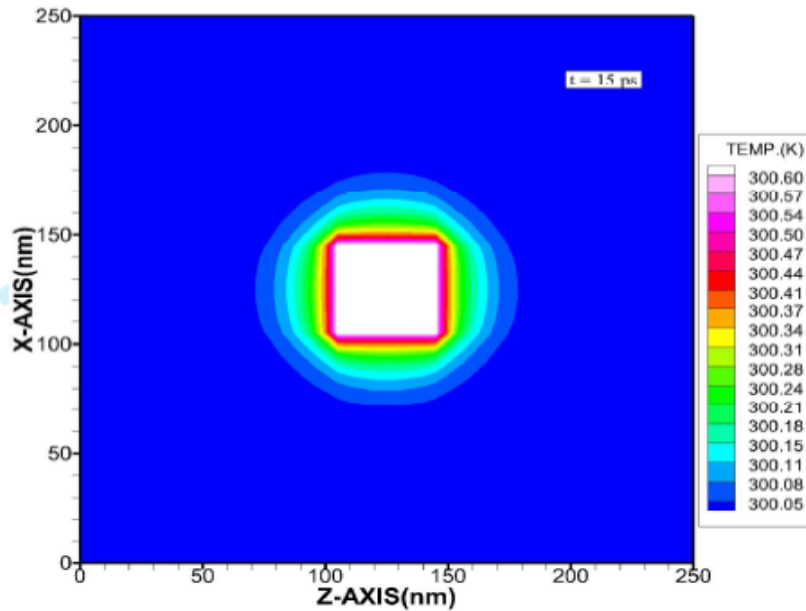


Figure 14: Temperature distribution at $t = 15$ ps

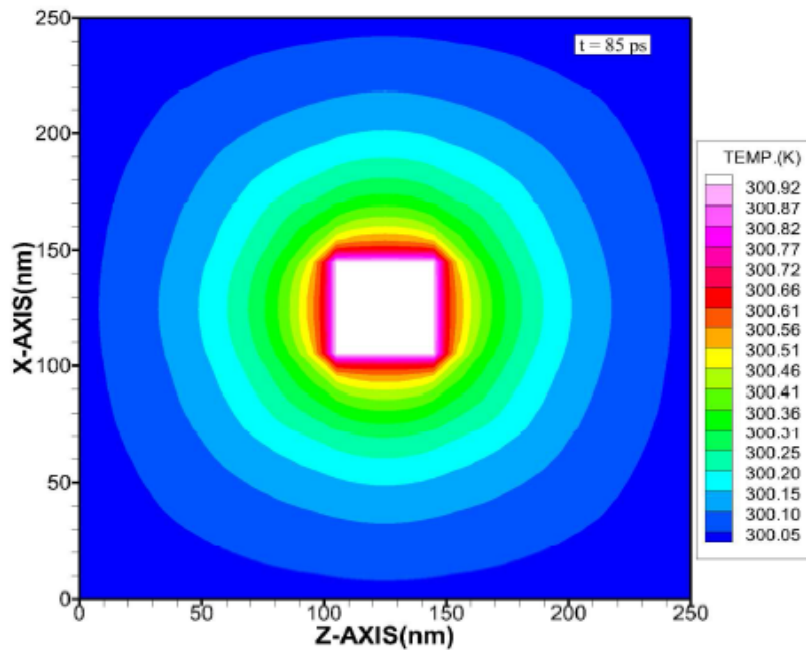


Figure 15: Temperature distribution at $t = 85$ ps

remained at $T = 300\text{ K}$. Silicon material properties remained the same, and material properties for aluminum were obtained from Incropera [58]. Parameters used in the silicon thin film simulation are listed in Table 6. The entire problem mesh is shown in Fig. 16 and the aluminum region is seen in Fig. 17. Mesh and quadrature information are contained in Table 7.

Properties for Al-Si system		
Parameter	Al	Si
T_b [K]	301	300
v_g [$\text{m} \cdot \text{s}^{-1}$]	6420	8430
C_v [$\text{J} \cdot \text{m}^{-3} \cdot \text{K}^{-1}$]	$2.944 \cdot 10^6$	$1.653 \cdot 10^6$
I_b [$\text{W} \cdot \text{m}^{-2}$]	$3.5165 \cdot 10^{11}$	$3.3267 \cdot 10^{11}$
Λ [m]	$2.9 \cdot 10^{-9}$	$33.8 \cdot 10^{-9}$

Table 6: Al-Si simulation parameters

Al-Si simulation data			
Element Count	DOFs	Quad. Order	Time [s]
11849	$1.7 \cdot 10^6$	S ₁₆	37

Table 7: Al-Si simulation statistics

The first moment of heat flux is shown in Figs. 20 and 21. Ali and Yilbas do not report this quantity and it has been included here for the sake of completeness. If the option is enabled, Rattlesnake will calculate the first moment of angular phonon intensity in all spatial directions.

A transient simulation of this system was performed. Time discretization is performed using the MOOSE framework involving an implicit Euler scheme. The simulation parameters (boundary conditions, quadrature set) were the same as in the steady-state problem, the duration was 500 ps with time steps of 1 ps. Figures 22 and 23 are conditions at 15 and 85 ps.

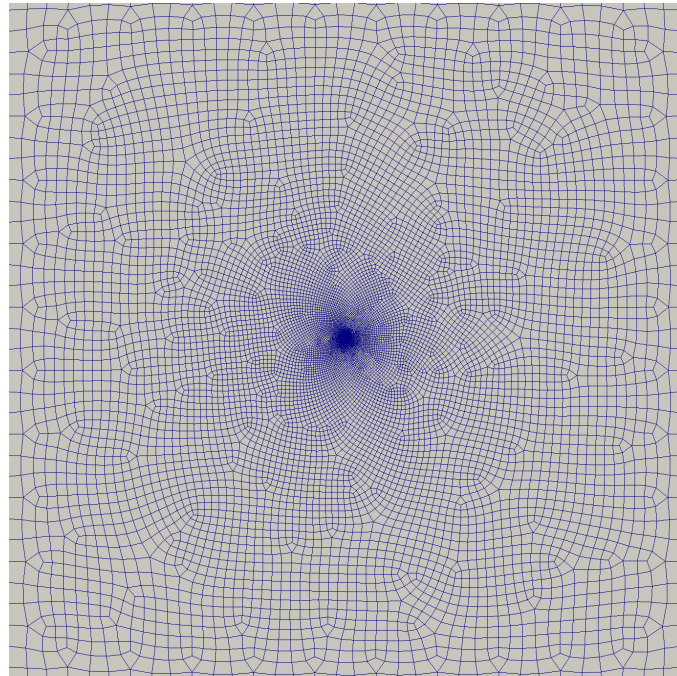


Figure 16: Mesh used in Al-Si system

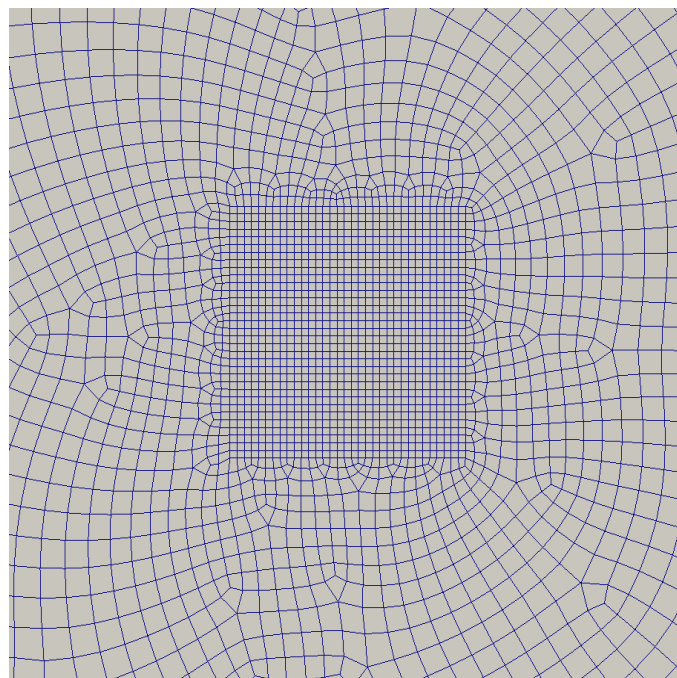


Figure 17: Aluminum region of mesh

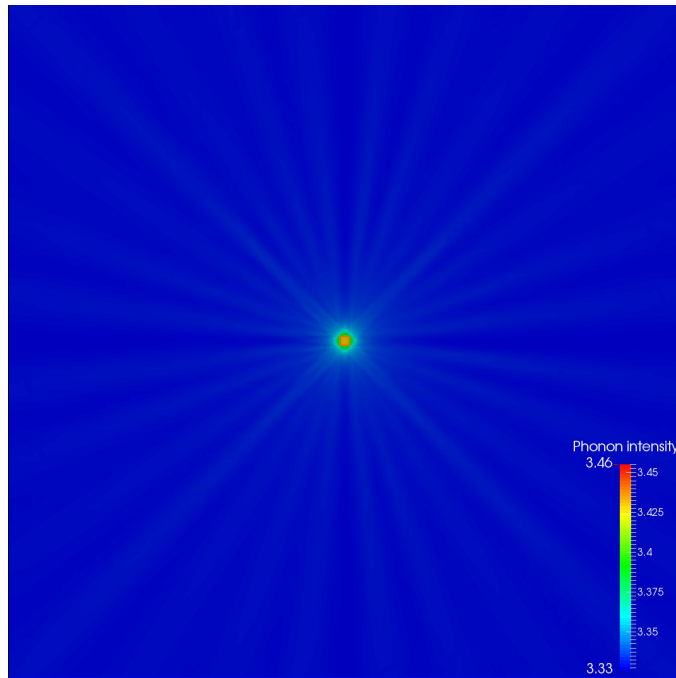


Figure 18: Phonon intensity, steady-state solution

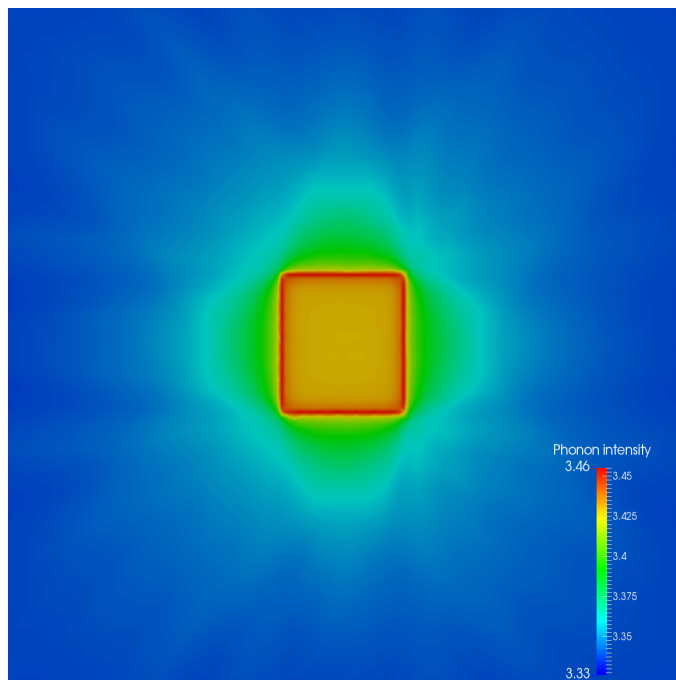


Figure 19: Phonon intensity near aluminum dot, steady-state solution

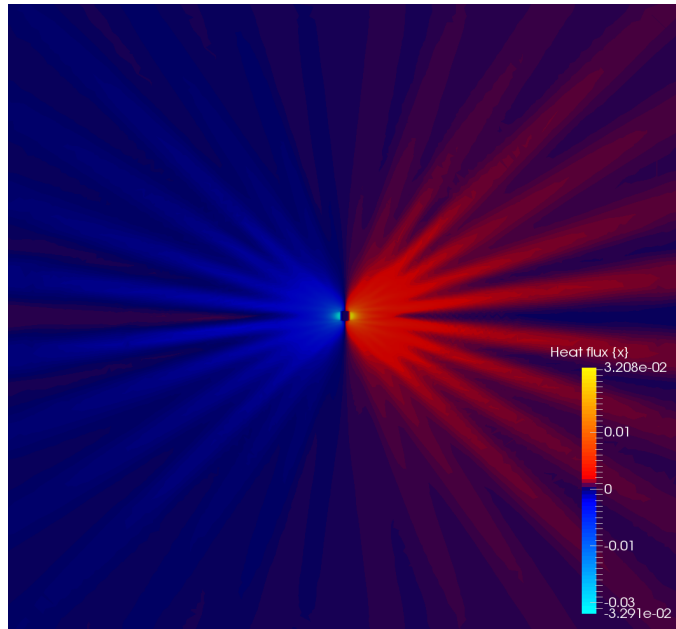


Figure 20: Heat flux, x -direction

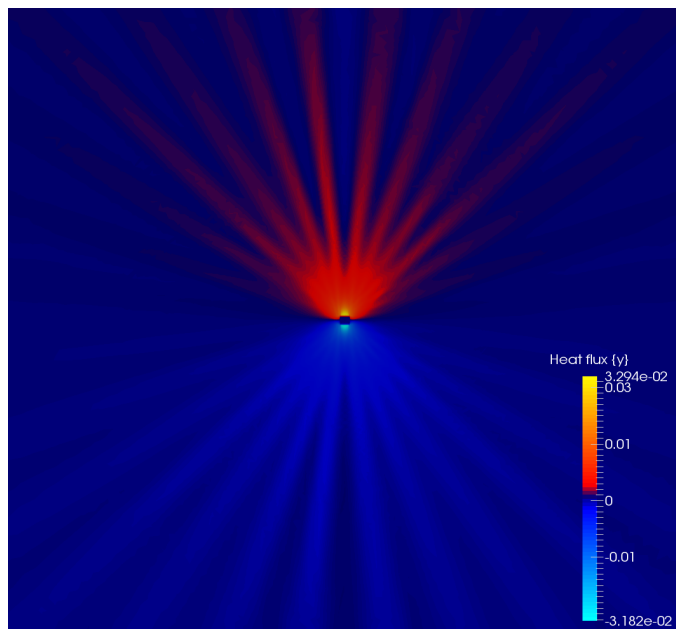


Figure 21: Heat flux, y -direction

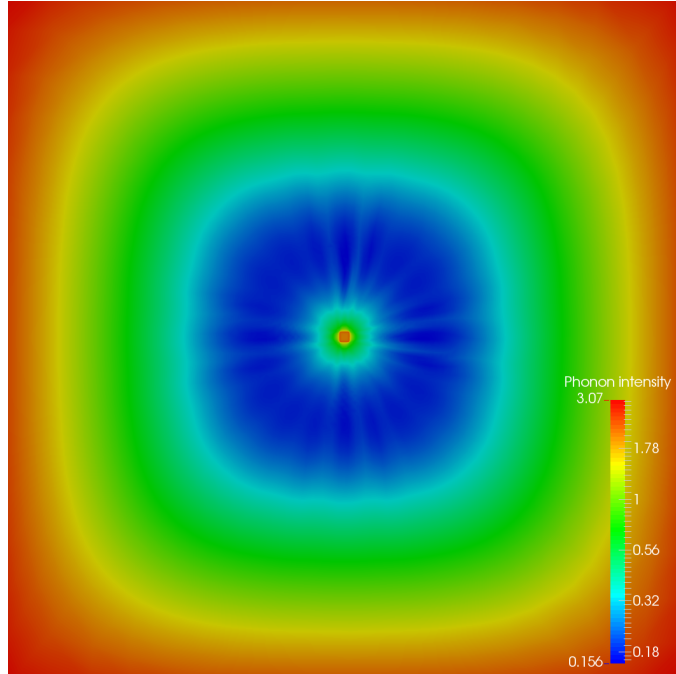


Figure 22: Rattlesnake solution at $t = 15$ ps.

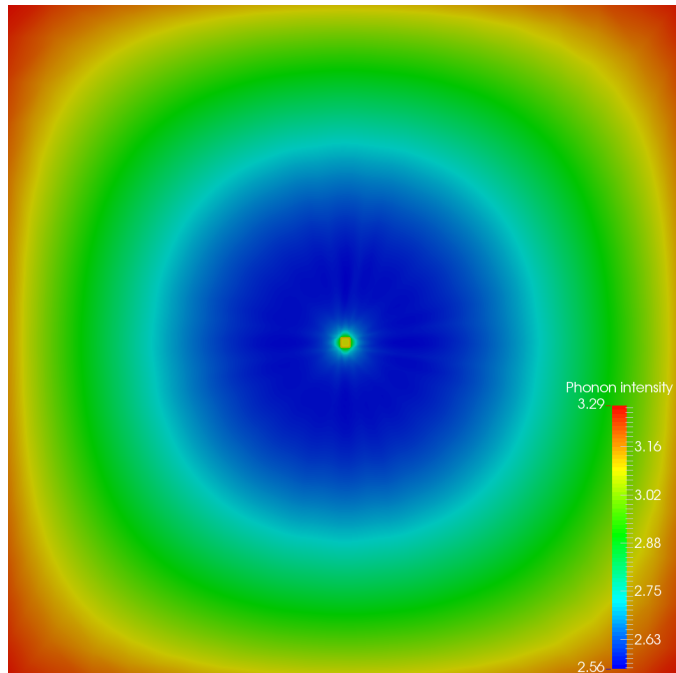


Figure 23: Rattlesnake solution at $t = 85$ ps.

4.4 Phonon Transport in z -axis Graphite

This test case was performed as a collaborative effort with MD researchers. Rattlesnake was used to conduct phonon transport simulations in graphite to measure thermal resistance. Rattlesnake results are compared to MD. The dominant mechanism which contributed to an increase in thermal resistance along the z -axis were the multiple types of interstitial cluster defects. The simulations performed with Rattlesnake modeled two cases: defect-free graphite, graphite with interstitial defect clusters.

To allow for the calculation of equilibrium thermal conductivity, a graphite superlattice was constructed. This geometry is a collection 8 of the simulation cells used in Oliveira [6]. Each cell had dimensions (x, y, z) of 2.705 nm x 4.686 nm x 7.379 nm and consisted of 22 layers of graphite, with the simulated defect placed in between the 11th and 12th layer. The superlattice sandwiched and stacked 8 cells together, giving overall dimensions of 5.41 nm x 9.37 nm x 14.8 nm which gives a total of 8 interstitial defects. The superlattice geometry is approximately 10 mean free paths thick along the z -axis. The mesh used in these simulations is shown in Fig. 24 and the eight defects show up as small black clusters. Pristine graphite simulations used the same mesh with no defects present.

Material data used as input in Rattlesnake was provided through MD simulations performed by Oliveira [6]. All data reported is for thermal transport along the z -axis of graphite. The Dulong and Petit law [59] states that the molar heat capacity of a solid element is approximately equal to $3R$, where R is the ideal gas constant. Theoretical volumetric heat capacity was calculated in this way. This data is listed in Table 8. Mesh and quadrature data is provided in Table 9. Thermal conductivity for both graphite cases is plotted in Fig. 25.

Properties used in graphite simulation	
Parameter	Value
$T_{b,L}$ [K]	301
$T_{b,R}$ [K]	300
v_g [$\text{m} \cdot \text{s}^{-1}$]	4090
C_v [$\text{J} \cdot \text{m}^{-3} \cdot \text{K}^{-1}$]	$4.697 \cdot 10^6$
$I_{b,L}$ [$\text{W} \cdot \text{m}^{-2}$]	$4.6023 \cdot 10^{11}$
$I_{b,R}$ [$\text{W} \cdot \text{m}^{-2}$]	$4.5870 \cdot 10^{11}$
Λ [m]	$1.485 \cdot 10^{-9}$

Table 8: Graphite simulation parameters

Graphite simulation data			
Element Count	DOFs	Quad. Order	Time [s]
$6.49 \cdot 10^5$	$4.1 \cdot 10^6$	S ₈	368

Table 9: Graphite simulation statistics

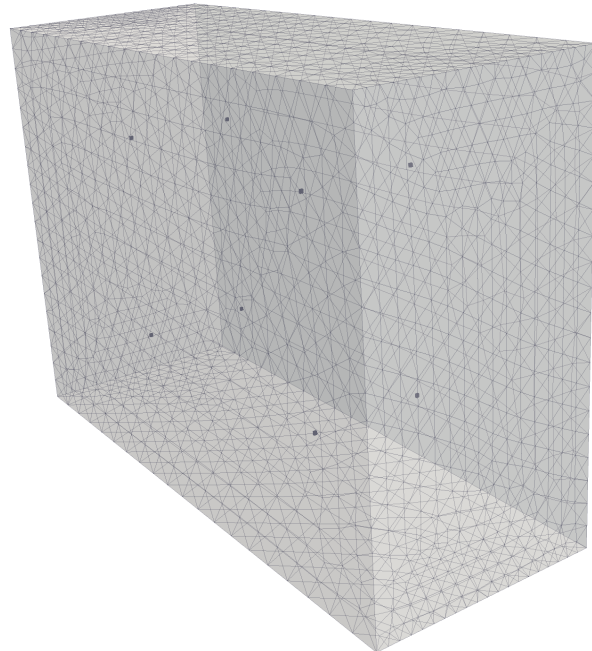


Figure 24: Mesh used in graphite scattering simulations

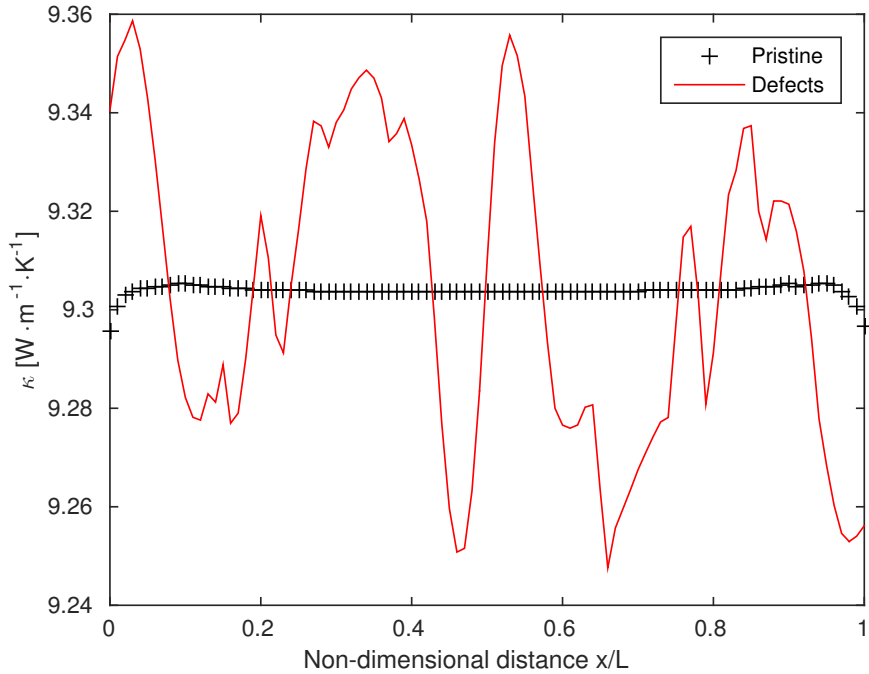


Figure 25: Thermal conductivity along z -axis

4.5 Thermal Conductivity in Single Crystal UO_2

Gofryk et al. [8] measured thermal conductivity in pristine samples of uranium dioxide to determine its anisotropic nature. Figure 26 [8] shows the experimental thermal conductivity in three prime directions for the sample between 4 K and 300 K.

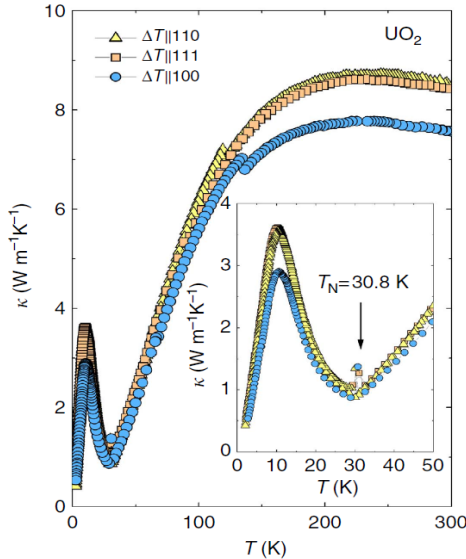


Figure 26: Experimental thermal conductivity for pristine UO_2 in $\langle 100 \rangle$, $\langle 110 \rangle$ and $\langle 111 \rangle$ directions

Experimental measurement of thermal conductivity were performed on samples of uranium dioxide from Los Alamos National Laboratory (LANL) which had dimensions of approximately (x, y, z) 1 mm x 1 mm x 7 mm. Laue back-reflection X-ray diffraction was used to measure the angle of misalignment in the $\langle 111 \rangle$ direction and is shown in Fig. 27 [8]. For a perfect orientation in $\langle 111 \rangle$, the lines should all go through the center of the picture. The estimation of misalignment by Gofryk et al. was less than 0.5 degrees in the $\langle 111 \rangle$ direction [8].

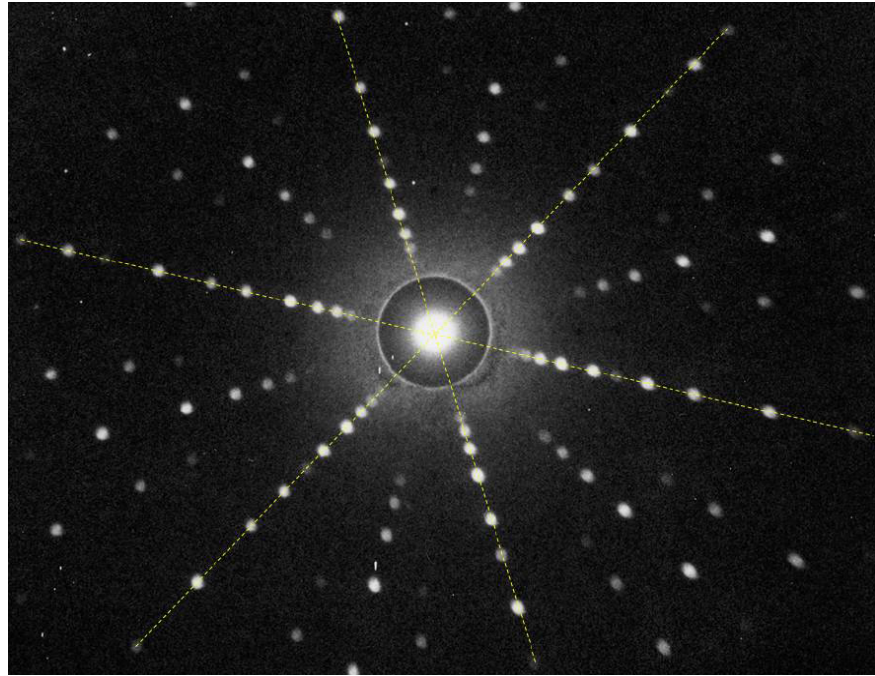


Figure 27: Laue back-reflection X-ray of UO_2 sample in $\langle 111 \rangle$ direction

In order to simulate the experiment with Rattlesnake, the phonon group velocity, volumetric specific heat capacity and mean free path are needed. Gofryk et al. reported phonon group velocity in the UO_2 sample of $v_g = 2965 \text{ m} \cdot \text{s}^{-1}$. They did not include a value for the specific heat capacity. Theoretical volumetric heat capacity for uranium dioxide was calculated using the Dulong-Petit law. Table 10 contains material properties and parameters used in the simulation. Table 11 contains numerical simulation data.

Properties for single crystal UO ₂ simulation	
Parameter	Value
$T_{b,L}$ [K]	301
$T_{b,R}$ [K]	300
v_g [m · s ⁻¹]	2965
C_v [J · m ⁻³ · K ⁻¹]	$1.013 \cdot 10^6$
$I_{b,L}$ [W · m ⁻²]	$7.1963 \cdot 10^{10}$
$I_{b,R}$ [W · m ⁻²]	$7.1723 \cdot 10^{10}$

Table 10: Single crystal UO₂ simulation parameters

Single Crystal UO ₂ Test Data				
Cell Length	Element Count	DOFs	Quad. Order	Time [s]
8	12312	$1.7 \cdot 10^6$	S ₈	112
15	12825	$1.85 \cdot 10^6$	S ₈	147
30	13104	$1.93 \cdot 10^6$	S ₈	172
60	11664	$1.8 \cdot 10^6$	S ₈	196
Superlattice	26450	$3.5 \cdot 10^6$	S ₈	250

Table 11: Single crystal UO₂ simulation statistics

Phonon mean free paths were obtained from the kinetic theory relationship $\kappa = \frac{1}{3}C_v v_g \Lambda$. Table 12 [8] lists the mean free paths obtained for all three crystal directions. Gofryk et al. performed MD simulations to provide validation for their experiments. They used simulation cells which were 3.8 nm x 3.8 nm in the x and y dimensions, and varied in length along the z coordinate between 8 nm and 60 nm. A geometry was constructed for Rattlesnake with these dimensions, as well as a superlattice approximately 10 phonon mean free paths (~ 85 nm) in the z -axis. Transport simulations were performed in the $\langle 100 \rangle$ and $\langle 111 \rangle$ directions at 300 K. The $\langle 110 \rangle$ direction was ignored as its thermal conductivity is very similar to the $\langle 111 \rangle$ direction.

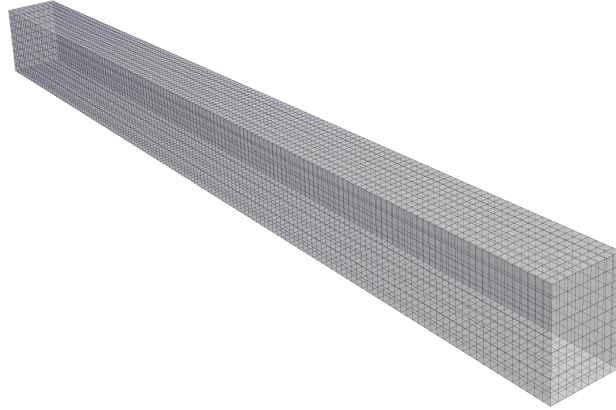


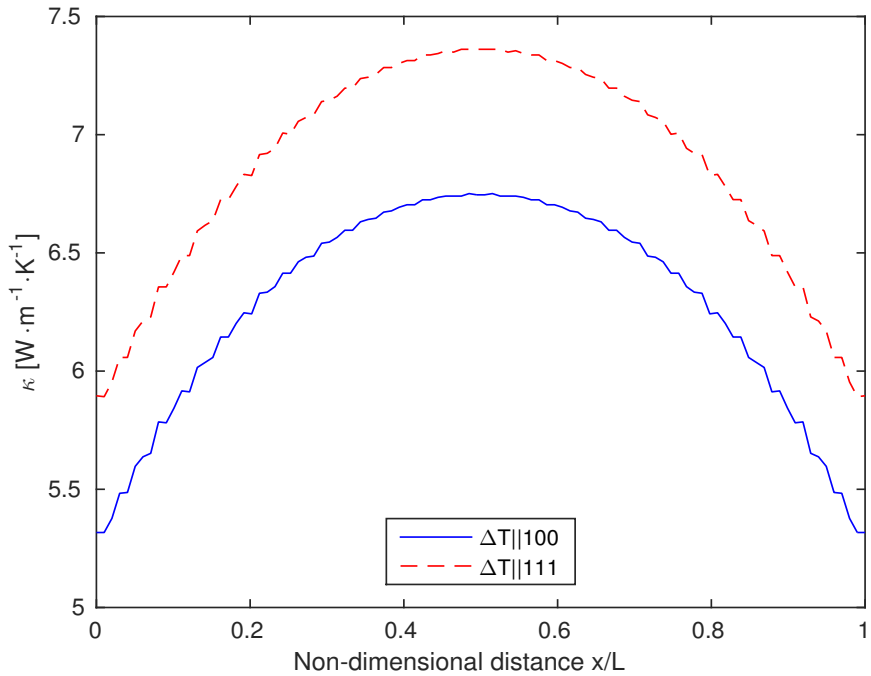
Figure 28: Mesh used in UO_2 single crystal simulation

Λ from Gofryk et al.	
Crystal Direction	Λ [m]
$\langle 100 \rangle$	$7.56 \cdot 10^{-9}$
$\langle 110 \rangle$	$8.00 \cdot 10^{-9}$
$\langle 111 \rangle$	$8.41 \cdot 10^{-9}$

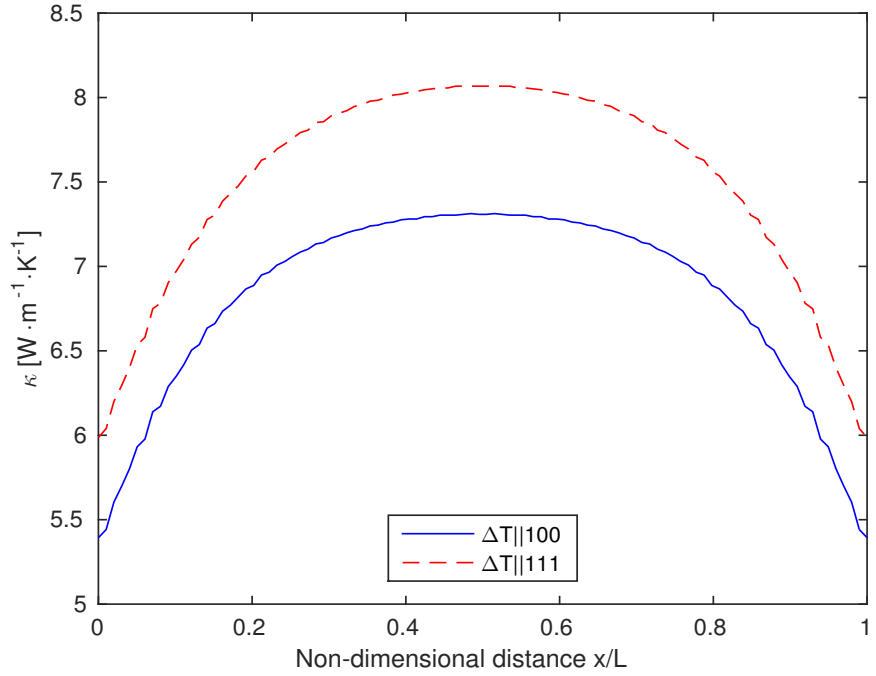
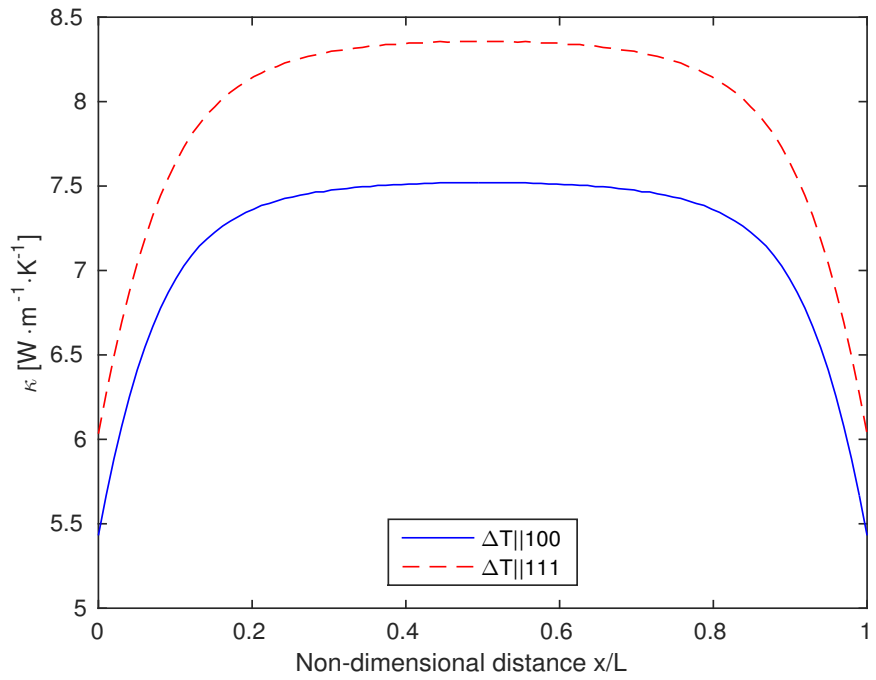
Table 12: Experimentally determined mean free path

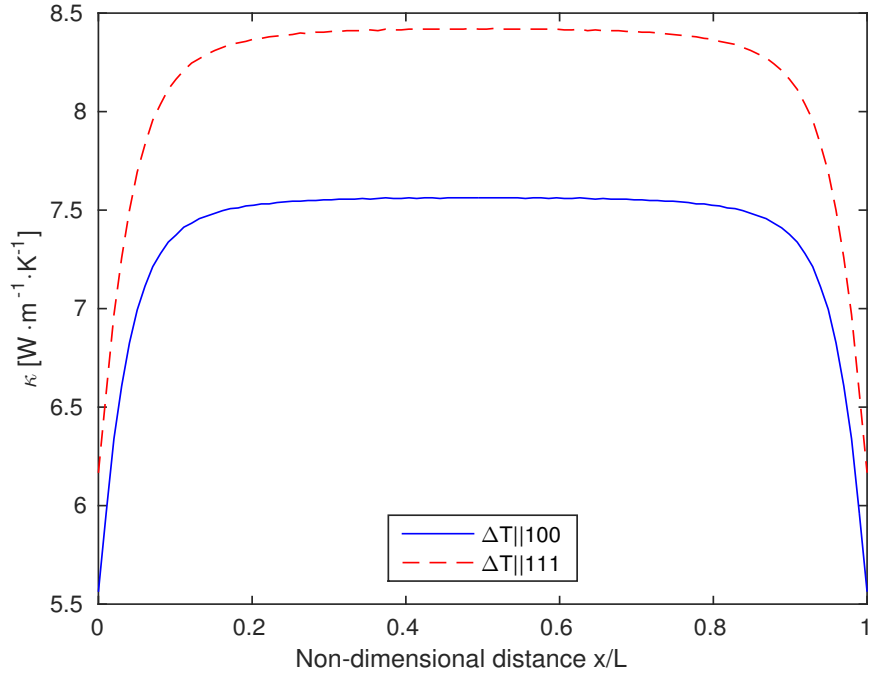
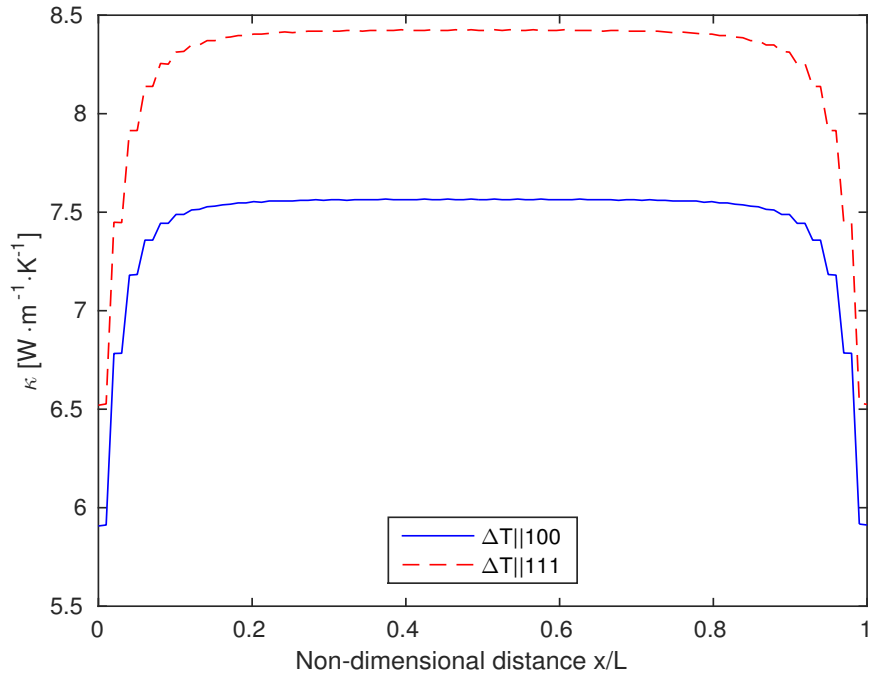
The different simulation cell lengths were likely used to classify and understand the boundary effects associated with the geometry of phonon transport simulations. Simulation boxes of 8, 15, 30 and 60 nm lengths were used, with a temperature gradient of 1 K ($T_{z,L} = 301$ K, $T_{z,R} = 300$ K). Thermal conductivity data for different cell lengths and directions are reported in Table 13.

Thermal conductivity in different cell lengths		
Cell Length [nm]	$\langle \kappa_{100} \rangle [\text{W} \cdot \text{m}^{-1} \cdot \text{K}^{-1}]$	$\langle \kappa_{111} \rangle [\text{W} \cdot \text{m}^{-1} \cdot \text{K}^{-1}]$
8	6.27	6.86
15	6.80	7.49
30 nm	7.18	7.94
60 nm	7.37	8.18
Superlattice	7.43	8.26

Table 13: κ in varying cell lengthFigure 29: κ at 8 nm cell length

Figures 29 - 32 show values of thermal conductivity for different cell lengths in the $\langle 100 \rangle$ and $\langle 111 \rangle$ directions. Thermal conductivities are reported in Table 14, and values from [8] were interpolated at 300 K.

Figure 30: κ at 15 nm cell lengthFigure 31: κ at 30 nm cell length

Figure 32: κ at 60 nm cell lengthFigure 33: κ in superlattice

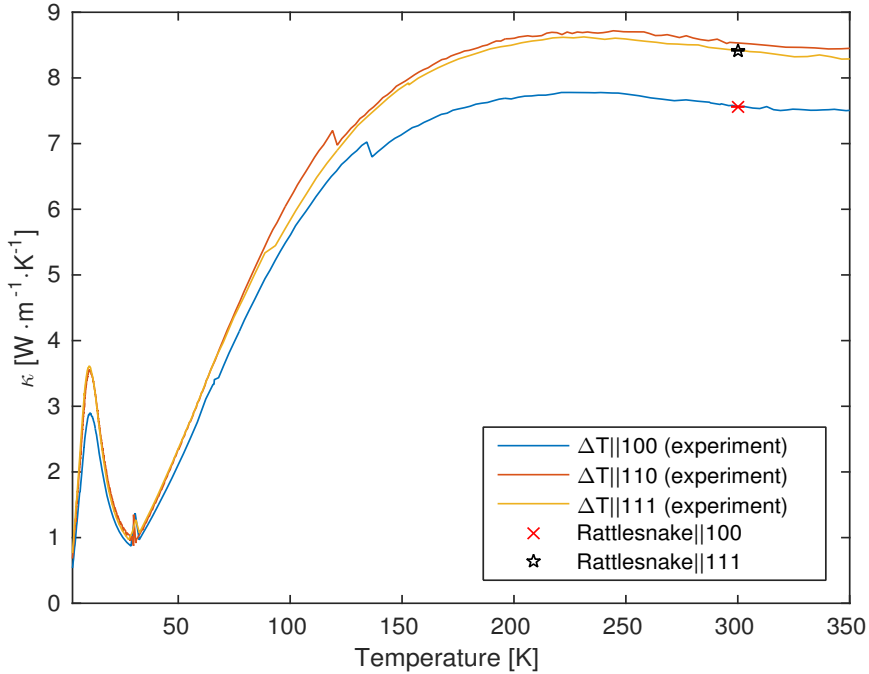


Figure 34: Comparison of thermal conductivities

κ [W·m⁻¹·K⁻¹]		
Crystal Direction	Gofryk et al. [8]	Rattlesnake
$\langle 100 \rangle$	7.57	7.43
$\langle 111 \rangle$	8.44	8.26

Table 14: Thermal conductivity comparison

4.6 UO₂ with Xenon Defects

Los Alamos National Laboratory conducted a MD study to determine the effect of xenon presence on thermal conductivity in UO₂. Rattlesnake transport simulations were performed to compare against this study. The paper presented by Du et al. [9] performed MD studies in UO₂ with various simulation environments, xenon bubbles at different locations in a cell of UO₂ with and without grain

boundaries incorporating between one and three xenon bubbles. They performed all simulations at temperatures of 300 K, 800 K and 1500 K.

Mean free path for uranium dioxide were extracted through the kinetic theory relationship in defect-free UO_2 [9]. Thermal conductivity for xenon was obtained separately from Kestin et al. [60]. Volumetric heat capacity in xenon was calculated through [59], but is multiplied by a factor of $\frac{1}{2}$ as it is a monoatomic gas.

A simulation cell with dimensions of 3.8 nm x 3.8 nm x 25 nm was used in Du et al. [9], this was kept consistent in Rattlesnake simulations. Table 15 [9, 61] contains phonon mean free path data. Here, the quantity $\zeta = \frac{\Lambda_{\text{UO}_2}}{\text{Cell}}$ is introduced. A xenon bubble with radius $r_{\text{Xe}} = 1 \text{ nm}$ was placed in the center of the cell. Table 16 contains data used for the input. Figure 35 is the mesh constructed for the simulations. All simulations were conducted along the $\langle 111 \rangle$ crystallographic direction.

Λ for all simulation temperatures				
Temperature [K]	Crystal Direction	$\Lambda_{\text{UO}_2} [10^{-9} \text{ m}]$	$\Lambda_{\text{Xe}} [10^{-7} \text{ m}]$	$\zeta = \frac{\Lambda_{\text{UO}_2}}{\text{Cell}}$
300	$\langle 111 \rangle$	18.868	1.647	0.7559
800	$\langle 111 \rangle$	8.4637	3.947	0.339
1500	$\langle 111 \rangle$	4.4715	6.227	0.1791

Table 15: Values of Λ

Properties for $\text{UO}_2 + \text{Xe}$ simulation			
Temperature [K]	300	800	1500
$v_g [\text{m} \cdot \text{s}^{-1}]$	2965	2965	2965
$C_v [\text{J} \cdot \text{m}^{-3} \cdot \text{K}^{-1}]$	$1.013 \cdot 10^6$	$1.013 \cdot 10^6$	$1.013 \cdot 10^6$
$I_{\text{b},\text{L}} [\text{W} \cdot \text{m}^{-2}]$	$7.1963 \cdot 10^{10}$	$1.9150 \cdot 10^{11}$	$3.5886 \cdot 10^{11}$
$I_{\text{b},\text{R}} [\text{W} \cdot \text{m}^{-2}]$	$7.1723 \cdot 10^{10}$	$1.9126 \cdot 10^{11}$	$3.5862 \cdot 10^{11}$

Table 16: $\text{UO}_2 + \text{Xe}$ simulation parameters

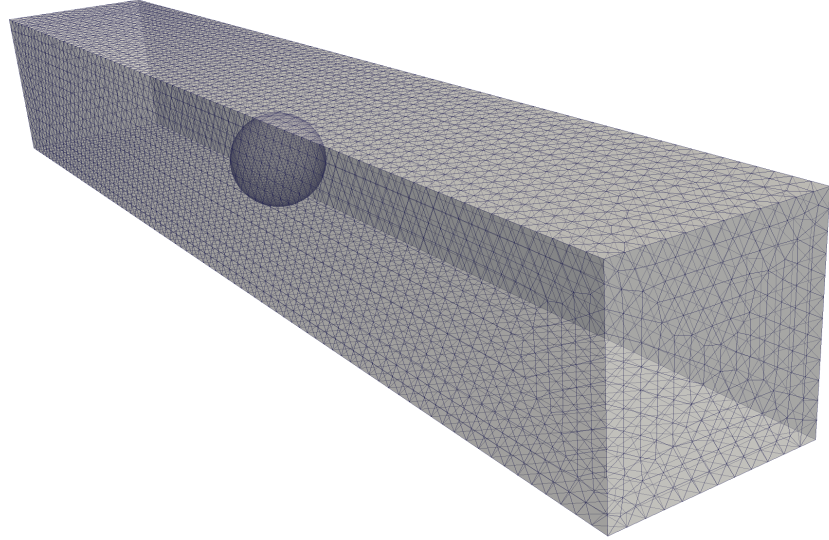


Figure 35: Mesh used in $\text{UO}_2\text{-Xe}$ simulations

UO ₂ + Xe simulation data				
Cell Length	Element Count	DOFs	Quad. Order	Time [s]
25 nm	$350 \cdot 10^3$	$6 \cdot 10^6$	S ₈	1100

Table 17: UO₂ + Xe simulation statistics

Figures 36 - 38 show dimensionless temperature in the direction of transport. Figure 39 is a composition of all three temperatures. Heat flux at all temperatures is reported in Table 18. Figure 44 shows heat flux at 300 K, 800 K and 1500 K.

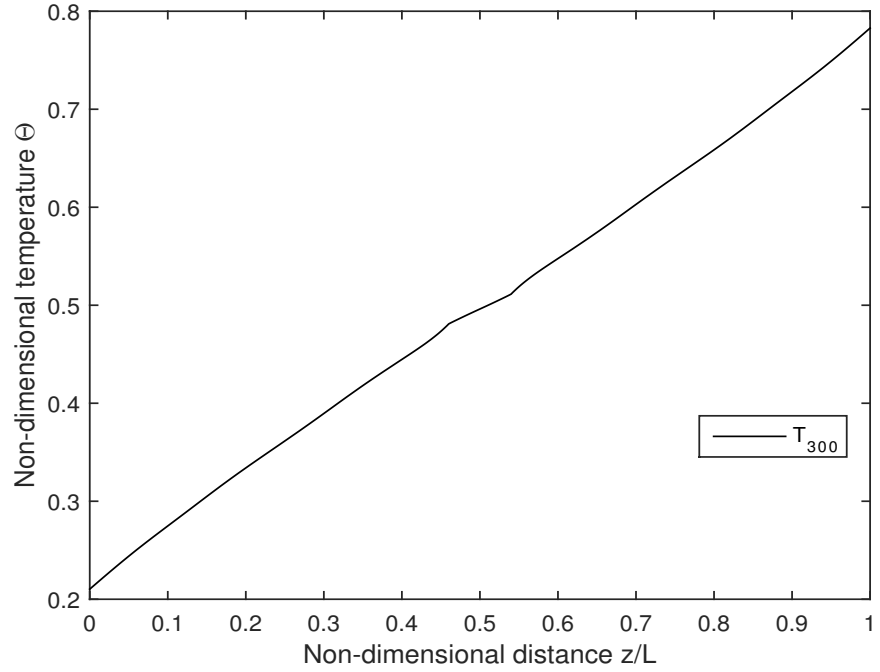


Figure 36: Non-dimensional temperature across z -axis at 300 K

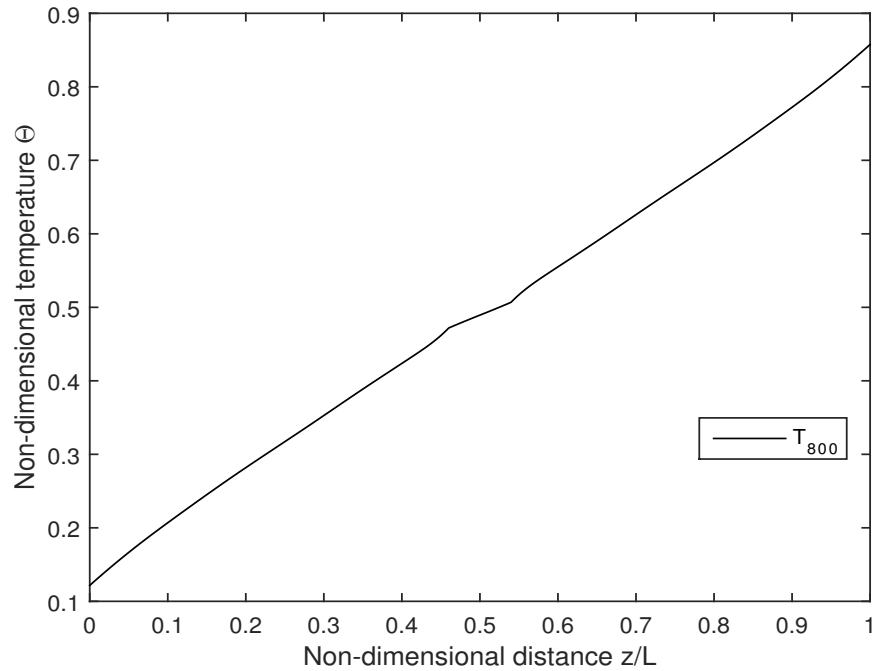


Figure 37: Non-dimensional temperature across z -axis at 800 K

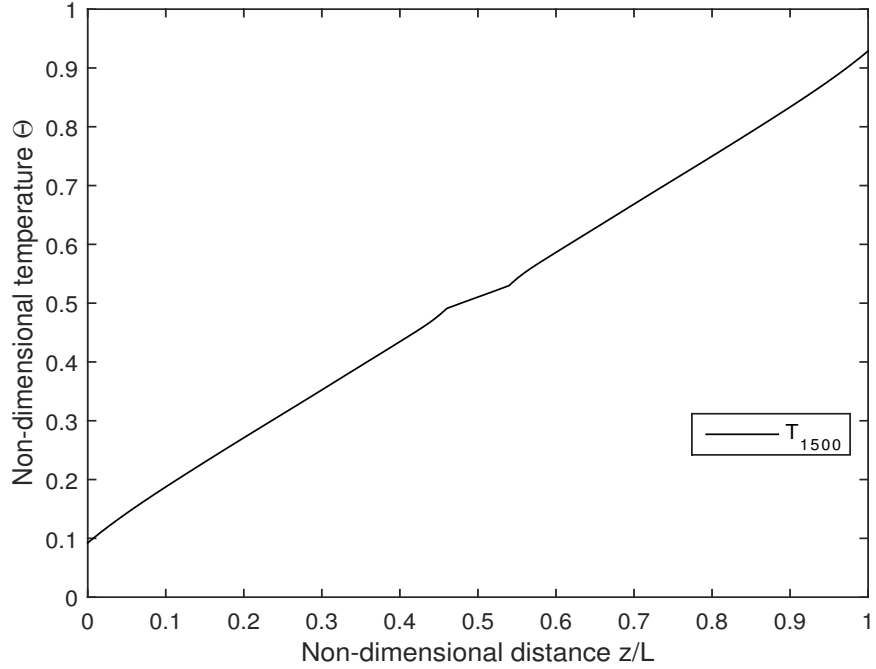


Figure 38: Non-dimensional temperature across z -axis at 1500 K

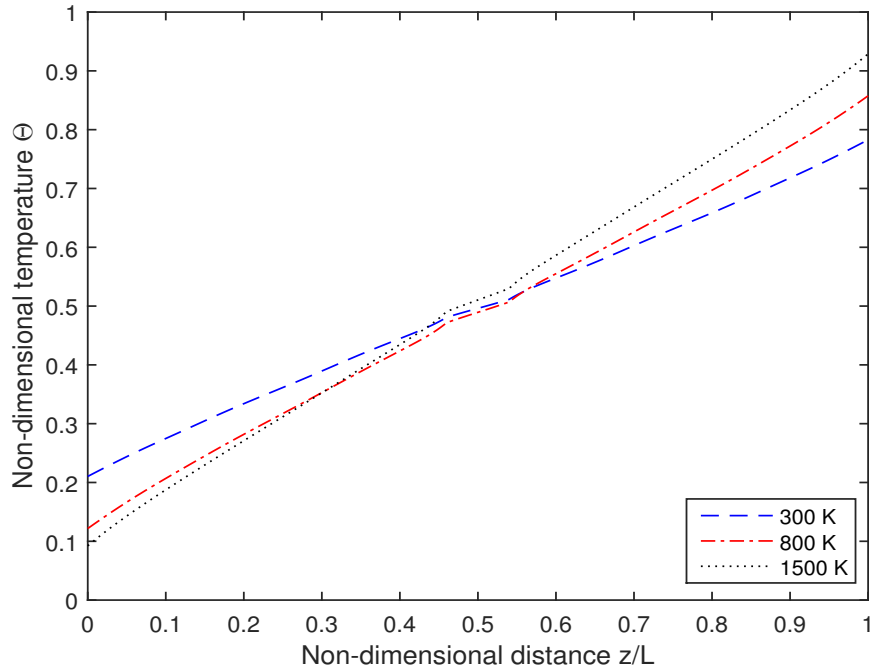
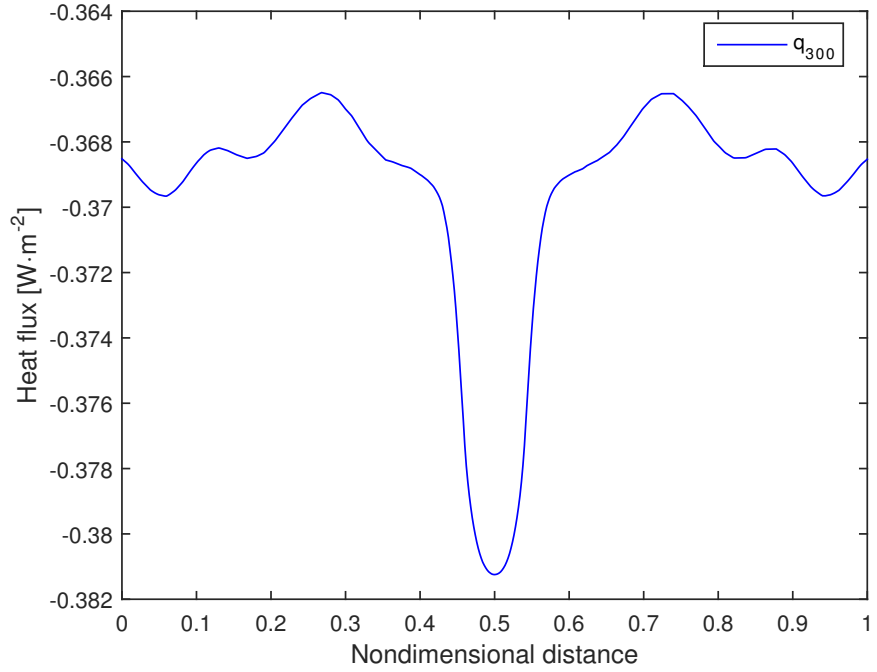
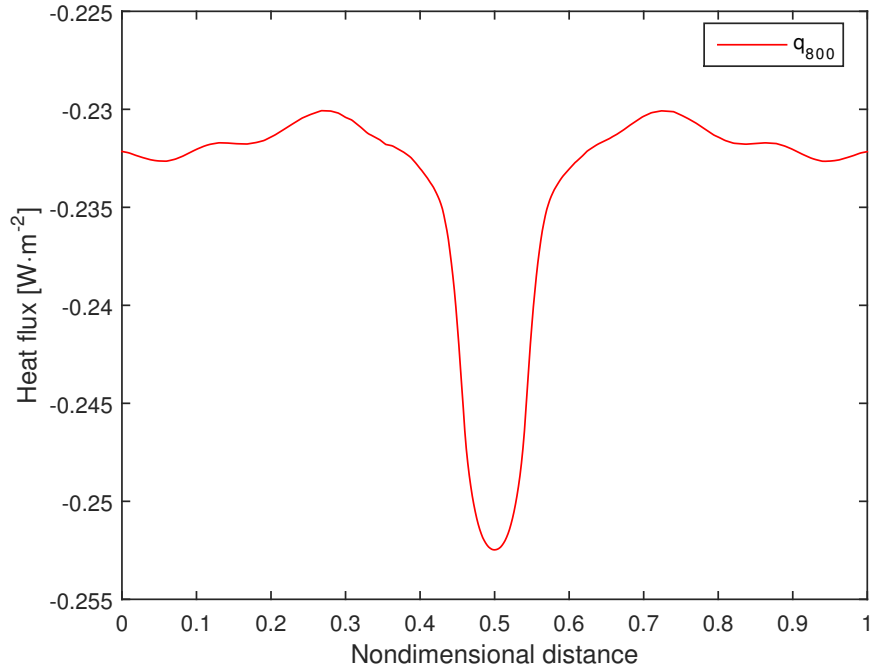


Figure 39: Non-dimensional temperature across z -axis at 300 K, 800 K and 1500 K

Figure 40: Heat flux across z -axis at 300 KFigure 41: Heat flux across z -axis at 800 K

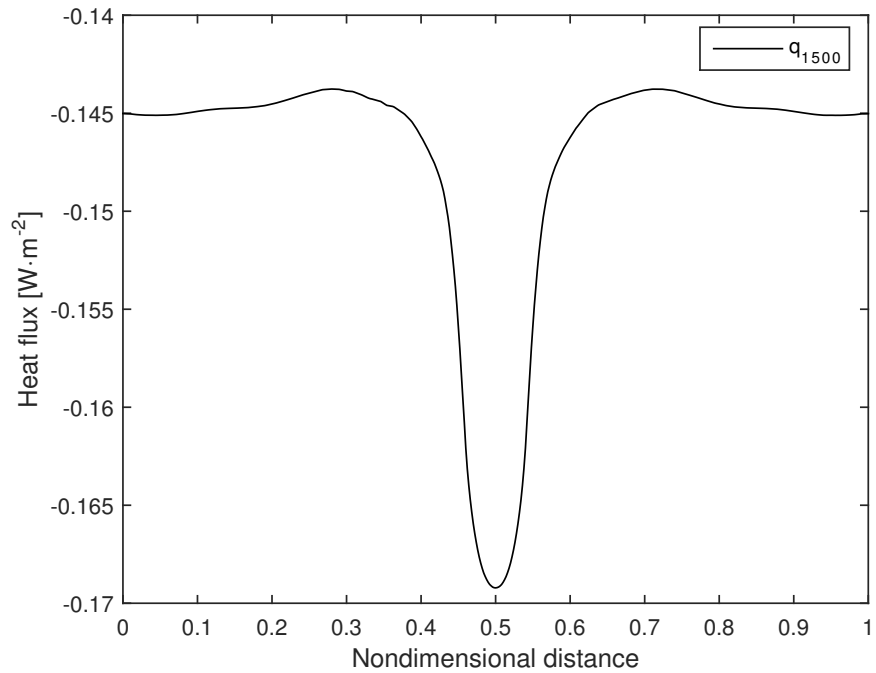


Figure 42: Heat flux across z -axis at 1500 K

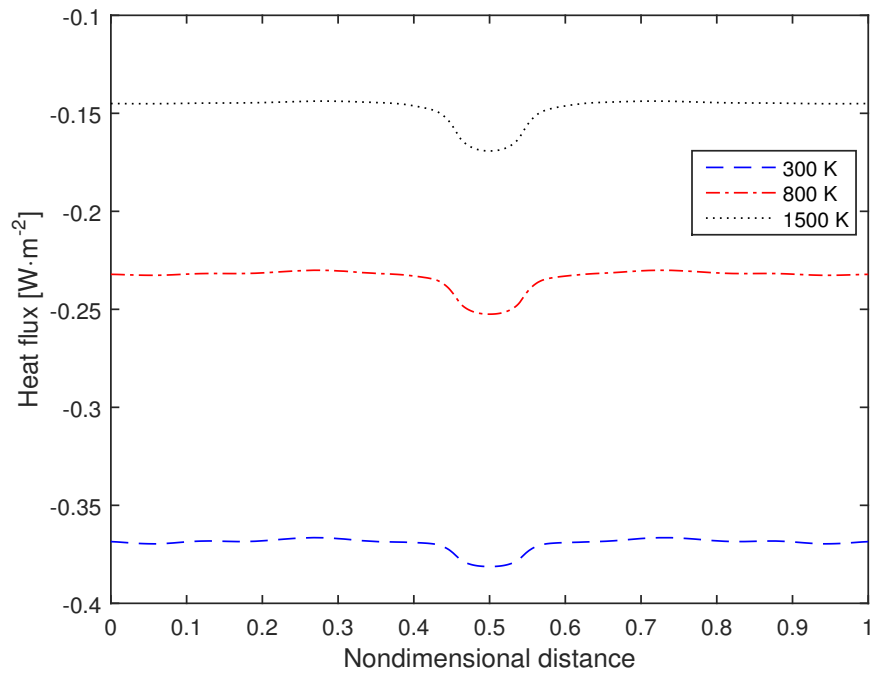


Figure 43: Heat flux across z -axis at 300 K, 800 K and 1500 K

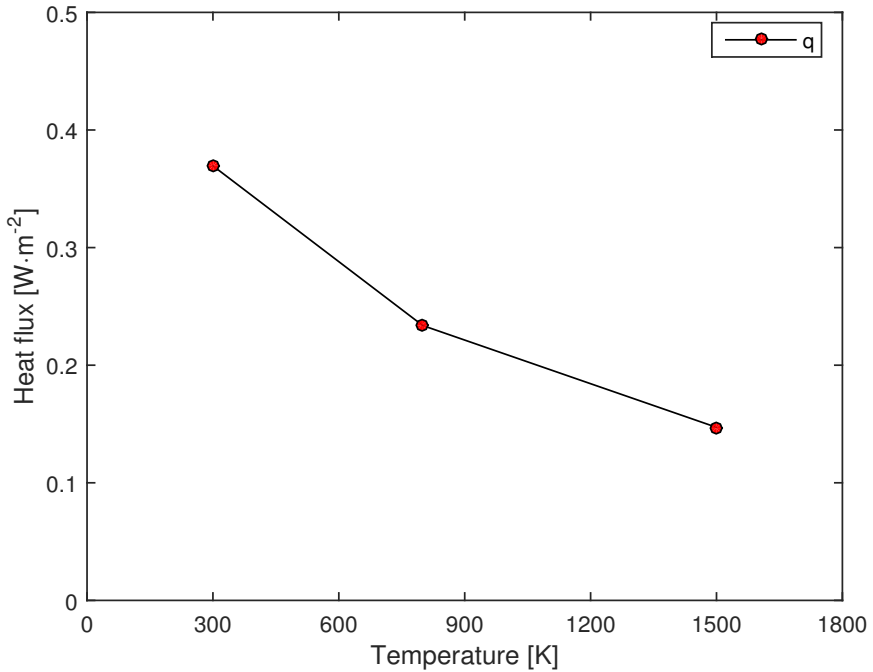
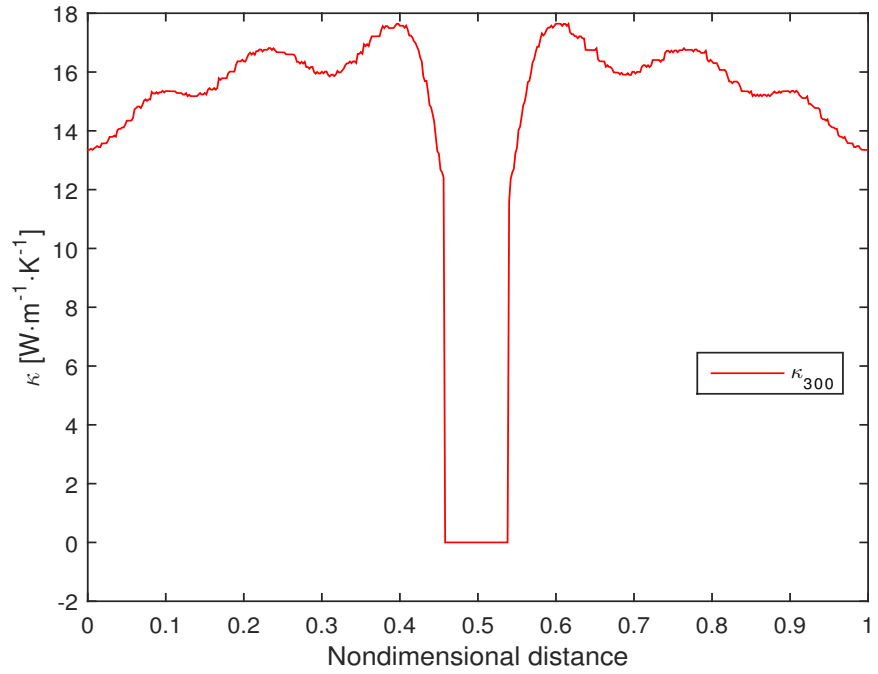
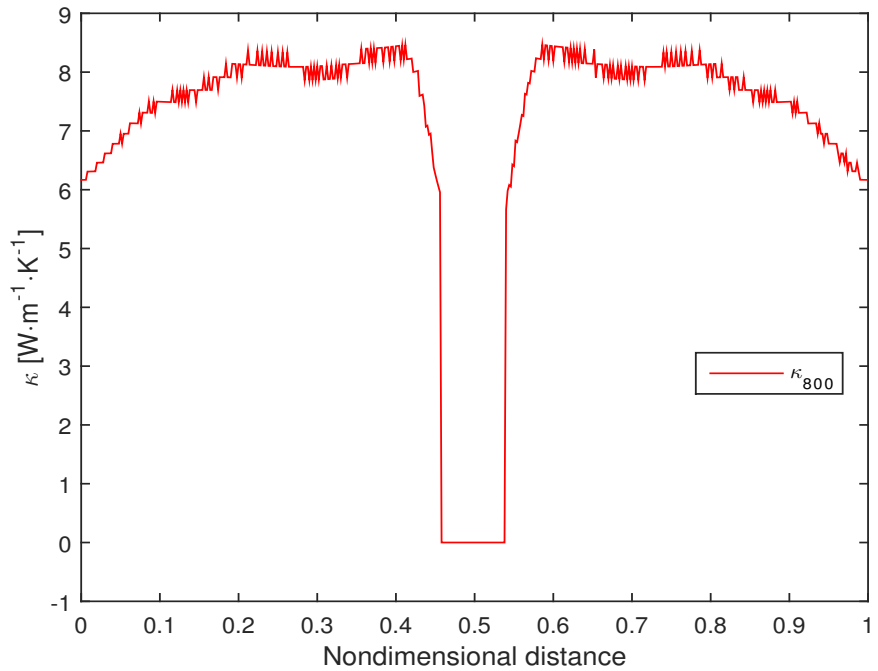
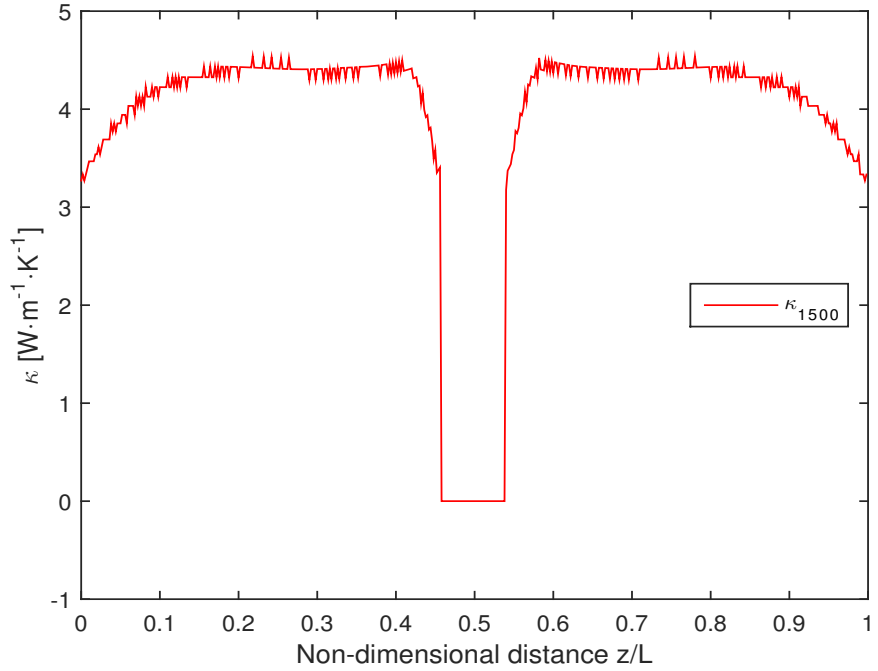
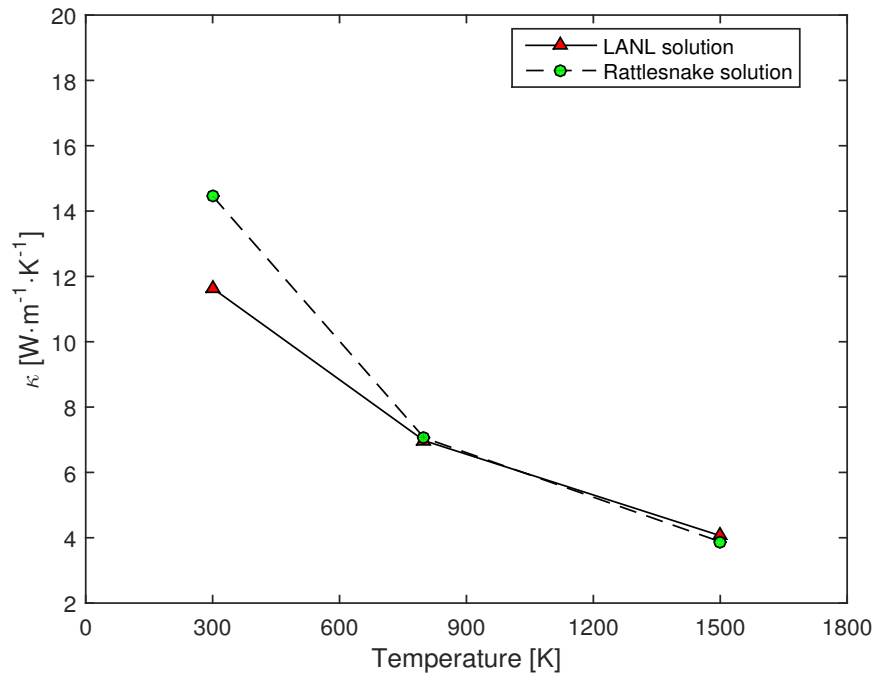


Figure 44: Mean heat flux across z -axis at 300 K, 800 K and 1500 K

Heat flux in UO_2 and Xe	
Temperature [K]	q [$\text{W} \cdot \text{m}^{-2}$]
300	0.369
800	0.234
1500	0.147

Table 18: Mean heat flux in $\text{UO}_2 + \text{Xe}$

Figure 45: κ across z -axis at 300 KFigure 46: κ across z -axis at 800 K

Figure 47: κ across z -axis at 1500 KFigure 48: Thermal conductivity across z -axis at 300 K, 800 K and 1500 K versus Du et al.

Thermal conductivity along the z -axis is shown in Figs. 45 - 47 for all temperatures and is reported in Table 19.

Thermal conductivity values				
Temperature [K]	κ_{RS} [$\text{W} \cdot \text{m}^{-1} \cdot \text{K}^{-1}$]	κ_{MD} [$\text{W} \cdot \text{m}^{-1} \cdot \text{K}^{-1}$] [9]		$\Delta\kappa$
300	14.46	11.64		+19.5%
800	7.06	6.97		+1.27%
1500	3.88	4.06		-4.43%

Table 19: Thermal conductivity in UO_2 with Xe

4.7 Summary

Transport results for the five case studies have been presented. All results were generally favorable, with deterministic transport showing good agreement with most cases of MD simulation. In particular, transport solutions for the case of uranium dioxide with xenon presence relate well to the solutions presented by Du et al. [9]. Some discrepancy exists in the low temperature solutions, this is attributed to the behavior of xenon in the UO_2 lattice. Conclusions are presented in the next chapter.

5 CONCLUSIONS

5.1 Introduction

The results from Chapter 4 are discussed here. The focus of this work is to predict thermal conductivity in heterogeneous nuclear fuel with fission product defects. However, it was first necessary to characterize deterministic phonon transport using Rattlesnake. Here the efficacy of Rattlesnake is discussed, and conclusions are drawn regarding its ability to simulate phonon transport. Proposals for future work in developing Rattlesnake as a phonon transport code are discussed.

5.2 Discussion of Results

The objectives of this research were to investigate the phonon transport capabilities of Rattlesnake by performing deterministic phonon transport simulations against problems with known solutions. These objectives were met and the results have revealed pathways for future development of Rattlesnake as a phonon transport engine. Predicting thermal conductivity in UO_2 with fission product defects is of primary interest to the nuclear materials science community [8, 9, 49, 50].

5.2.1 Thin Film Transport

The work of Yilbas and Bin Mansoor was influential in the initial investigation of deterministic phonon transport simulations using the SAAF formulation of the BTE. Figure 10 shows the Rattlesnake solutions as compared to the results from Yilbas and Bin Mansoor [26]. The coarse and fine mesh results are in very good agreement with the test problem solution. The solution is highly linear, consistent

with other numerical solutions of the EPRT [12, 23].

The shape of the Yilbas and Bin Mansoor solution has a slight curvature, with a depression above the midpoint and an inflection below. The plot of the Rattlesnake solutions appear to be sharply linear in contrast. This difference is likely due to the higher fidelity of the Rattlesnake calculation, with greater angular resolution. The finite element discretization scheme, as opposed to the finite difference scheme used by Yilbas and Bin Mansoor, may also have an effect.

Figures 11 and 12 show the results of angular quadrature and mesh refinement studies. In both studies, the results do not change by appreciable amounts despite large changes in angular resolution and element count. The results of these refinement studies show that for a simple homogeneous medium, the choice of quadrature and mesh size can be minimized to an S_8 quadrature, an element count of 1000 and yield accurate results quickly. However with a small quadrature set, values at the boundaries have a greater relative deviation from the Yilbas and Bin Mansoor solutions, as well as the Rattlesnake solutions obtained with quadratures greater than S_8 . More complicated simulations may require a higher element count to properly resolve the spatial dimension.

Rattlesnake provides accurate solutions to the EPRT as shown here, which reflect the solutions to the EPRT from Yilbas and Bin Mansoor among others [12, 23, 25–27]. However, these results are for a problem which has been widely modeled in literature and does not necessarily prove Rattlesnake to be effective for more advanced simulations, i.e. heterogeneous species or simulations with scattering centers.

5.2.2 Two Material System

An important phenomenon to model with a two-component system is the effect of differing size domains of material and the difference in the phonon mean free path between elements. Through modeling the work of Ali and Yilbas [29] insight is gained to how Rattlesnake is able to capture phonon transport physics at interfaces. Additionally, classification of effects of ballistic and diffuse phonon scattering at small and larger length scales of material is possible. Ali and Yilbas also investigated temporal effects in their work and a transient simulation of this system is performed.

Ali and Yilbas [29] investigated the effects of thermal excitation on phonon transport in a two dimensional silicon thin film. The heat source was provided in the form of an aluminum “quantum dot” which was modeled at the center of a silicon square. The temperature at the edges of this thermal source was varied exponentially with time, and the effect of the perturbation on the phonon transport behavior in the thin film was investigated. Both the phonon intensity distribution and thermal conductivity are reported, and the latter is validated against numerical results existing in open literature. Their numerical approach involved a frequency dependent formulation of the Boltzmann transport equation.

The numerical methods used by Ali and Yilbas bear a resemblance those used by Yilbas and Bin Mansoor [26], though there are some distinct differences which show the evolution of the modeling procedures used. The modifications to the approach in [29] were numerous: the addition of k -space wave vector dimension, the quantification of the contribution of optic and acoustic phonons across the transverse and longitudinal branches, and the introduction of transient phonon transport.

In their derivation of the EPRT, Ali and Yilbas included frequency and time dependence. The drive for introducing frequency dependent transport is in the simulation of higher temperature systems; higher temperatures imply that normal and Umklapp phonon scattering plays a larger role. Ali and Yilbas did not address this, but the investigation of this formulation may aid in the future development of Rattlesnake to model additional phonon scattering physics. Ali and Yilbas relate the frequency to wave vector through the phonon dispersion relation

$$D(\omega) = \frac{k^2}{2\pi^2} \frac{dk}{d\omega}, \quad (77)$$

here $D(\omega)$ is the phonon density of states and k is the wave vector. Their two dimensional formulation of the BTE for phonons is

$$\frac{1}{v_k} \frac{\partial I_k}{\partial t} + \cos \theta \frac{\partial I_k}{\partial x} + \sin \theta \sin \phi \frac{\partial I_k}{\partial z} = \frac{I_k^0 - I_k}{\Lambda_k}, \quad (78)$$

as in Yilbas and Bin Mansoor [26], angular dependence of equilibrium phonon intensity I_k^0 is removed. Although the problem models time dependent heat generation from the aluminum dot, the EPRT was derived in a steady state formulation which assumes no internal heat generation. The time rate of change of the internal energy of the system and the heat flux are both zero, $\frac{\partial u}{\partial t} + \nabla \cdot \mathbf{q} = 0$. Ali and Yilbas state the temperature in the spatial domain of the aluminum dot remains constant with the sources applied at the boundaries of dot.

To account for the frequency dependence in their method, Ali and Yilbas apply the phonon dispersion relation for silicon [29] which gives three polarizations and two vibrational modes (acoustic and optic). This leads to a total of six waves, but due to the degenerate state of the transverse waves there were only four curves modeled in their dispersion relation. Their EPRT was solved for each of these

waves. Additional physics would need to be included in Rattlesnake to model these multiple polarizations and vibrational states. In the formulation discussed here, a modification is made to temperature relationship to include the contributions from each phonon branch

$$T(x, z, t) = \frac{\int_0^{k_{max}} \int_0^{2\pi} \int_0^{\pi} I_k \sin \theta d\theta d\phi dk}{\int_0^{k_{max}} (2C_{TA,k}v_{TA,k} + 2C_{LA,k}v_{LA,k} + 2C_{TO,k}v_{TO} + 2C_{LO,k}v_{LO,k}) dk}, \quad (79)$$

where C is the volumetric specific heat capacity, and the indices correspond to the transverse or longitudinal branch, and either the acoustic or optic modes.

Figure 14 shows the temperature distribution from Ali and Yilbas at $t = 15$ ps. A high amount of diffuse scattering is observed in the silicon radiating out of the aluminum source. The mean free path in the aluminum is very short, here phonon scattering is highly ballistic. As the phonons change medium at the aluminum-silicon interface, diffuse scattering begins to dominate and heat migrates in this way through the silicon.

At the time these results were generated, the capability did not exist in Rattlesnake to model the time dependent temperature in the aluminum dot. In its current form, the transport solver in Rattlesnake computes the grey phonon intensity and is unable to quantify the contributions from the wave vector derivation of Ali and Yilbas [29]. This capability could be added in future work.

Figure 18 is the Rattlesnake solution of phonon intensity at steady-state. The aluminum region is the dominant source of phonons. Figure 19 shows the aluminum region enlarged. The forked patterns radiating from the aluminum dot in Figs. 18 and 19 are “ray effects” which are a known simulation artifact characteristic to the discrete ordinates angular discretization. The assumption from Ali and Yilbas that temperature is constant over the aluminum region is not enforced. As a result,

there is a spatial variation in the phonon intensity distribution in the aluminum.

A transient simulation of this system was performed. As the simulation evolves toward an equilibrium state, the silicon temperature boundaries are responsible for initial heating of the region. This is due to a large difference in scale compared to the aluminum temperature boundaries. Figures 22 and 23 show the effect of the silicon dominating the temperature distribution early in the simulation. As the simulation progresses, the high temperature of the aluminum region dominates the intensity map and begins to depress the intensity magnitude contributed by the silicon boundaries. Owing to the difference in mean free path length between aluminum and silicon, reflected phonons from silicon regions provide a small boost in the phonon intensity at the Al/Si interface. Effective steady state conditions are attained at $t \approx 250$ ps.

With the implementation of transient capabilities in the problem modeled in Sec. 4.3, phonon scattering was characterized in systems of two elements. Though currently unable to model time-dependent sources, Rattlesnake classified transport with a static heat source as phonons transitioned between two materials. As development of Rattlesnake continues, this feature can surely be implemented to approximate a time-dependent source. Phonon transport at differing length scales is captured, with temperature distributions being approximately equal to those documented in Ali and Yilbas [29]. Although we were unable to exactly reproduce their results, this simulation was successful in demonstrating the transient capability of Rattlesnake.

5.2.3 Transport in Graphite

The work outlined in this section was the result of a collaborative effort with Laura de Sousa Oliveira and Dr. P. Alex Greaney from Oregon State University. They used MD methods to investigate thermal resistance from irradiation induced defects in graphite. They performed equilibrium molecular dynamics simulations and reported the difference in thermal conductivities due to the presence of clustering and non clustering point defects using the Green-Kubo method [6].

Oliveira used the Green-Kubo formalism to compute thermal conductivity in equilibrium molecular dynamics (EMD) simulations, using a method derived from the fluctuation-dissipation theorem due to equilibrium oscillations in the heat current vector \mathbf{J}_{xx}

$$\kappa_{xx} = \frac{V}{k_B T^2} \int_0^\infty C_{\mathbf{J}_{xx}}(\tau) d\tau. \quad (80)$$

Here V , T and k_B are volume of the region, temperature, and Boltzmann's constant. $C_{\mathbf{J}}(\tau) = \langle \mathbf{J}(t) \mathbf{J}(t + \tau) \rangle$ is the non-normalized heat current autocorrelation function (HCACF). The basis of the HCACF is that it fluctuates about zero and thermal conductivity is related to the length of time at which these fluctuations diminish.

Oliveira was interested in the change in thermal conductivity due to the presence of defects induced through radiation damage. A multitude of defects were simulated including Stone-Wales, interstitials and vacancies. These defects were annealed to obtain the lowest free energy configurations. Figure 49 [6] shows defect contribution to the thermal resistance along the z -axis, and is the collection of defects which were introduced to the graphite structure. The larger slices indicate a higher thermal resistance, which lowers the overall thermal conductivity along the axis of transport.

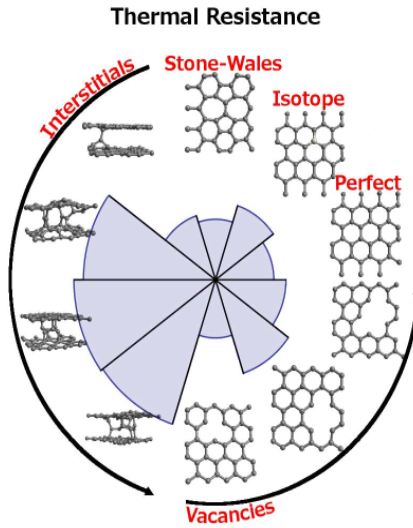


Figure 49: Defect collection

Rattlesnake was unable to resolve the thermal conductivity reported by Oliveira for graphite in the presence of interstitial defect clusters. This is due to the fundamental differences in the way deterministic phonon transport is simulated as compared to MD. As the defects share the same mean free path as the graphite bulk, they will have no effect on the scattering; Rattlesnake will interpret the defect regions as having the same material properties as the surrounding graphite and scattering mechanics will not change. In an attempt to address this shortcoming, reflecting boundary conditions were placed on the defects and were assumed to be at the same temperature as the surrounding graphite. This approach did not yield the thermal conductivity solutions of the molecular dynamics simulations, as is evident from Fig. 25.

In calculations of thermal conductivity in a pristine (defect-free) superlattice of graphite, Rattlesnake yielded results within 2% of the EMD simulations, thermal conductivity in the z -axis of $\kappa \approx 9.3 \text{ W} \cdot \text{m}^{-1} \cdot \text{K}^{-1}$. This is shown in Figure 25,

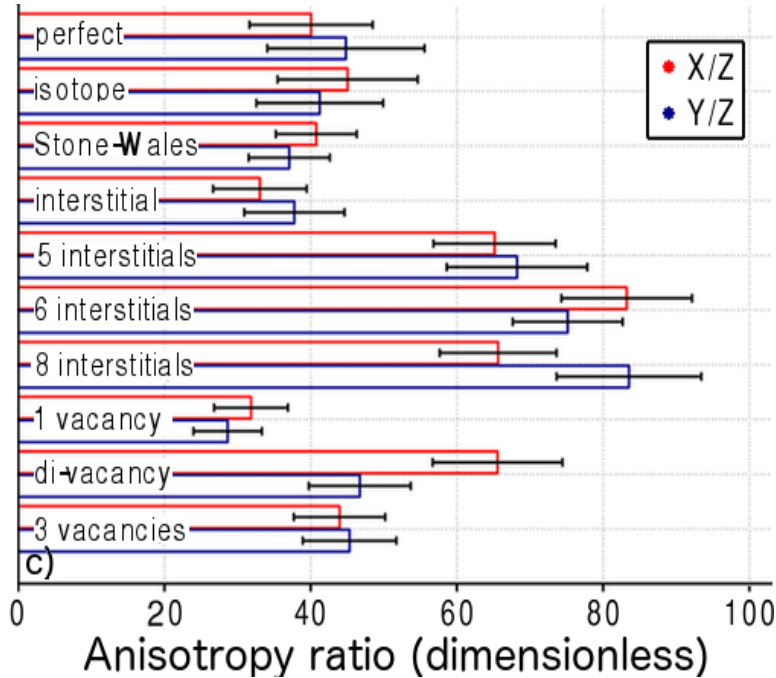


Figure 50: Anisotropy ratios

alongside thermal conductivity for the superlattice with eight interstitial defects. Figure 51 [6] are the thermal conductivities along the z -axis from Oliveira. The value for $\kappa_{z, \text{MD}, 8 \text{ defects}}$ with eight interstitial defects is roughly half of the value calculated by Rattlesnake.

Rattlesnake is able to capture linear anisotropic scattering effects, which allows for the computation of N moments of the angular flux. It is currently unable to simulate the effects of material anisotropy, which is a characteristic MD can simulation. A quantity of interest in MD simulations is the ratio of the anisotropic effect of graphite on the thermal conductivities along the different axes of thermal transport. Oliveira computed these ratios for all of the simulation cases. Figure 50 [6] shows strong anisotropic dependence in the z -axis for the eight defect case, as well as the anisotropic influence from other defect types. The ability to model these

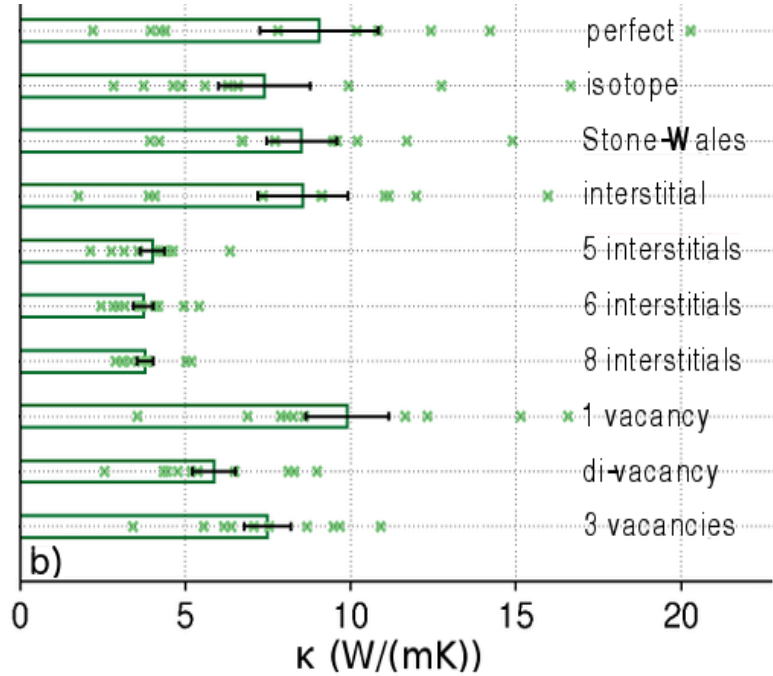


Figure 51: Thermal conductivities along z -axis

effects in Rattlesnake would be a worthwhile capability to add to the code.

Transport simulations performed on pristine graphite with Rattlesnake are shown to reproduce the values of thermal conductivity along the z -axis of graphite within about 2% of MD simulations. The two results are in close agreement with each other and this is a positive outcome in the process of testing Rattlesnake on continually advanced simulations. The difficulty in attaining the same thermal conductivity in the presence of defects is unwelcome, and demonstrates limitations of the code in dealing with defect presence in which the phonon mean free path in the defects is the same as in the bulk material.

Using Rattlesnake to simulate transport in graphite with interstitial defects, the graphite mean free path does not change as phonons interact with the defects. Physically, phonon scattering does change at these interstitials, but Rattlesnake is

unable to resolve this effect. An attempt was made to simulate these defects by applying reflecting boundary conditions to the impurities to approximate them as scattering centers, however this proved to be the wrong approach, evident from Fig. 25. Rattlesnake code does not currently contain the scattering physics necessary to accurately capture local behavior of the phonons scattering off these lattice impurities, this was addressed in Sec. 2.4.3. Molecular dynamics methods are able to quantify these effects, and this is an area where Rattlesnake may further be developed.

5.2.4 Single Crystal UO_2

Uranium dioxide has the stable fluorite crystalline structure CaF_2 . It is cubic in point and space groups which implies isotropic conditions for thermal conductivity. Gofryk et al. suggested that a hidden anisotropy exists in UO_2 which may help explain the unexpected behavior of thermal conductivity in UO_2 .

The trends of the data near the edges of Figs. 29 - 33 show how size of the simulation cell affects phonon scattering behavior. The magnitude of the effect is amplified as the simulation box decreases in size along the z -axis where the temperature gradient is applied. With increasing cell length, the temperature influence of the boundaries have a lesser effect and an equilibrium (“infinite medium”) value of thermal conductivity consistent with Gofryk et al. [8] is found. The Rattlesnake results agree well with experimental values. This is expected due to the near identical input conditions with the application of a mean free path extracted from experimental thermal conductivity.

Figure 34 shows the values of thermal conductivity from the Rattlesnake simulations plotted against the experimental outcome from Gofryk et al. [8]. The values

from the transport simulations are in good agreement with those of experiment. This comparison further demonstrates the capability of Rattlesnake as a phonon transport engine. A true test of the abilities of Rattlesnake is to model a problem in which a mean free path for the bulk material is known, and a mean free path for an impurity is calculated independently. This simulation is illustrated in the following section with the simulation of phonon transport in UO_2 with xenon impurities.

5.2.5 UO_2 with Xenon Defects

Thermal conductivity predicted through Rattlesnake phonon transport generally agrees well with outcomes in Du et al. Rattlesnake is unable to model grain boundaries, and the test case modeled with Rattlesnake focused on a single bubble of xenon in a cell of UO_2 with no grain boundaries. The ratio ζ gives a sense of expected scattering behavior. As ζ approaches unity (the Casimir limit), ballistic scattering is predicted as the dominant scattering mechanism. As ζ decreases, more diffuse scattering is anticipated. The presence of the xenon bubble creates a discontinuity in the non-dimensional temperatures in Figs. 36 - 38.

Heat flux through the cell is affected by mean free path, temperature and ζ . Oscillations are observed at lower temperature, which could be from the highly ballistic scattering or the result of some numerical instability. In Fig. 40, oscillatory behavior is very apparent, but has little overall influence on the solution. The magnitude of the oscillations is approximately 0.2%. The oscillations reduce at elevated temperature, as ζ decreases there is less influence from the boundaries. The presence of the xenon bubble has a dramatic influence on reduction of local heat flux, which has dependence on increasing temperature. More diffuse phonon

scattering occurs as the mean free path decreases in value; the reduction in Λ is significant at the temperature extremes, decreasing by a factor of 4.

Thermal conductivity in Figs. 45 - 47 show a depression at each boundary. This may be an artifact of the very slight curve at the each edge of the non-dimensional temperatures in Figs. 36 - 38. Also present are the oscillations seen in heat flux. The curved edges are due to influence of the boundaries and are also seen in the plots of thermal conductivity in pristine UO_2 (Sec. 4.5). Gofryk et al. and Du et al. both reported this phenomenon [8, 9]. Rattlesnake solutions of thermal conductivity in Fig. 48 generally agree well with the MD solutions from Du et al. [9]. Thermal conductivity at 300 K is elevated compared to [9], but this is likely due to a lack of data for the material properties of xenon in UO_2 at low temperatures. Thermal conductivity for all temperatures are reported in Table 19.

Studies on the behavior of xenon in uranium dioxide have been performed to gain insight into how its density and phase change due to varying atomic forces at the nanoscale [7, 10, 62–64]. In bubbles of small (1-2 nm) radii, xenon experiences extremely high pressures due to strain fields located along bubble edges. The pressure xenon sees is decreased as bubble radius increases [62]. When modeled in a geometric configuration of nanometer diameter bubbles, xenon has been shown to exhibit properties of a solid, rather than those of a gas. Density of the xenon is increased by approximately three orders of magnitude, and the speed of sound in liquid xenon was used as the phonon velocity. Data was readily available for xenon at temperatures above 600 K. A lack of data for low temperature xenon in UO_2 may be a cause in the disparity in thermal conductivity at 300 K compared to results from Du et al.

Rattlesnake was able to produce solutions for thermal conductivity which com-

pare well with MD results when accurate data for xenon is used. The lack of data should not detract from the overall positive outcomes when using Rattlesnake as a phonon transport engine. Results of this study could be improved by performing additional simulations to give thermal conductivity at other values of temperature above 600 K, where material properties of xenon are better understood. The placement of more xenon bubbles to quantify the effects of an increased amount of scattering centers may also be of merit. Bubble radii and location may play a role in further understanding how xenon disrupts thermal transport in UO₂.

5.3 Overall Conclusions and Future Work

In this first approach of predicting thermal conductivity in materials through use of the neutron transport code Rattlesnake, results are generally favorable. The transport behavior of the solutions to the selected test problems is accurate and in many cases agrees well with the results of molecular dynamics simulations. Some shortcomings exist in the modeling of more detailed phonon scattering processes and we shed light on areas where Rattlesnake may be improved as a phonon transport engine.

Because Rattlesnake has proven to be an effective deterministic phonon transport engine, a wealth of possibilities exists to increase its abilities in modeling more complicated phonon transport processes. At its core, Rattlesnake is a radiation transport solver and is unable to resolve some of the more complicated phonon scattering processes which must be quantified to capture all of the effects taking place at the nanoscale. Some of these processes were briefly discussed in Section 2, and many can be naturally incorporated into the MOOSE architecture.

In particular, development of a module to calculate the phonon dispersion re-

lation for arbitrary materials could easily be added, as the equations are in general well understood and used in molecular dynamics codes. The contributions to the relaxation time require a more detailed understanding of scattering physics and frequency dependent transport is required to capture these processes. Modeling normal and Umklapp processes accounts for the inherent anharmonic scattering which takes place in real materials, and is an important component to consider at elevated temperatures [11, 52, 53]. The contributions from these processes are provided through molecular dynamics simulations in modeling the Callaway continuum for thermal conductivity [9, 53]. Developing these physics kernels is another potential pathway in future work with Rattlesnake.

To understand scattering physics occurring at material defects where mean free path is the same as in the bulk, an additional kernel which capture these mechanics could be developed. This scattering kernel would need to include interatomic potentials between various species in a heterogeneous lattice. These potentials are used by a host of MD codes such as LAMMPS [21] and are continually developed as more experimental work is performed to further refine them.

The MOOSE framework has a number of animals (codes) in the herd. One such code is MARMOT, which models 4th order phase fields at the mesoscale. One of the capabilities of MARMOT is generation of meshes with randomized placement of structures such as grain boundaries, lattice imperfections, and nucleation sites. In this work, Rattlesnake used static meshes for a transport platform. In the future, these static meshes can be eradicated and generated meshes with random placement of xenon bubbles or other fission product defects may be created through coupling Rattlesnake to MARMOT. This could be achieved with a relative minimum of work, as the MOOSE architecture allows for direct communi-

cation between the animals in its herd provided the developer has a knowledge of the C++ coding environment.

Applying deterministic methods to simulate phonon transport is an underdeveloped facet of the phonon transport community. Classic Monte Carlo and molecular dynamics approaches can provide detailed information of thermal conductivity, but are computationally expensive. By approaching phonon transport with deterministic methods, accurate calculations of thermal conductivity in nuclear fuels may be obtained. This serves an ultimate purpose of predicting thermal conductivity in operating nuclear power plants (provided appropriate concentrations of fission product defects in the fuel) and in the validation of advanced nuclear fuels for next-generation power reactors, which are currently under development.

BIBLIOGRAPHY

- [1] IAEA, “Thermal Conductivity of Uranium Dioxide,” Tech. rep., International Atomic Energy Agency (1966).
- [2] IAEA, “Thermophysical properties database of materials for light water reactors and heavy water reactors,” Tech. rep., International Atomic Energy Agency (2006).
- [3] M. AMAYA, T. KUBO, and Y. KOREI, “Thermal Conductivity Measurements on UO_{2+x} from 300 to 1400 K,” *Journal of Nuclear Science and Technology* (1996).
- [4] S. POPOV, J. CARBAJO, V. IVANOV, and G. YODER, “Thermophysical Properties of MOX and UO_2 Fuels Including the Effects of Irradiation,” Tech. rep., Oak Ridge National Laboratory (2000).
- [5] V. TENNERY, “Review of Thermal Conductivity and Heat Transfer in Uranium Dioxide,” Tech. rep., Oak Ridge National Laboratory (1959).
- [6] L. DE SOUSA OLIVEIRA, “Thermal resistance from irradiation defects in graphite,” *Computational Materials Science*, **103**, 68–76 (2015).
- [7] J.-Y. OH, Y.-H. KOO, J. S. CHEON, B.-H. LEE, and D.-S. SOHN, “Molecular dynamics simulation of the pressure-volume-temperature data of xenon for a nuclear fuel,” *Journal of Nuclear Materials* (2008).
- [8] K. GOFRYK ET AL., “Anisotropic thermal conductivity in uranium dioxide,” *Nature Communications* (2014).

- [9] S. DU, K. GOFRYK, D. A. ANDERSSON, X.-Y. LIU, and C. STANEK, “A molecular dynamics study of anisotropy and the effect of Xe on UO₂ thermal conductivity,” Tech. rep., Los Alamos National Laboratory (2011).
- [10] M. COLBERT, G. TRÉGLIA, and F. RIBEIRO, “Theoretical study of xenon adsorption in UO₂ nanoporous matrices,” *Journal of Physics: Condensed Matter* (2014).
- [11] C. KITTEL, *Introduction to Solid State Physics*, John Wiley & Sons, Inc., 8th ed. (2005).
- [12] T. KLITSNER ET AL., “Phonon Radiative Heat Transfer and Surface Scattering,” *Physical Review B*, **38**, 11, 7576–7594 (1988).
- [13] H. B. G. CASIMIR, “Notes on the Conduction of Heat in Crystals,” *Physica*, **5**, 6, 495–500 (1938).
- [14] S. MAZUMDER and A. MAJUMDAR, “Monte Carlo Study of Phonon Transport in Solid Thin Films Including Dispersion and Polarization,” *Journal of Heat Transfer*, **123**, 749–759 (August 2001).
- [15] D. LACROIX and K. JOULAIN, “Monte Carlo transient phonon transport in silicon and germanium at nanoscales,” *Physical Review B*, **72**, 6, 11 (August 2005).
- [16] K. TERMENTZIDIS and S. MERABIA, *Molecular Dynamics - Theoretical Developments and Applications in Nanotechnology and Energy*, InTech (2012).
- [17] R. LESAR, *Introduction to Computational Materials Science*, Cambridge University Press (2013).

- [18] T. HORI, T. SHIGA, and J. SHIROMI, “Phonon transport analysis of silicon germanium alloys using molecular dynamics simulation,” *Journal of Applied Physics*, **113** (2013).
- [19] B.-L. HUANG and M. KAVIANY, “*Ab initio* and molecular dynamics prediction for electron and phonon transport in bismuth telluride,” *Physical Review B* (2008).
- [20] L. SUN and J. MURTHY, “Molecular Dynamics Simulation of Phonon Scattering at Rough Semiconductor Interfaces,” in “Thermal and Thermomechanical Phenomena in Electronic Systems,” (2008).
- [21] S. PLIMPTON, “Fast Parallel Algorithms for Short-Range Molecular Dynamics,” *Journal of Computational Physics*, **117**, 1–19 (1995).
- [22] W. HUMPHREY, A. DALKE, and K. SCHULTEN, “VMD – Visual Molecular Dynamics,” *Journal of Molecular Graphics*, **14**, 33–38 (1996).
- [23] A. MAJUMDAR, “Microscale heat conduction in dielectric thin films,” *Journal of Heat*, **115**, 7–16 (February 1993).
- [24] A. MAJUMDAR, “Effect of Interfacial Roughness on Phonon Radiative Heat Conduction,” *Journal of Heat Transfer*, **113**, 797–805 (November 1991).
- [25] B. YILBAS and S. BIN MANSOOR, “Phonon Transport in Two-Dimensional Silicon Thin Film: Influence of Film Width and Boundary Conditions on Temperature Distribution,” *European Physical Journal B*, **85**, 234–242 (2012).
- [26] B. YILBAS and S. BIN MANSOOR, “Lattice Phonon and Electron Temperatures in Silicon-Aluminum Thin Films Pair: Comparison of Boltzmann

Equation and Modified Two-Equation Model,” *Journal of Computational and Theoretical Transport* (2014).

- [27] B. YILBAS and S. BIN MANSOOR, “Transient Effect of Phonon Transport in Two-Dimensional Silicon Film,” *Numerical Heat Transfer* (2012).
- [28] B. YILBAS and S. BIN MANSOOR, “Radiative phonon transport in silicon and collisional energy transfer in aluminum films due to laser short-pulse heating: Influence of laser pulse intensity on temperature distribution,” *Optics & Laser Technology* (2011).
- [29] H. ALI and B. YILBAS, “Phonon Transport in a Silicon Film with Presence of an Aluminum Dot in the Film,” *The Journal of Computational and Theoretical Transport* (2014).
- [30] A. BULUSU and D. WALKER, “One-dimensional thin-film phonon transport with generation,” *Microelectronics Journal*, **39**, 7, 950–956 (2008).
- [31] J. D. CHUNG and M. KAVIANY, “Effects of phonon pore scattering and pore randomness on effective conductivity of porous silicon,” *International Journal of Heat and Mass Transfer* (1999).
- [32] M. GALLER and F. SCHÜRRER, “A deterministic solution method for the coupled system of transport equations for the electrons and phonons in polar semiconductors,” *Journal of Physics A: Mathematical and General* (2004).
- [33] M. GALLER and F. SCHÜRRER, “A deterministic solver for the transport of the AlGaN/GaN 2D electron gas including hot-phonon and degeneracy effects,” *Journal of Computational Physics* (2005).

- [34] S. KUMAR, A. MAJUMDAR, and C. TIEN, “The Differential Discrete Ordinate Method for Solving the General Equation of Radiative Transfer,” *Journal of Heat*, **113**, 424–429 (1990).
- [35] A. MITTAL and S. MAZUMDER, “Hybrid discrete ordinates-spherical harmonics solution to the Boltzmann Transport Equation for phonons for non-equilibrium heat conduction,” *Journal of Computational Physics* (2011).
- [36] A. NABOVATI, D. SELLAN, and C. AMON, “On the lattice Boltzmann method for phonon transport,” *Journal of Computational Physics* (2011).
- [37] S. SRINIVASAN, R. MILLER, and E. MAROTTA, “Parallel Computation of the Boltzmann Transport Equation for Microscale Heat Transfer in Multilayered Thin Films,” *Numerical Heat Transfer, Part B*, **46**, 31–58 (2004).
- [38] D. TERRIS, K. JOULAIN, D. LACROIX, and D. LEMMONIER, “Numerical simulation of transient phonon heat transfer in silicon nanowires and nanofilms,” *Journal of Physics: Conference Series*, **92** (2007).
- [39] R. YANG, G. CHEN, and M. DRESSELHAUS, “Thermal Conductivity Modeling of Core-Shell and Tubular Nanowires,” *Nano Letters*, **5**, 6, 1111–1115 (2005).
- [40] J. DUDEKSTADT and L. HAMILTON, *Nuclear Reactor Analysis*, Wiley (1976).
- [41] J. DUDEKSTADT and W. MARTIN, *Transport Theory*, John Wiley & Sons, Inc. (1979).
- [42] E. LEWIS and W. MILLER, *Computational Methods of Neutron Transport*, Wiley-Interscience (1993).

- [43] J. MOREL and J. MCGHEE, “A Self-Adjoint Angular Flux Equation,” *Nuclear Science and Engineering*, **3**, 12, 312–325 (1999).
- [44] D. GASTON ET AL., “MOOSE: A Parallel Computational Framework for Coupled Systems of Nonlinear Equation,” *Nuclear* (2009).
- [45] Y. WANG, H. ZHANG, and R. MARTINEAU, “Diffusion Acceleration Schemes for Self-Adjoint Angular Flux Formulation with a Void Treatment,” *Nuclear Science and Engineering*, **176**, 201–225 (2014).
- [46] Y. WANG, “Nonlinear Diffusion Acceleration for the Multigroup Transport Equation Discretized with S_N and Continuous FEM with Rattlesnake,” in “M&C 2013,” (2013).
- [47] F. GLEICHER, Y. WANG, D. GASTON, and R. MARTINEAU, “The Method of Manufactured Solutions for Rattlesnake, a S_N Radiation Transport Solver inside the MOOSE Framework,” Tech. rep., Idaho National Laboratory (2012).
- [48] Y. WANG, “Rattlesnake - the Radiation S_N Transport Application with MOOSE for Multiphysics Simulations,” .
- [49] H. KIM, M. H. KIM, and M. KAVIANY, “Lattice thermal conductivity of UO_2 using *ab-initio* and classical molecular dynamics,” *Journal of Applied Physics*, **115** (2014).
- [50] Z. WANG and X. HUANG, “A non-equilibrium molecular dynamics study of the thermal conductivity of uranium dioxide,” *Nuclear Science and Techniques* (2010).

- [51] H. JAHN and E. TELLER, “Stability of Polyatomic Molecules in Degenerate Electronic States,” *Proceedings of the Royal Society of London*, **161**, 220–235 (1937).
- [52] J. ZIMAN, *Electrons and Phonons: The Theory of Transport Phenomena in Solids*, Oxford University Press (2001).
- [53] G. SRIVASTAVA, *The Physics of Phonons*, Taylor & Francis (1990).
- [54] *MATLAB and Statistics Toolbox Release 2014b*, The MathWorks, Inc., Natick, Massachusetts, United States.
- [55] B. S. KIRK, J. W. PETERSON, R. H. STOGNER, and G. F. CAREY, “libMesh: A C++ Library for Parallel Adaptive Mesh Refinement/Coarsening Simulations.” *Engineering with Computers*, **22**, 3-4, 237–254 (2006).
- [56] S. BALAY, S. ABHYANKAR, M. F. ADAMS, J. BROWN, P. BRUNE, K. BUSCHELMAN, V. EIJKHOUT, W. D. GROPP, D. KAUSHIK, M. G. KNEPLEY, L. C. MCINNES, K. RUPP, B. F. SMITH, and H. ZHANG, “PETSc Users Manual,” Tech. Rep. ANL-95/11 - Revision 3.5, Argonne National Laboratory (2014).
- [57] S. N. LABORATORY, *CUBIT Geometry and Mesh Generation Toolkit*, 14.1 ed.
- [58] F. INCROPERA, D. DEWITT, ET AL., *Introduction to Heat Transfer*, John Wiley & Sons, Inc., 5th ed. (2007).
- [59] A. PETIT and P. DULONG, “Recherches sur quelques points importants de

- la Theorie de la Chaleur," *Annals de Chimie et de Physique*, **10**, 395–413 (1819).
- [60] J. KESTIN ET AL., "Equilibrium and Transport Properties of the Noble Gases and Their Mixtures at Low Density," *Journal of Physical Chemistry Reference Data*, **13**, 1 (1984).
- [61] *CRC Handbook of Chemistry and Physics*, CRC Press, 85 ed. (2005).
- [62] T. XIAO-FENG, L. CHONG-SHENG, Z. ZHENG-HE, and G. TAO, "Molecular Dynamics simulation of collective behaviour of Xe in UO₂," *Chinese Physics B* (2010).
- [63] O. SIFNER and J. KLOMFAR, "Thermodynamic Properties of Xenon from the Triple Point to 800 K with Pressures up to 350 MPa," Tech. rep., Institute of Thermomechanics (1992).
- [64] S. SASAKI, N. WADA, and H. T. KUME, "High-pressure Brillouin study of the elastic properties of rare-gas solid xenon at pressures up to 45 GPa," *Journal of Raman Spectroscopy* (2009).